Univerzita Karlova v Praze
Matematicko-fyzikální fakulta

# DIPLOMOVÁ PRÁCE



Marie Kratochvílová

**Studium magnetických a termodynamických vlastností ternárních sloučenin se silně korelovanými 4$f$ elektrony**

Katedra fyziky kondenzovaných látek
Vedoucí diplomové práce: RNDr. Jiří Pospíšil
Studijní program: Fyzika, FKSM
Fyzika kondenzovaných soustav a materiálů

Praha 2011

Charles University in Prague
Faculty of Mathematics and Physics

# DIPLOMA THESIS

Marie Kratochvílová

## Study of magnetic and thermodynamic properties of ternary compounds with strongly correlated 4*f* electrons

Department of Condensed Matter Physics
Supervisor: RNDr. Jiří Pospíšil
Study program: Physics,
Physics of Condensed Matter and Materials

Praha 2011

Prohlašuji, že jsem tuto diplomovou práci vypracovala samostatně a výhradně s použitím citovaných pramenů, literatury a dalších odborných zdrojů.

Beru na vědomí, že se na moji práci vztahují práva a povinnosti vyplývající ze zákona č. 121/2000 Sb., autorského zákona v platném znění, zejména skutečnost, že Univerzita Karlova v Praze má právo na uzavření licenční smlouvy o užití této práce jako školního díla podle § 60 odst. 1 autorského zákona.

V Praze dne 15. 4. 2011

Marie Kratochvílová

# Contents

*Název práce:* Studium magnetických a termodynamických vlastností ternárních sloučenin se silně korelovanými 4$f$ elektrony

*Autor:* Marie Kratochvílová

*Katedra (ústav):* Katedra fyziky kondenzovaných látek

*Vedoucí diplomové práce:* RNDr. Jiří Pospíšil

*Abstrakt:* Zabývali jsme se studiem sloučeniny YPd$_2$Al$_3$ a systému sloučenin Ce$_n$T$_m$In$_{3n+2m}$. Polykrystal YPd$_2$Al$_3$, nový člen skupiny *RE*Pd$_2$Al$_3$, byl připraven pomocí obloukového tavení. Rentgenová difrakce potvrdila, že fáze YPd$_2$Al$_3$ krystalizuje v hexagonální soustavě typu PrNi$_2$Al$_3$. Měření magnetizace, AC susceptibility, měrného tepla a elektrického odporu odhalilo supravodivost pod teplotou $T_s \approx 2{,}2$ K. V druhé části práce jsme se zabývali studiem sloučeniny Ce$_2$PdIn$_8$ a systému sloučenin Ce$_n$RhIn$_{3n+2}$ dopovaných palladiem. Monokrystaly sloučenin Ce$_2$Rh$_{1-x}$Pd$_x$In$_8$ s $x = 0$; 0,10; 0,15; 0,30; 0,45; 0,85; 1 a CeRh$_{1-x}$Pd$_x$In$_5$ s $x = 0$; 0,1; 0,25 byly připraveny metodou růstu z roztoku. Energiově disperzní analýza a rentgenová difrakce potvrdily kvalitu a složení monokrystalů. Pomocí měření magnetizace, měrného tepla a elektrického odporu jsme zkoumali vliv dopování palladiem na magnetické vlastnosti Ce$_n$Rh$_{1-x}$Pd$_x$In$_{3n+2}$. Bylo zjištěno, že dopování palladiem postupně potlačuje Néelovu teplotu v obou systémech, ale jeho vliv je silnější v případě sloučenin Ce$_2$Rh$_{1-x}$Pd$_x$In$_8$. Teplotní závislost odporu sloučeniny CeRh$_{0.75}$Pd$_{0.25}$In$_5$ byla studována v tlacích dosahujících až 2,2 GPa. Podobně jako v případě fáze CeRhIn$_5$ je s rostoucím tlakem postupně potlačováno antiferomagnetické uspořádání a indukuje se supravodivost, která koexistuje s antiferomagnetismem.

*Klíčová slova:* YPd$_2$Al$_3$, Ce$_n$T$_m$In$_{3n+2m}$, supravodivost, antiferomagnetismus, těžkofermionové chování

*Title:* Study of magnetic and thermodynamic properties of ternary compounds with strongly correlated 4$f$ electrons

*Author:* Marie Kratochvílová

*Department:* Department of Condensed Matter Physics

*Supervisor:* RNDr. Jiří Pospíšil

*Abstract:* We have studied two different systems of compounds, YPd$_2$Al$_3$ and Ce$_n$T$_m$In$_{3n+2m}$. Polycrystalline YPd$_2$Al$_3$, a new member of the *RE*Pd$_2$Al$_3$ system, was prepared by arc melting. The X-ray diffraction confirmed that YPd$_2$Al$_3$ crystallizes in the hexagonal PrNi$_2$Al$_3$-type structure as the other *RE*Pd$_2$Al$_3$ compounds. Magnetization, AC susceptibility, specific heat and resistivity measurements revealed superconductivity below $T_s \approx 2.2$ K. The second part of the work was focused on studies of Ce$_2$PdIn$_8$ and Pd-doped Ce$_n$RhIn$_{3n+2}$. Single crystals of Ce$_2$Rh$_{1-x}$Pd$_x$In$_8$ with $x = 0$, 0.10, 0.15, 0.30, 0.45, 0.85, 1 and CeRh$_{1-x}$Pd$_x$In$_5$ with $x = 0$, 0.1, 0.25 were prepared by solution growth method. The quality of crystals was confirmed by microprobe analysis and X-ray diffraction. The effect of Pd doping on magnetism of Ce$_n$Rh$_{1-x}$Pd$_x$In$_{3n+2}$ was studied by specific heat, magnetization and resistivity measurements. The Pd doping gradually suppresses the Néel temperature in both systems, however the effect is stronger in Ce$_2$Rh$_{1-x}$Pd$_x$In$_8$. Temperature dependence of resistivity of CeRh$_{0.75}$Pd$_{0.25}$In$_5$ was studied in pressure up to 2.2 GPa. Similar to CeRhIn$_5$, the antiferromagnetism is gradually suppressed by the applied pressure, while superconductivity is induced and coexists with ntiferromagnetism.

*Keywords:* YPd$_2$Al$_3$, Ce$_n$T$_m$In$_{3n+2m}$, superconductivity, antiferromagnetism, heavy fermion behavior

# 1.    Introduction

In this work "Study of magnetic and thermodynamic properties of ternary compounds with strongly correlated 4*f* electrons" we have focused on the study of selected materials containing rare earth (*RE*) elements, which takes in lanthanides, yttrium and scandium. Magnetism of 4*f* (lanthanide) elements [1] is particularly interesting considering the localized character of 4*f* electrons, contrasting to the itinerant character of electrons in the iron (3*d*), palladium (4*d*) and platinum (5*d*) group [1]. The localization of the 4*f* electrons deep in the electron-shell structure leads to a weak, however intriguing interactions [2,3]. Therefore the *RE* intermetallics exhibit a variety of interesting physical properties such as complex magnetic structures, strong magnetocrystalline anisotropy or exotic superconductivity (SC) [4].

The term strongly correlated electrons [4] (SCE) is usually reserved to systems with strong interaction or hybridization between narrow open *d-* (transition metals) or *f -* (rare earth and actinides) shells and conduction electrons. Strongly correlated electron systems (SCES) have been attracting attention of physicists for more than 50 years representing a great variety of unusual physical phenomena such as Kondo screening, heavy fermion (HF) behavior, coexistence of magnetism and superconductivity [4,5]. Since the discovery of heavy fermion superconductivity in $CeCu_2Si_2$ [6] groups of various compounds have been investigated. For example, series $CeT_2X_2$ (*T* – transition metal; *X* = Si or Ge) representing the interplay between antiferromagnetism (AF) and SC have been studied for several decades [7]; on the other hand, the superconducting ferromagnetic compound $UCoGe$ [8] from the *UTX* series or the $Ce_nT_mIn_{3n+2m}$ (*n* = 1, 2; *m* = 1; *T* = Co, Ir, Rh and Pd) [7,9-11] system exhibiting heavy fermion SC with very high transition temperatures has been investigated in recent years (especially the relatively new members $Ce_2PdIn_8$ [12,13] and $CePt_2In_7$ [14]).

## 1.1.    Motivation & Aim

The work is based on two main topics:

The first part is devoted to the study of $YPd_2Al_3$ – a new member of the well-known group of $REPd_2Al_3$ intermetallic compounds [15,16]. The study of $YPd_2Al_3$ resumes author's bachelor project [17] focused on $SmPd_2Al_3$ [18]. $YPd_2Al_3$ was studied with intent to investigate properties of a non-*f*-electron analog to $REPd_2Al_3$ (*RE* = La, Ce, Pr, Nd, Sm, Gd) family of compounds. Since the $REPd_2Al_3$ family exhibits a broad range of types of magnetic ordering, which are strongly influenced by crystal field (CF) interactions [15,19]. Our preliminary studies of $YPd_2Al_3$ revealed superconductivity below 2.2 K which enhanced the interest in the investigation of this material.

The second class of materials investigated in this work involved selected members and substitutions of the $Ce_nT_mIn_{3n+2m}$ group, (often called 115 and 218 compounds with *m* = 1, *n* = 1 and 2, respectively) namely Pd-doped $Ce_nRhIn_{3n+2}$, and $Ce_2PdIn_8$. The series $Ce_nT_mIn_{3n+2m}$ (*T* = Co, Rh, Ir) exhibits heavy fermion superconductivity which often coexists with antiferromagnetic order as in the case of $Ce_nRhIn_{3n+2}$. $Ce_2PdIn_8$, as a new member of the $Ce_nT_mIn_{3n+2m}$ has been recently discovered as a new heavy fermion superconductor [9,10] with $T_s < 0.7$ K, however, the critical temperature was found to be strongly influenced by sample preparation [20,21]. Therefore we have tried to focus on this problem to find the optimal growth

conditions for the highest and sharpest reported SC transition temperature. Although the existence of $CePdIn_5$ has not been reported yet, one of our aims was to grow Pd-doped $CeRhIn_5$ and $Ce_2RhIn_8$ up to the maximum concentration range of Pd content and to study the influence of the doping on magnetic properties and superconductivity.

## 1.2.  Outline of the thesis

The work has six chapters including introduction. Chapter 2 is devoted to the introduction to the theory of rare earth intermetallics discussing the phenomena connected with the compounds studied in this work. Next chapter introduces previous results and a brief overview of properties of materials selected for our studies. Chapter 4 provides the description of used methods for sample synthesis with the main emphasis placed on the solution growth method and sample characterization techniques, as well as the measurement techniques. A special subsection of Chapter 4, Experimental techniques, is devoted to the discussion of influence of the sample's shape on demagnetization field. Chapter 5 presents the results obtained in this work, while the last chapter is the summary followed by possible future plans. Appendix A introduces first results of differential thermal analysis (DTA) of Ce-Pd-In system which present an important contribution to sample synthesis.

# 2. Introduction to the physics of *RE* intermetallic compounds

## 2.1. Magnetism of 4*f* electrons

The ground state of ions with partially filled *d*- or *f*- shells is given by Hund's rules, and it is described by the total spin and orbital momentum $S$ and $L$, as well as by the total angular momentum $J$ [2,22]. The Hund's rules explain how to fill the one-electron levels. The ground state should have the largest total spin $S$ consistent with the Pauli exclusion principle along the first rule. The second rule says that the total orbital momentum $L$ has the largest value that is consistent with the first Hund's rule. Finally, the third Hund's rule originating from the spin-orbital coupling determines the value of total angular momentum $J$; $J$ is equal for $L+S$ for more than half filled shells and $|L-S|$ for less than half filled shells. However, the theoretical values of magnetic moments for free *f*-ions predicted by Hund's rules are usually somewhat lower than the experimental values of magnetic moments in *RE* compounds, which is caused mainly by CF effects. The spin-orbital coupling as well as the CF interaction can be described within the general full free-ion Hamiltonian $\hat{H}$. The Hamiltonian $\hat{H}_0$, the residual interaction $\hat{G}$, crystal field Hamiltonian $\hat{H}_{CF}$ together with spin-orbital coupling $\hat{H}_{SO}$, form the full free-ion Hamiltonian $\hat{H}$ [22,23] from the independent electron approximation:

$$\hat{H} = \hat{H}_0 + \hat{G} + \hat{H}_{SO} + \hat{H}_{CF} \tag{1}$$

Hamiltonian $\hat{H}_0$ is represented by the kinetic energy of $N$ electrons at positions $r_i$ together with electrostatic potential of bare nuclei and effective potential $V_{ef}$:

$$\hat{H}_0 = \sum_i^N \left( -\frac{h^2 \Delta_i}{2m_e} - \frac{Ze'^2}{r_i} + V_{ef}(r_i) \right) \tag{2}$$

Here $Z$ is the atomic number and $\Delta_i$ is the Laplacian operator. Effective potential $V_{ef}$ represents electron-electron interaction equal to Coulomb and exchange interaction from the Hartree-Fock approximation. Residual interaction $\hat{G}$ given by

$$\hat{G} = \frac{1}{2} \sum_{i,j} \frac{e'^2}{r_{ij}} - \sum_i V_{ef}(r_i) \tag{3}$$

can be treated as a perturbation [23].

Spin-orbital interaction $\hat{H}_{SO}$, the most significant among the relativistic corrections of the Dirac equation, is a result of the relativistic perturbation. It is given by

$$H = \lambda(\boldsymbol{L}.\boldsymbol{S}) \tag{4}$$

where $\lambda$ is a constant for given LS state. Spin-orbital interaction influences the states with well defined quantum numbers $L$ and $S$ and because of this, $L$ and $S$ are not separately conserved but the total angular momentum $J = L + S$ is conserved. The multiplets split up into different fine structure levels labeled by $J$ due to $\hat{H}_{SO}$. The third Hund's rule arises from an attempt to minimize the spin-orbit energy, as mentioned earlier.

The spin-orbit interaction is the primary source of the magnetocrystalline anisotropy. Magnetocrystalline anisotropy is developed by locking magnetic moments in certain crystallographic directions. As a result, certain crystallographic directions are preferred for the magnetization; i. e. magnetically anisotropic material will order its moments into the direction of its easy axis [2,3,24].

Crystal field splitting is a perturbation, which plays a significant role among rare earths, is the interaction between $4f$ electrons and crystal field. Crystal field represents the local environment due to the crystal symmetry. The perturbation can be described by the crystal field Hamiltonian

$$\hat{H}_{CF} = \sum_{L,M} B_L^M \hat{O}_L^M \tag{5}$$

where $B_L^M$ represents CF parameters depending on the symmetry of crystal field and $\hat{O}_L^M$ CF operators summed over quantum numbers $\boldsymbol{L}$ and $\boldsymbol{M}$. Crystal field influences the energy levels of an atom, so it is necessary to first review the shapes of the atomic orbitals. The asphericity in charge density of electrons from the outer $6s5d$ shell in $RE$ atoms influences significantly the CF splitting of the $(2J+1)$-fold degenerate energy levels. Depending on the site symmetry, the CF remove partly or entirely the $(2J+1)$-fold degeneracy of the free-ion $J$ multiplets [22,25].

Hamiltonians $\hat{H}_{CF}$ and $\hat{H}_{SO}$ represent the basic sources of magnetic anisotropy. For $4f$ electrons the $\langle \hat{H}_{CF} \rangle$ is usually much weaker than $\langle \hat{H}_{SO} \rangle$ [25]. In the case of $3d$ metals the crystal field is much stronger than the spin-orbit coupling and this leads also to invalidation of the Hund's third rule due to quench of $\boldsymbol{L}^2$. The situation for higher transition series ($4d$ and $5d$) is more complex, since in the heavier elements the spin-orbit coupling is stronger, often comparable to CF splitting [22,25].

**Exchange interactions**

Exchange interactions stand behind the phenomenon of long range magnetic order. The Heisenberg Hamiltonian [3], which describes the energy of these interactions, is given by

$$H_{ij} = -2J_{ij} \boldsymbol{S}_i \boldsymbol{S}_j \tag{6}$$

where $J_{ij}$ is the exchange integral and $\boldsymbol{S}_i$, $\boldsymbol{S}_j$ are the appropriate spin quantum numbers.

There are 3 basic types of exchange interactions:

The *direct interaction* is short range because it proceeds directly without the need for an intermediary. Direct exchange appears by metals with overlapping $d$ orbitals.

*Super exchange* is a coupling between two next-to-nearest neighbor cations through a non-magnetic anion. It is usually observed in intermetallic compounds with $f$ and $d$ or $p$ metals.

Magnetic moments of 4$f$ electrons interact via *the indirect RKKY (Ruderman, Kittel, Kasuya, Yoshida) interaction*. RKKY interaction is realized whereby conduction electrons which interact with the spins via hyperfine interaction and create a correlation energy between them. The interaction is weak, long range and has an oscillatory dependence on the distance $r$ (see Fig. 1) between the magnetic moments:

$$J_{RKKY}(r) \propto \frac{\cos(2k_F r)}{r^3} \tag{7}$$

Here $k_F$ is the radius of spherical Fermi surface.
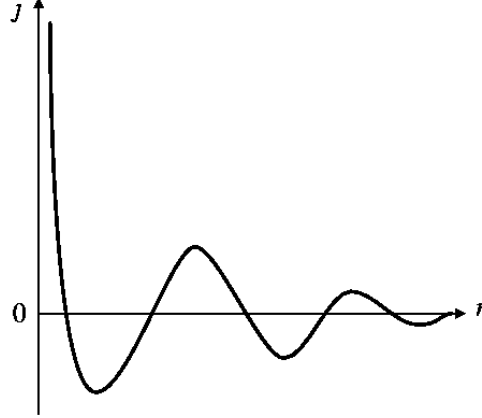


Fig. 1: Variation of the exchange integral $J$ [26].

## 2.1.1. Basic types of magnetic behavior

The quantum mechanical aspect ascribes the origin of free atom magnetic moment to the orbital moment, spin moment (paramagnetic contribution) and the interaction of the orbital moment with an external magnetic field (diamagnetic contribution). A convenient unit for describing the size of atomic magnetic moments is called Bohr magneton $\mu_B$:

$$\mu_B = \frac{e\hbar}{2m_e} \tag{8}$$

Magnetic moment per volume defines the magnetization $M$. Magnetization together with the intensity of magnetic field $H$, defines the magnetic susceptibility $\chi$. It is a magnetic moment induced by the intensity of magnetic field per volume unit. Susceptibility $\chi$ is generally a tensor quantity, defined as differential susceptibility $\chi_{ij}$, but in the case when $M$ is very accurately linear in $H$, the definition reduces into [22]

$$\chi_{ij} = \frac{\partial M_i}{\partial H_j} \rightarrow \chi = \frac{M}{H}. \tag{9}$$

**Diamagnetism**

Diamagnetic materials are characterized by the negative value of the magnetic susceptibility, which is temperature and field independent. The external field induces a weak magnetic moment, which acts against the direction of the external field. This can be interpreted as a consequence of the Lenz law. The quantum mechanical approach describes diamagnetism using diamagnetic term in Hamiltonian for an atom in external field $B$ oriented

along the *z*-axis. From this term, the classical Langevin relation for diamagnetic susceptibility can be derived as

$$\frac{e^2 B^2}{8 m_e} \sum_i (x_i^2 + y_i^2) \rightarrow \chi_{dia} = \sum_i^z \langle r_i^2 \rangle \frac{N e^2 \mu_0}{6 V m_e} \tag{10}$$

where $N$ is the number of ions and $V$ marks the volume. Expression $\langle r^2 \rangle$ is related to the magnetic loop [2].

Diamagnetism is present in all materials but its contribution is usually weak compared to other effects (paramagnetism etc.). The diamagnetic response is observable in the case of solid noble gases, metals like copper, silver and gold and by simple ionic crystals.

Superconductors form a special class of diamagnetic materials, considered to be ideal diamagnets with $\chi = -1$ due to Meissner effect (this kind of diamagnetism arises from persistent screening currents which flow to oppose the applied field; this external field is then expelled from the whole volume of the superconductor) [22].

**Paramagnetism**

The shells of atoms in paramagnetic materials are partially filled and therefore give rise to spin and orbital moments. These moments are oriented randomly and their magnetization is zero until an external field is applied. As a result, the moments orientate into the direction of the field.

In classical physics the magnetic moment $m$ is presented by a loop of area $A$ where a current $I$ is circulating:

$$m = IA \tag{11}$$

In quantum mechanical approach, the magnetic moment of an ion is associated with its total angular momentum $\boldsymbol{J}$ which is a sum of the orbital angular momentum $\boldsymbol{L}$ and the spin angular momentum $\boldsymbol{S}$, so that

$$J = L + S . \tag{12}$$

Magnetic moment $\boldsymbol{m}$ of a free ion can be defined using $\boldsymbol{J}$ as

$$\boldsymbol{m} = -g_J \mu_B \boldsymbol{J} \tag{13}$$

where $g_J$ is the Landé factor.

The effective magnetic moment $\mu_{eff}$ is given by

$$\mu_{eff} = g_J \mu_B \sqrt{J(J + 1)} . \tag{14}$$

It is necessary to distinguish cases where $J = 0$ and $J \neq 0$. If the shell has $J = 0$, the ground state is nondegenerate and the first-order perturbation (linear term) predicts no paramagnetic contribution for $J = 0$ (closed shells or shells that are one electron short of being half filled):

$$\mu_B \boldsymbol{H} \langle n | \hat{\boldsymbol{L}} + g_J \hat{\boldsymbol{S}} | n \rangle \tag{15}$$

However, the second-order calculation gives a change in the ground state energy $E_0$ and the paramagnetic susceptibility is then given by

$$\chi_{par} = \frac{2N\mu_B^2}{V}\left(\sum_n \frac{|\langle 0|(\hat{L} + g_J\hat{S})|n\rangle|^2}{E_n - E_0}\right) \tag{16}$$

where $E_0$, $E_n$ are energies of the ground and excited states 0 and $n$. This paramagnetic contribution to diamagnetic susceptibility is called Van Vleck paramagnetism and is, similar to diamagnetism, small and temperature independent [2,22]. If $J \neq 0$, the ground state is $(2J+1)$-degenerate in zero field and the linear term is large enough to neglect the diamagnetic and second-ordered perturbation term.

Using the Boltzmann distribution and Brillouin function [3]

$$B_J(y) = \frac{2J+1}{2J}\coth\left(\frac{2J+1}{2J}y\right) - \frac{1}{2J}\coth\frac{y}{2J} \tag{17}$$

where $y$ is the substitution with the applied field $\boldsymbol{B}$ and temperature $T$

$$y = \frac{m\boldsymbol{B}}{k_B T}, \tag{18}$$

we obtain the definition of the paramagnetic susceptibility

$$\chi_{par} = \frac{n\mu_0\mu_{eff}^2}{3k_B T} = \frac{C}{T} \tag{19}$$

for $n$ spins per unit volume. The paramagnetic susceptibility is positive and field independent but it decreases with rising temperature due to the increase of thermal disorder of the magnetic moments. The last term is known as Curie law with Curie constant $C$.

Until now, the contributions concerning the rare earth magnetism were discussed, but the contribution of itinerant conduction electrons to the magnetic moment was not mentioned yet. The wave functions of the valence electrons form a band with equal numbers of spins up and down. When an external field is applied, only electrons close to Fermi energy $E_F$ change the orientation of their spins because other electron states with spins parallel to external field are already occupied. As a result, a small surplus of one type of spins will emerge. This effect, known as Pauli-paramagnetism, is temperature-independent and even weaker than Van Vleck paramagnetism. Pauli paramagnetic susceptibility is given by

$$\chi_P = \mu_B^2 DOS(E_F) \tag{20}$$

where DOS is the density of states for the conduction band at Fermi energy [2,22].

**Magnetically ordered states**

In a material with strongly interacting magnetic moments cooperative phenomena can be observed, leading to long-range ordering of magnetic moments at temperatures below a characteristic temperature. As a result, magnetic ordering is observed even with the absence of external magnetic field. Magnetic ordering develops generally due to exchange interactions which were described in Section 2.1. The magnetic ordering emerging in the *RE* compounds

is induced by the long-range RKKY interaction. The oscillatory character of the interaction determines the type of magnetic ordering - it may be either ferromagnetic (FM) where $J_{RKKY} > 0$, or antiferromagnetic where $J_{RKKY} < 0$, depending on the distance between the magnetic moments.

To describe the magnetically ordered state, approximation needs to be made. The exchange interaction can be replaced by using the effective molecular field (sometimes called Weiss molecular field) $\boldsymbol{B}_E = \lambda.\boldsymbol{M}$ where $\lambda$ is a constant which parameterizes the strength of the molecular field as a function of the magnetization [2,22,24]. The paramagnetic susceptibility in the external field $\boldsymbol{B}_{ext}$ is than given by

$$\mu_0 \boldsymbol{M} = \chi(\boldsymbol{B_{ext}} + \boldsymbol{B}_E). \tag{21}$$

Applying the Curie law on $\chi_P$, we get expression

$$\chi = \frac{C}{T - \theta_P} \tag{22}$$

known as Curie-Weiss (C-W) law where $\theta_P = \lambda C$ represents the Weiss temperature. This relation describes the paramagnetic behavior above the ordering temperature. Modified C-W law is defined as

$$\chi = \frac{C}{T - \theta_P} + \chi_0 \tag{23}$$

where $\chi_0$ is temperature independent contribution to the susceptibility.

Systems with elementary magnetic ordering as ferromagnets, antiferromagnets and ferrimagnets (FI) are shown in Fig. 2.
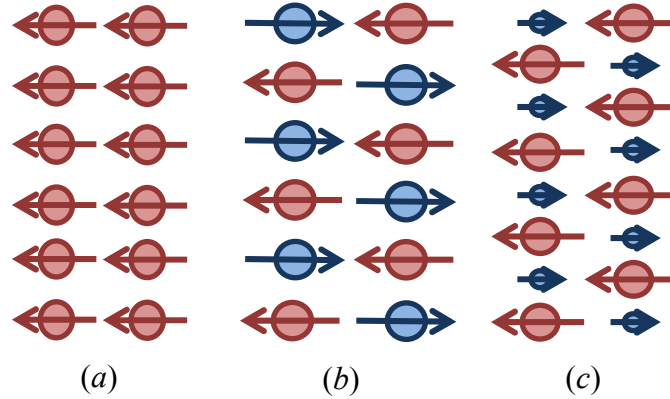


Fig. 2: Examples of various magnetically ordered systems – ferromagnetics (*a*), antiferromagnetics (*b*) and ferrimagnetics (*c*).

In the case of simple ferromagnets, the magnetic moments order parallel below characteristic Curie temperature $T_C \sim \theta_P > 0$ and thus we observe nonzero magnetization for $T < T_C$. Antiferromagnetic materials are characterized by an antiparallel ordering which is established below Néel temperature $T_N \sim \theta_P < 0$. In contrast to ferromagnetic ordering we observe zero magnetization below characteristic temperature due to mutual compensation of magnetic moments. The structure of AF material can be described using two penetrating

ferromagnetic sublattices A and B (red and blue atoms, respectively, in Fig. 2 (*b*)) with antiparallel magnetizations $M_A$ and $M_B$ ($|M_A| = |M_B|$). Ferrimagnetics can be treated as uncompensated antiferromagnetic materials using Néel sublattice model where we assume that $|M_A| \neq |M_B|$, as shown in Fig. 2 (*c*). The spontaneous magnetization $M = M_A - M_B$ is therefore nonzero and various types of $M_S$ (*T*) curves (spontaneous magnetization) are found for ferrimagnets depending on the temperature variation of sublattice magnetizations (see Fig. 3).



(*a*)                                                                (*b*)



(*c*)
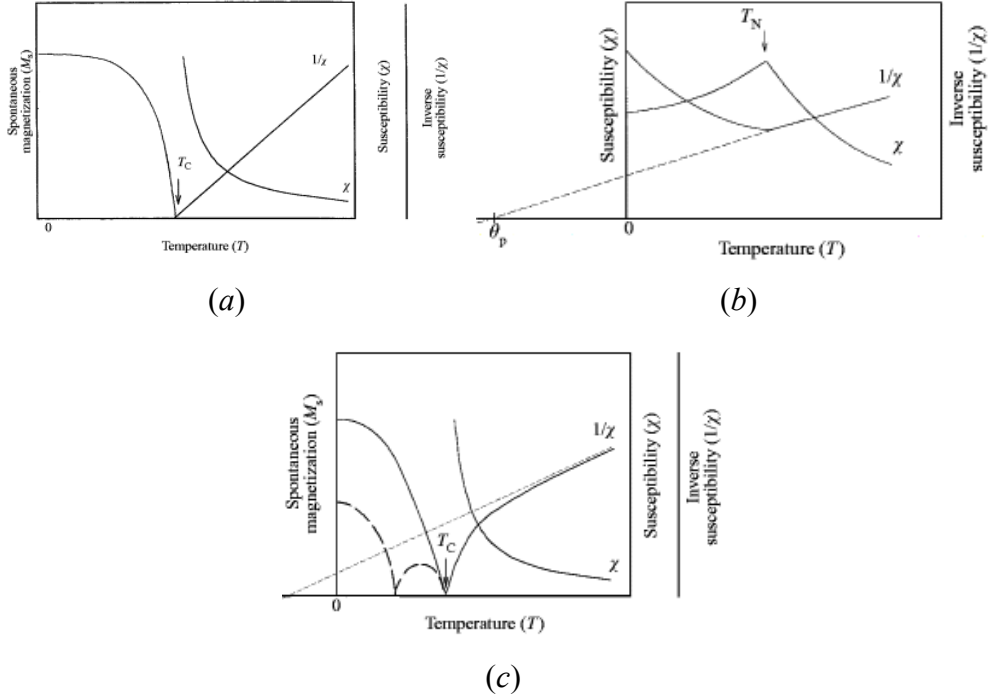
Fig. 3: Temperature dependencies of magnetization, susceptibility and inverse susceptibility for ferromagnetics (*a*), antiferromagnetics (*b*) and ferrimagnetics (*c*). After V. Sechovský [24].

Some examples of nontrivial magnetically ordered systems as weak ferrimagnets (WF), noncollinear antiferromagnets (NC-AF), spiral and helicoidal structures or spin glass (SG) are shown in Fig. 4. Spin glasses exhibit many metastable structures where usually ferromagnetic and antiferromagnetic bonds are randomly distributed (see Fig. 4 (*a*)). Spin-spiral state (see Fig. 4 (*b*)), also known as spin density wave (SDW) can be described as a function of the wave vector *q*. The left two spin configurations are examples of transversal spin-spiral states and the lower two spin configurations show a longitudinal spin-spiral state. Illustrations of the helicoidal spins (see Fig. 4 (*c*)) represented by arrows with proper screw, longitudinal conical and slanted conical spin structures [3,25].

(*a*)



(*c*)
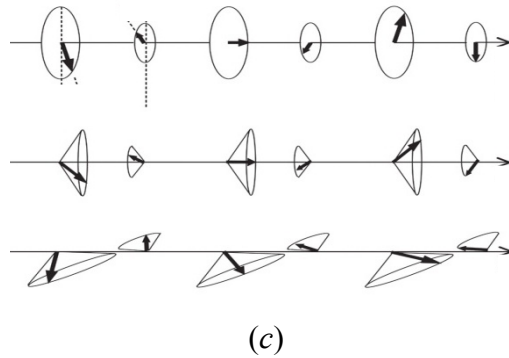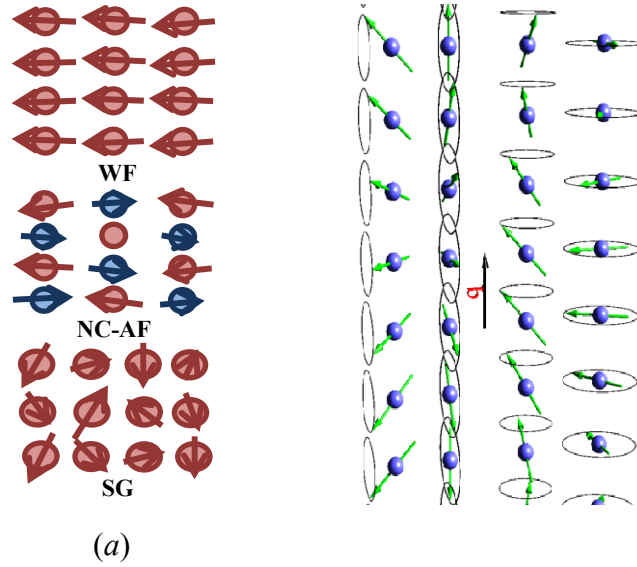
Fig. 4: Examples of nontrivial magnetically ordered systems - weak ferrimagnets (WF), noncollinear antiferromagnets (NC-AF) and spin glass (SG) (*a*), spiral (*b*) and helicoidal (*c*) structures. Figures (*b*) and (*c*) after Rancourt [27] and Ishiwata [28], respectively.

The wave vector $q$ characterizes the modulation of magnetic moments within the structure. If $q$ is equal to the reciprocal lattice vector $a$ (see Fig. 5) of the underlying crystal structure, or if it is a simple fraction thereof, the structure is called commensurate. The other magnetic structures with $q'$ are called incommensurate.
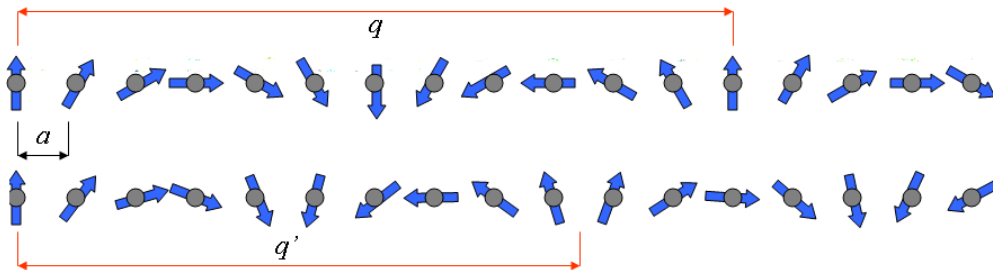


Fig. 5: Commensurate and incommensurate magnetic structure. After P. Javorský [29].

# 2.2. Strongly correlated electron systems

Generally, the term "electron correlations" means that each single electron has a complex influence on its neighbors. Simple metals, whose conduction electrons are essentially uncorrelated and which exhibit free-electron-like behavior, present the direct opposite of strongly correlated electron systems where the phenomena cannot be described effectively by studying the behavior of individual particles alone. Correlations are responsible for phenomena, such as superconductivity, arising from broad-band itinerant electrons, and for long-range magnetic ordering, emerging from the narrow-band localized electrons forming local magnetic moments. A term "strongly correlated electron systems" is mostly reserved for metallic systems where a strong interaction or hybridization of narrow open *d-* (transition metals) or *f-* (rare earth and actinides) shells and conduction electrons exists. The main topic concerns materials, which exhibit heavy fermion behavior [24].

## 2.2.1. Heavy fermion compounds

### Fermi gas and Fermi liquid

Fermi gas [30] is an electron gas consisting of non-interacting, independent electrons. There are no interactions with the lattice of magnetic ions and no electron-electron interactions other than the Pauli exclusion principle. The specific heat of Fermi gas $C_{el}$ is linearly dependent on temperature with coefficient $\gamma$, called Sommerfeld coefficient. The Sommerfeld coefficient $\gamma$ (typical values in mJ mol$^{-1}$ K$^{-2}$ range) is proportional to the density of states and therefore to the electron mass $m_e$.

Fermi liquid can be treated as Fermi gas with interactions. The electron-electron and electron-lattice interactions lead to a substantially modified energy dispersive relations forming narrow bands which enhances density of states at the Fermi level. As a consequence of the enhanced density of states, the characteristic effective masses $m_{eff}$ of the conduction electrons increase. A quasiparticle approximation is therefore needed.

In the so-called heavy fermion systems, the effective mass of these new quasiparticles - ("heavy fermions") is enhanced more than hundred times [31] due to a weak overlap of wave functions of *f* electrons on neighboring ions [32]. The linear term $\gamma \sim 1/T_K$ in the electronic specific heat and magnetic susceptibility $\chi$ are much larger than those corresponding to normal magnetic behavior. Hence:

$$\chi = \chi_P \frac{m^*}{m_0}(1 + F_0^{\alpha}) \tag{24}$$

where $\chi_P$ is the Pauli susceptibility, $m_0$ is the free-electron mass and $F_0^{\alpha}$ is the additional Landau parameter [30].

The values of $\gamma$ are typically of the order of 1000 mJ mol$^{-1}$ K$^{-2}$ for non-magnetic compounds at low temperatures and 100 mJ mol$^{-1}$ K$^{-2}$ for compounds ordered magnetically [4]. Since the electronic contribution to the specific heat $C_{el}$ is given by $C_{el} = m_{eff}/m_0 \gamma T$, a large electronic contribution to the specific heat (at low) temperatures is observed.

The Fermi liquid model explains the temperature dependence of resistivity by electron-electron interactions. The temperature dependence of resistivity has a quadratic character given by

$$\rho = \rho_0 + AT^2 + \cdots \tag{25}$$

where the coefficient $A$ reflects the strongly enhanced state similar to coefficients $\chi$ and $\gamma$ [31]. It is difficult to observe the quadratic behavior for normal metals where the coefficient $A$ is too low compared to the residual resistivity $\rho_0$.

**Intermediate valence**

The valence, i.e. number of conduction electrons, is usually constant in the case of *RE* elements where the trivalent oxidation state strongly dominates [33]. Some elements with almost empty 4*f* shell like Ce, elements with a nearly half-filled shell like Sm and Eu, or with an almost filled 4*f* shell like Tm and Yb break this rule by exhibiting intermediate valence [4]. The necessary condition for non-integer valence to occur is a strong hybridization of conducting electrons state and localized 4*f* state. Intermediate valence is represented by a homogeneous quantum mechanical mixture of two consecutive integer valence configurations. It can be induced by pressure, temperature or by a specific material composition. For example, valence of Ce ions can change from common trivalent to tetravalent when the lattice is cooled or compressed [34]. The energy of the inner 4*f* level is nearly the same as that of the valence electrons, so only small energy is required to change the relative occupancy of these electronic levels. Reversal effect is observable in Yb compounds on the opposite side of the *RE* series [4].

## 2.2.2. Kondo effect

**Anderson model and Kondo behavior**

The first studied strongly correlated electron systems were 3*d*-metal impurities (iron, cobalt, nickel…) [4] placed in a host matrix such as copper or Nb-Mo alloys [35]. These systems were described theoretically by Anderson in 1961 [36]. He introduced a hybridization Hamiltonian where the 3*d* (or 4*f* or 5*f*) level located at the energy $E_d$ is hybridized with the conduction electrons by the hybridization parameter $V_{dk}$ [4]:

$$\text{H} = \sum_{k\sigma} \varepsilon_k n_{k\sigma} + E_d(n_{d\uparrow} + n_{d\downarrow}) + U n_{d\uparrow} n_{d\downarrow} + \sum_{k\sigma} V_{dk}(c_{d\sigma}^+ c_{k\sigma} + c_{d\sigma} c_{k\sigma}^+) \tag{26}$$

The first term represents the energy of conduction electrons where $\varepsilon_k$ is the energy dispersion relation of the conduction-electron band and $n_{k\sigma}$ the number operator for wave vector $k$ and conduction electron spin $\sigma$. The 3*d* (or 4*f* or 5*f*) level located at the unperturbed energy $E_d$ with the corresponding number operators $n_{d\uparrow}$ and $n_{d\downarrow}$ form together the second term. The third term describes the Coulomb repulsion between *d*- (or *f*- localized) states. The Coulomb integral $U$ for the localized electrons is considered to be very large due to strong correlations. The second term is hybridized with the conduction electrons by the hybridization parameter $V_{dk}$ from the last term. Hybridization parameter $V_{dk}$ is responsible for tunneling from the state $d$ to state $k$ while $c_{d\sigma}$ ($c_{d\sigma}^+$) and $c_{k\sigma}$ ($c_{k\sigma}^+$) are annihilation (creation) operators for *d*- or *f*-electrons and conduction band, respectively. Term $V_{dk}$ broadens localized states into one of Friedel's resonances [37].

Friedel's resonance Δ has a characteristic width

$$\Delta = \pi \langle V_{dk}^2 \rangle \rho(E_d) \ . \tag{27}$$

Anderson model in the $U \gg \Delta$ limit [38] leads to model, which was presented by Kondo [39] in 1964 (both models are equivalent in this limit). The calculations made by Kondo explained the behavior of magnetic impurities (transition metals and rare earths) in diluted alloys, especially the resistivity minimum in diluted magnetic alloys, which was firstly observed in 1931 [4,40]. The system within the Kondo model is well described by the classical exchange Hamiltonian $H_{ex} = -2JS.\sigma$ where $S$ represents localized impurity spin and $\sigma$ represents conduction electron spin. The quantity $J$ is an effective exchange parameter, which originates from the hybridization. Positive value of $J$ points to ferromagnetic coupling, while a negative one to antiferromagnetic coupling.

Kondo computed the magnetic resistivity $\rho_m$ in second-order perturbation [39] and found out that the magnetic resistivity decreases with increasing temperature for $J < 0$. Considering that the total resistivity is the sum of magnetic resistivity $\rho_m$, phonon resistivity $\rho_{ph}$, which increases linearly with increasing temperature, and temperature-independent residual resistivity, a minimum appears on the curve representing the temperature dependence of resistivity. The resistivity increases logarithmically from the minimum with decreasing temperature. Kondo's calculation is valid only at sufficiently high temperatures above so-called Kondo temperature $T_K$

$$T_K k_B = D e^{\frac{-1}{|J \cdot \rho(E_F)|}} \tag{28}$$

where $\rho(E_F)$ is the density of states for the conduction band at Fermi energy. Kondo problem for $T = 0$ K was solved by Wilson in 1975 [41]. At $T = 0$ K, the ground state of the impurity with spin $S$ is found to be completely screened (compensated) by the surrounding conduction electron spins $\sigma$ with antiferromagnetic orientation, thus forming a non-magnetic singlet. The electron screening cloud has a certain correlation length, which increases with decreasing temperature. Increasing concentration of impurities leads to their mutual interactions via conduction electrons (RKKY interaction). This effect destroys the singlet state and the Kondo behavior disappears [4,42].

**Kondo lattice**

In some cases the local moments (e.g. Ce, Yb or U atoms) are ordered in regular crystal lattice while they are still Kondo coupled to conduction electrons. Such materials are called Kondo lattice materials. The behavior of Kondo lattice differs strongly from the single Kondo impurity because the intersite interactions between the localized magnetic moments of the impurities cannot be neglected any longer. The coherent superposition of scattering amplitudes of all Kondo impurities in the lattice appears. The resistivity curve of a Kondo lattice does not raise till the lowest temperatures as in the case of single impurity but it reveals a maximum as shown in Fig. 6. Temperature $T_K$ is roughly proportional to temperature at the maximum on the resistivity curve [42,43].
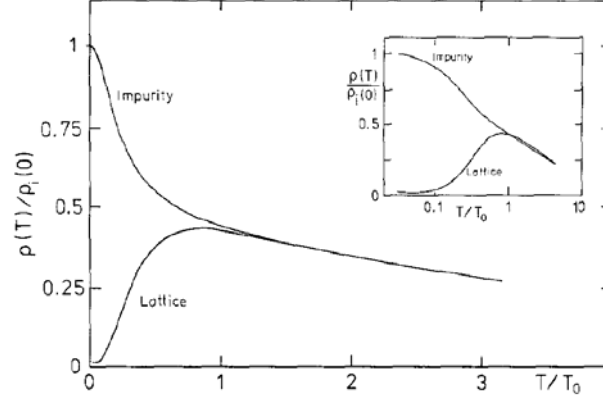
Fig. 6: Temperature dependent normalized resistivity for single Kondo impurity and Kondo lattice calculated by Cox and Grewe [44].

**Doniach diagram**

The competition between the Kondo effect, which tends to suppress the magnetic moment with decreasing temperature on each atom and the RKKY interaction, which tends to give a magnetic ordering between different rare-earth atoms was described by Doniach in 1977 [45]. He presented an idea which describes the interactions in the heavy fermion compounds. His model is usually known in the form of the Doniach diagram shown in Fig. 7. The curve marked $T_{K0}$ represents Kondo temperature for the magnetic impurity:

$$T_{K0} \sim exp\left(-1/|J\rho|\right). \tag{29}$$

$T_{N0}$ is the Néel, resp. Curie temperature

$$T_{N0} \sim |J\rho|^2, \tag{30}$$

as if there were no Kondo effect ($|J\rho|$ represent the tuning parameter where $J$ is the exchange parameter and $\rho$ is the density of conduction electron states). In the limit of small $|J\rho|$, $T_{K0} < T_{N0}$, which leads to magnetic ordering of the system. On the other hand, for large $|J\rho|$, $T_{K0} > T_{N0}$ and the system does not order magnetically. As the result, the real Néel temperature $T_N$ increases with increasing $|J\rho|$, reaches a maximum and for critical value of $|J\rho|_c$ drops to zero at so-called quantum critical point (QCP) [46].
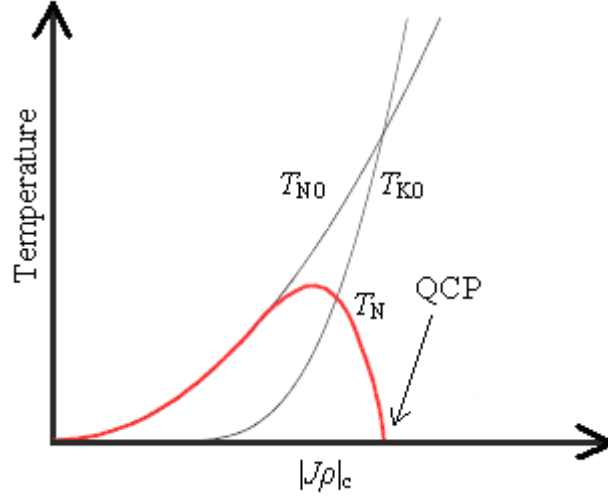
14

Fig. 7: Doniach diagram. The grey curves present the tuning parameter dependence of $T_{N0}$ and $T_{K0}$, the red curve presents the evolution of $T_N$.

The critical temperature $T_{K0}$ can be tuned to zero in the vicinity of QCP by applying the pressure, magnetic field or substitution (chemical pressure). Both hydrostatic pressure and substitution affect the interatomic distances but in contrast to chemical pressure (substitution), hydrostatic pressure saves composition, purity and shape of the sample [47].

The term "classical" phase transition has to be modified when $T_s$ vanishes at critical value of $|J\rho|_c$. At $T = 0$, only quantum fluctuations at phase transitions are possible. Thus, quantum phase transitions are not caused by thermal fluctuations, unlike the classical phase transitions. In the vicinity of QCP the description using Fermi liquid model fails. It is due to spin fluctuations. In the QCP, the transition to so-called non-Fermi liquid (NFL) behavior is observed [30]. In the NFL region, the electronic specific heat coefficient $\gamma$ is proportional to $\log(T)$ and magnetic resistivity is proportional to $T^{3/2}$ [48].

## 2.3. Superconductivity

Superconductivity was discovered in 1911 by Heike Kammerlingh Onnes in mercury, who was studying the resistance of solid mercury at cryogenic temperatures. He observed, that at the temperature of 4.2 K, the resistance of mercury abruptly disappeared [49,50]. Shortly after mercury, superconductivity was found in several other metals such as lead (1913) or tin (1935), however the theory which would explain this exciting phenomena came much later.

In the following years, many new phenomena connected with superconductivity have been observed, among them so-called Meissner effect, which was explained in 1933. Macroscopic properties of superconductors were well described by the phenomenological Landau-Ginzburg theory in 1950. The same year brought a discovery of critical temperature dependence of a superconductor on the isotopic mass of the constituent element. This observation called isotope effect pointed to microscopic mechanism responsible for superconductivity and thus to the existence of the electron-phonon interaction. Complete microscopic theory of superconductivity was formulated by Bardeen, Cooper and Schrieffer (BCS theory) in 1957 [51].

The superconducting current is according to BCS theory realized by Cooper pairs which are formed due to electron-phonon interactions [51]. Simplified explanation of this interaction

15

says that the electron is repelled from other electrons due to their negative charge, but it also attracts the positive ions which form the crystal lattice of the metal. This attraction can deform the positively charged ion lattice in such a way that it attracts other electrons to this source of inhomogeneity of positive charge distribution (see Fig. 8 (b)) – electrons interact through the exchange of phonons. At long distances this attraction between electrons can overcome the electrons' repulsion and cause them to pair-up. The electrons pair-up below the critical temperature $T_s$ to a quantum state with net zero angular momentum and spin which is separated from other possible electron states by a finite energy gap $\Delta$; this microscopic condensation takes place not in the real space but in the momentum space as shown in Fig. 8 (a) [52]. Although single electron is a fermion with spin ½, the superconducting electrons have anti-parallel spins, they form bosons with integer (zero) spin and thus their behavior underlies the Bose-Einstein statistics [50].

Considering one of the topics discussed in this work - $YPd_2Al_3$, it is necessary to mention the basic properties of type-I and II superconductors. These materials reveal two clearly distinguishable kinds of behavior: Type-I superconductors revert from superconducting into normal state when the magnetic field exceeds critical field $H_C$ ($T$). On the other hand, type-II superconductors exhibit two critical magnetic fields - $H_{C1}$ ($T$) and $H_{C2}$ ($T$) where $H_{C2}$ ($T$) > $H_{C1}$ ($T$). The whole specimen is in superconducting state under the first critical field and it reverts in a normal state above the second critical field, but when the applied field is between $H_{C1}$ ($T$) and $H_{C2}$ ($T$), the magnetic field penetrates partially into the material leading to a complicated microscopic structure of both normal and SC regions, known as mixed state. The elementary BCS prediction for critical magnetic field is often expressed as the empirical square law:

$$\mu_0 H_{C2}(T) = \mu_0 H_{C2}(0) \left[ 1 - \left( \frac{T}{T_S} \right)^2 \right] \tag{31}$$

BCS theory is originally a weak-coupling theory which is fulfilled for low temperature superconductors with weak electron-phonon interactions [22,53], so the deviations from the square law are not negligible in the strong-coupling superconductors, such as mercury [54]. The critical field $\mu_0 H_{C2}(0)$ can be determined also from Werthamer-Helfand-Hohenberg (WHH) formula [55] within the weak-coupling BCS theory:

$$\mu_0 H_{C2}(0) = -0.693 \left( \frac{dH_{C2}}{dT_{T=T_S}} \right) T_S \tag{32}$$

The superconducting coherence length $\xi(0)$, which can be interpreted as the length scale on which the superconducting order parameter [2] $\psi$ changes considerably. The coherence length $\xi(0)$ based on Ginzberg-Landau formula [2,50] for an isotropic three-dimensional superconductor can be derived from the upper critical field using equation:

$$\mu_0 H_{C2}(0) = \frac{\Phi_0}{2\pi\xi(0)^2} \tag{33}$$

16

The transition into SC state is observable also in specific heat data. The weak-coupling BCS theory predicts a discontinuity in the specific heat [22]

$$\frac{C_s - C_n}{C_n}\bigg|_{T_S} = \frac{\Delta C_p}{\gamma T}\bigg|_{T_S} = 1.43 \tag{34}$$

where $C_s$ and $C_n$ represent specific heat in the SC and normal state, respectively; $\gamma$ represents the Sommerfeld coefficient.
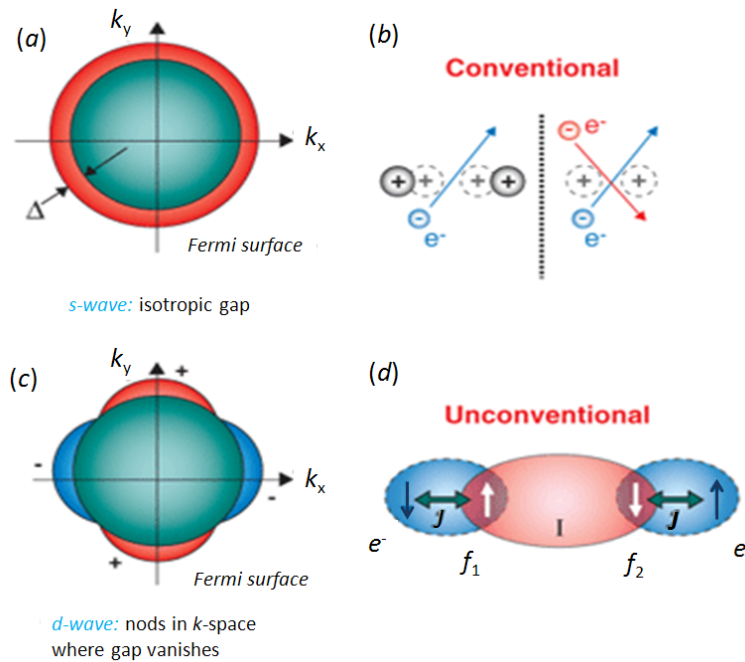


Fig. 8: Forming of the Cooper pair [52].

Soon after the BCS theory was published, an idea of superconductivity without the mediating role of phonons appeared [56]. The BCS theory, based on the charge interaction of quasiparticles, was successful till the discovery of high temperature superconductors by Bednorz and Műller, which exhibited unexpectedly high $T_s \sim 35$ K [57]. More precise theory of superconductivity considering an exotic pairing mechanism was needed due to the research of magnetically ordered superconductors like $UGe_2$ [58,59].

It was suggested, that the superconducting pairing of the conduction electrons in materials with strong Coulomb interaction and magnetism is not mediated by phonons but by a spin-spin interactions [52,60], which depends on the spins of the interacting quasiparticles rather than their charges. Conventional Cooper pair [56] is commonly described as a carrier of *s*-wave superconductivity - a spin singlet state with symmetric form. The idea of formation of an unconventional Cooper pair is described in Fig. 8 (*d*). The pairing is based on an attraction of two conduction electrons which are coupled with localized magnetic moments $f_1$ and $f_2$, respectively. Also the superconducting gap structure becomes more complicated (see Fig. 8 (*c*)), crossing Fermi surface; thus, the Cooper pairs have more freedom for their spin and angular momentum states and their symmetries differ from the concept of a conventional Cooper pair. The *p*-wave spin triplet state is characterized by two-fold symmetry and *d*-wave spin singlet state with four-fold symmetry. Both *p*- and *d*-wave states are characteristic for a system close to the magnetic instability which leads to spin-spin interaction. Positive

interaction with parallel spins (ferromagnetic case) and non-zero total momentum describes the *p*-wave case. The ferromagnetism is expected to be itinerant and therefore carried by the conduction electrons and, as a result, ferromagnetism and superconductivity are carried by the same electrons [59]. The *d*-wave state occurs if the interaction is antiferromagnetic and the total momentum is therefore equal to zero. Considering *s*- and *p*-wave state, the probability distribution function extends over many lattice sites, which is the signature of a weakly bound large-sized Cooper pair reflecting low $T_s$. In contrast, in the *d*-wave case, the probability distribution is concentrated at the nearest lattice site to the origin and quickly decays with distance, which indicates a small Cooper-pair size and correspondingly high $T_s$ [56].

# 3. Selected compounds for physical studies

## 3.1. $RE$Pd$_2$Al$_3$

Discovery of two heavy fermion superconductors UPd$_2$Al$_3$ and UNi$_2$Al$_3$ ($\gamma$ = 150 mJ mol$^{-1}$ K$^{-2}$, $T_s$ = 2 K, $T_N$ = 14 K) [61-63] more than twenty years ago has motivated the studies of physical properties of intermetallic compounds $RE$Pd$_2$Al$_3$. $RE$Pd$_2$Al$_3$ ($RE$ = La, Ce, Pr, Nd, Sm, Gd) compounds are noted for extensity of physical effects such as magnetism, heavy fermion behavior, or superconductivity. $RE$Pd$_2$Al$_3$ represent a broad range of types of magnetic orderings, which are strongly influenced by crystal field interactions [15,19]. The family of $RE$Pd$_2$Al$_3$ compounds crystallize in the hexagonal PrNi$_2$Al$_3$-type crystal structure (space group P6/mmm) [64,65] consisting of $RE$-Pd layers, alternating along the $c$-direction with isolated Al layers as shown in Fig. 9. The lattice parameters for the members of the $RE$Pd$_2$Al$_3$ family are in shown in Tab. 1. The $RE$ atom occupies the highly symmetric position 1$a$, the Pd atoms the position 2$c$ and Al atoms 3$g$ [66].



(a)                                    (b)
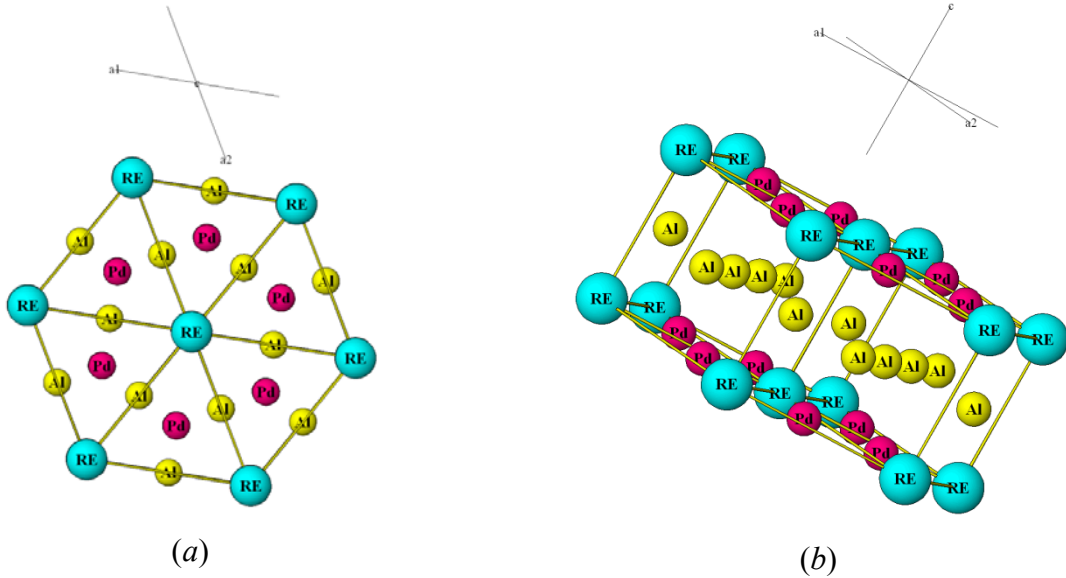
Fig. 9: The structure of $RE$Pd$_2$Al$_3$ compounds oriented parallel (*a*) and perpendicular (*b*) to the basal plane (*RE* is marked by blue, Pd by red and Al by yellow color).

| Compound | $a$ (Å) | $c$ (Å) |
|----------|---------|---------|
| LaPd$_2$Al$_3$ | 5.5082 | 4.2267 |
| CePd$_2$Al$_3$ | 5.4709 | 4.2157 |
| PrPd$_2$Al$_3$ | 5.4569 | 4.2117 |
| NdPd$_2$Al$_3$ | 5.4419 | 4.2069 |
| SmPd$_2$Al$_3$ | 5.4131 | 4.1997 |
| GdPd$_2$Al$_3$ | 5.3924 | 4.1941 |
| UPd$_2$Al$_3$ | 5.3650 | 4.1860 |

Tab. 1: The lattice parameters of the series of $RE$Pd$_2$Al$_3$ compounds [64,65].

The UPd$_2$Al$_3$ and UNi$_2$Al$_3$ compounds exhibit coexistence of superconductivity and antiferromagnetic ordering with relatively high magnetic moment 0.85 $\mu_B$ [61] on U site. Recently, the UPd$_2$Al$_3$ compound has been shown to exhibit NFL behavior when uranium is partially replaced by yttrium [67]. Chemical substitution with yttrium in place of uranium results in a suppression of the magnetic order and the superconductivity U$_{1-x}$Y$_x$Pd$_2$Al$_3$.

Non-magnetic analog LaPd$_2$Al$_3$ shows a superconducting transition at temperature 0.8 K [68].

The HF CePd$_2$Al$_3$ compound ($\gamma = 380$ mJ mol$^{-1}$ K$^{-2}$) orders antiferromagnetically below 2.8 K and reveals a strong Kondo effect [16,69,70]. A Schottky anomaly around 15 K was observed in heat-capacity studies [15]. The ground state, the first and second excited state are doublets; the first excited state appears at 32 K and the second at 800 K [15,64]. The effective magnetic moment per Ce ion is 2.42 $\mu_B$ [71].

PrPd$_2$Al$_3$ compound remains paramagnetic down to 1.5 K, again a Schottky anomaly around 25 K, resp. 30 K was observed [15,72,73]. The ground state is a singlet, the first excited state is doublet at $\sim 60$ K [73]. The value of the effective magnetic moment per Pr ion is 3.45 $\mu_B$ [64].

NdPd$_2$Al$_3$ compound ($\gamma < 20$ mJ mol$^{-1}$ K$^{-2}$) [70] undergoes an antiferromagnetic transition around 6.5 K [15]. The effective magnetic moment per Nd ion reaches the value of 3.59 $\mu_B$ [16]. The Néel temperature varied from 5.2 to 7.7 K depending on different samples. It shows a linear dependence on the lattice constant $a$, not on $c$, which probably means that the exchange interactions inside the $ab$ plane dominate in the magnetism of this compound [74]. The susceptibility measurements revealed the splitting of $^4I_{9/2}$ multiplet to 5 doublets due to CF effects [64,70].

The experimental data observed for SmPd$_2$Al$_3$ point to a complex phase diagram in the temperature range below 12 K characterized by multiple magnetic phase transitions at 3.4, 3.9, 4.4 and 12.4 K, which were revealed in specific heat data and partially also in magnetic and resistivity measurements. The measurements reveal also strong uniaxial magnetocrystalline anisotropy with easy magnetization direction along the $c$-axis. The SmPd$_2$Al$_3$ magnetism is characterized by a small Sm magnetic moment 0.19 $\mu_B$ and strongly influenced by the crystal field interactions and higher multiplets $J = 7/2$ and 9/2.

GdPd$_2$Al$_3$ reveals also a complex magnetic phase diagram which has been conceived in terms of a two-dimensional triangular lattice antiferromagnet with magnetic phase transitions at 13 and 16 K [75,76]. The effective magnetic moment reaches a relatively huge value of 8.13 $\mu_B$ [76].

The studies of YPd$_2$Al$_3$, a new member of the $RE$Pd$_2$Al$_3$ family, have not been carried out yet.


## 3.2.  Ce$_n$T$_m$In$_{3n+2m}$

The heavy fermion series Ce$_n$T$_m$In$_{3n+2m}$ ($n = 1, 2$; $m = 1$; $T =$ Co [77,78], Rh [79,80], Ir [77]) has been intensively studied for more than the past ten years. These compounds exhibit enhanced effective mass of conduction electrons and display a number of unusual electronic properties including phenomena like interplay between superconductivity and magnetism, unconventional superconductivity, NFL behavior, quantum criticality and others [6,79]. The ground state of this system can be tuned by doping or pressure to the vicinity of the QCP [30].

The family of $Ce_nT_mIn_{3n+2m}$ crystallizes in $Ho_nCo_mGa_{3n+2m}$ tetragonal structure (space group P4/mmm), see Fig. 10 and Tab. 2. It can be viewed as a quasi-2D structure of $m$ layers of $TIn_2$ growing along the $c$-axis alternating with $n$ layers of the compound $CeIn_3$ [81]. The structure of compounds with $n = 1$, so-called 115 compounds, exhibits 2D character more strongly than the structure of so-called 218 compounds where $n = 2$. The effect of varying dimensionality of the crystal structure leads to changes of electronic properties between 218 and 115 compounds.



$RE$In$_3$

$RET$In$_5$

$RE_2T$In$_8$

$RET_2$In$_7$
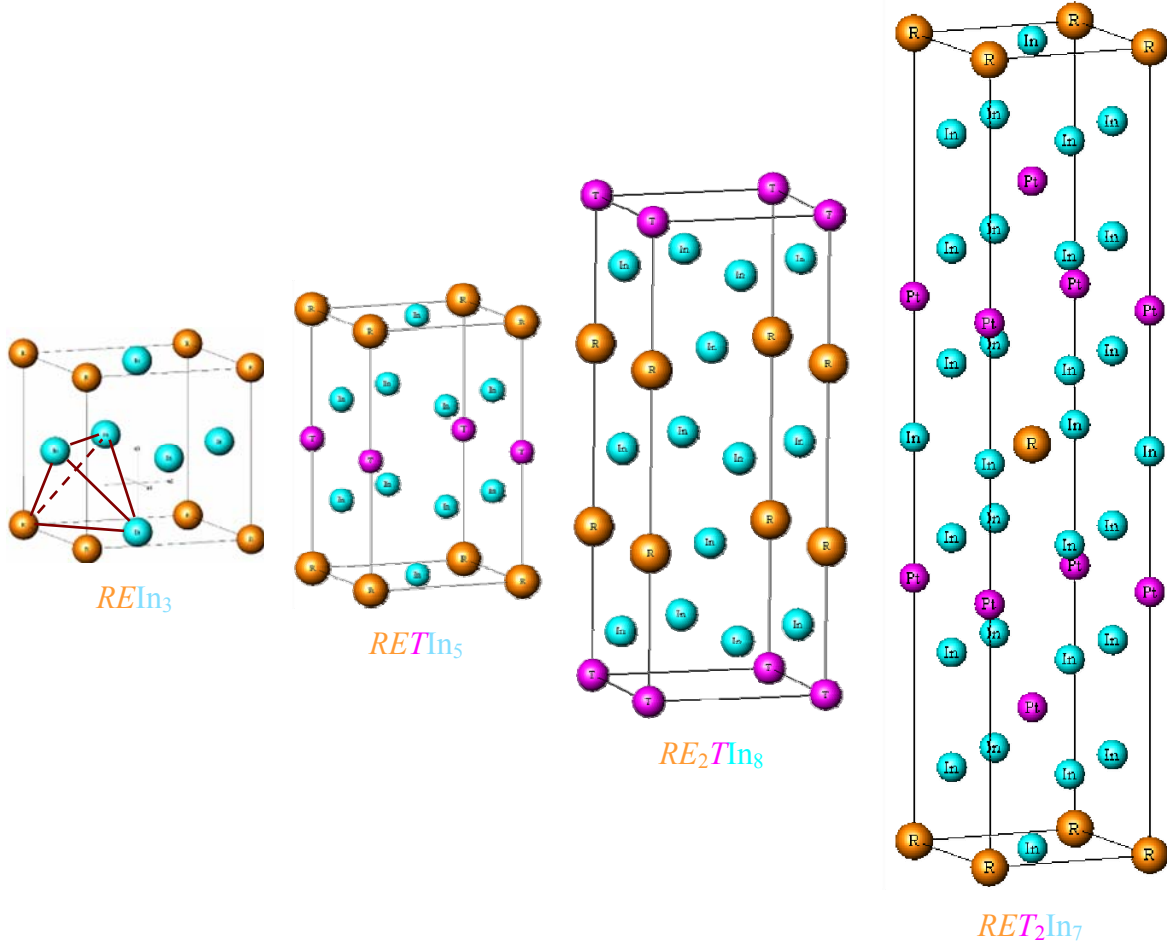
Fig. 10: The structure of $RE_nT_mIn_{3n+2m}$ compounds.

## CeIn$_3$

The compound CeIn$_3$, which represents a basic building element of $Ce_nT_mIn_{3n+2m}$ family, crystallizes in the cubic AuCu$_3$ crystal structure (Pm3m). CeIn$_3$ orders antiferromagnetically below $T_N = 10.2$ K [82] with the magnetic $q$-vector (½, ½, ½) and becomes superconducting under pressure [83] as shown in the phase diagram (see Fig. 11). In fact, CeIn$_3$ is one of the very few systems for which the pressure and magnetic field dependences of the resistivity are in good agreement with the predictions of an antiferromagnetic QCP [84].

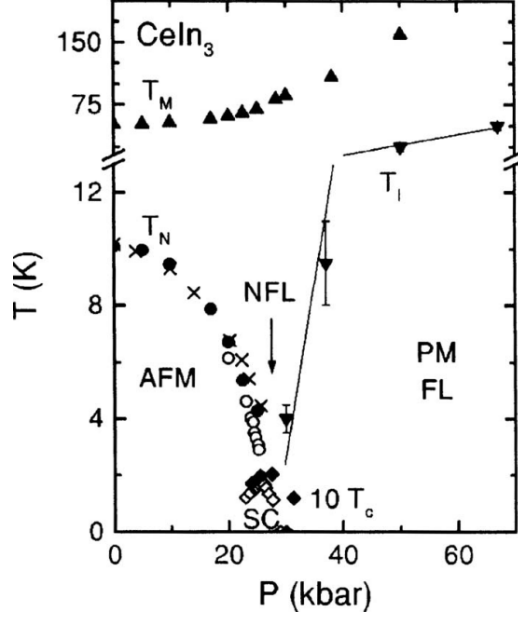Fig. 11: The temperature-pressure phase diagram of $CeIn_3$ ($T_N$ is Néel temperature; $T_M$ indicates the temperature of the maximum of the resistivity curve and $T_I$ the transition temperature to the Fermi liquid regime. The superconducting transition temperature $T_C$ is scaled by a factor 10. After Knebel et al. [85].

| $Ce_nT_mIn_{3n+2m}$ | $a$ (Å) | $c$ (Å) | $c/a$ | $T_s$ (K) | $T_N$ (K) | $p_N$ (GPa) | Ref. |
|---|---|---|---|---|---|---|---|
| $CeIn_3$ | 4.69 | 4.69 | 1 | 0.19 | 10.2 | 2.5 | 7 |
| $CeCoIn_5$ | 4.614 | 7.552 | 1.6367 | 2.3 | - | - | 7 |
| $CeIrIn_5$ | 4.668 | 7.515 | 1.6099 | 0.4 | - | - | 7 |
| $CeRhIn_5$ | 4.652 | 7.542 | 1.6212 | 2.12 | 3.8 | 1.7 | 7 |
| $Ce_2CoIn_8$ | 4.643 | 12.250 | 2.6384 | 0.4 | - | - | 86 |
| $Ce_2IrIn_8$ | 4.671 | 12.214 | 2.6149 | PM down to 50 mK | - | - | 87 |
| $Ce_2RhIn_8$ | 4.665 | 12.244 | 2.6240 | 0.9 | 2.8 | ~ 1.8 | 87,88 |
| $Ce_2PdIn_8$ | 4.695 | 12.210 | 2.6006 | 0.69 | - | - | 21 |

Tab. 2: The structural and physical properties of $Ce_nT_mIn_{3n+2m}$ compounds.

## Ce$T$In$_5$

CeCoIn$_5$ is an ambient pressure $d$-wave superconductor exhibiting many unusual properties. The compound reveals strong antiferromagnetic correlations which enhance the effective electron mass, but the superconducting state is established before the magnetic order can prevail. The variation in the specific heat and thermal conductivity with fourfold symmetry for the magnetic field in the basal plane [89,90] and further measurements [77] point to an unconventional form of superconductivity given by $d_{x^2-y^2}$ pairing. CeCoIn$_5$ features an unusual magnetic field-temperature phase diagram; the transition from normal to superconducting state is first-order but further cooling leads to another second-order transition to superconducting state, called Q-phase [78]. NFL behavior appears in the normal state suggesting the vicinity of CeCoIn$_5$ to an antiferromagnetic QCP [91]. The NFL characteristics retains even in applied magnetic field till the second critical field $H_{c2}$ is reached and the Fermi liquid (FL) behavior is recovered [92].

CeIrIn$_5$ is another ambient pressure superconductor. The superconducting temperature increases with applied pressure and this increase is consistent with the observed decrease in $\gamma$, which may be interpreted as an increase in the characteristic spin fluctuation temperature[93]. The susceptibility and resistivity measurements point to NFL behavior of the normal state[77].

CeRhIn$_5$ orders antiferromagnetically at ambient pressure in contrast to CeCoIn$_5$ and CeIrIn$_5$ and reveals a nontrivial magnetic structure for the magnetic field applied along the $a$-axis[94-96] The ground state of CeRhIn$_5$ is an incommensurate antiferromagnet with $q = (\frac{1}{2}, \frac{1}{2}, 0.297)$ and with magnetic moments oriented helicoidally in the basal plane[94]; in higher magnetic fields $T_N$ increases and two magnetic field-induced transitions at $T_1$ and $T_2$ appear. The phase transitions divide the phase diagram into several regions, which differ in magnetic structure as shown in Fig. 12. Between $T_N$ and $T_2$ the magnetic moments change the helicoidal ordering (region II) to elliptical one (region I) and the structure differs from the ground state in size of magnetic moments. A commensurate antiferromagnetic structure with $q = (\frac{1}{2}, \frac{1}{2}, \frac{1}{4})$ emerges in the high field phase in region III under $T_1$. $T_N$ decreases as the field is applied along the $c$-axis.

While the long-range antiferromagnetic order of CeCoIn$_5$ and CeIrIn$_5$ can be established only by doping, ambient pressure antiferromagnet CeRhIn$_5$ becomes superconducting under pressure and by doping[79,97-99]. Pressure reduces the distances of Ce $4f$ ligands in CeRhIn$_5$ increasing their overlap[100]. The magnetically ordered (MO) state of Ce $4f$ moments is preferred at lower pressures and $T_N = 3.8$ K initially increases slightly with pressure (see Fig. 13 for details). The increase stops above 0.5 GPa where pressure-induced bulk superconductivity appears and coexists with MO state. Similar to other heavy fermion superconductors, magnetism and superconductivity coexist when magnetism appears first at higher temperature and superconductivity is followed at lower temperature. As soon as the two characteristic temperatures $T_N$ and $T_s$ become equal ($\sim 2$ K) at $p_1 \sim 1.75$ GPa, magnetism disappears and only superconductivity (with properties consistent with a $d$-wave gap with line nodes[101]) is observed at higher pressures[80,100]. Specific heat measurements under pressure and magnetic field reveal a phase boundary separating homogeneous volume superconductivity and a phase coexistence of antiferromagnetic order and superconductivity[80]. Specific heat measurements under pressure and field inside the superconducting dome reveal a line of quantum phase transitions between SC state and the coexisting states of SC and field-induced magnetism[80].
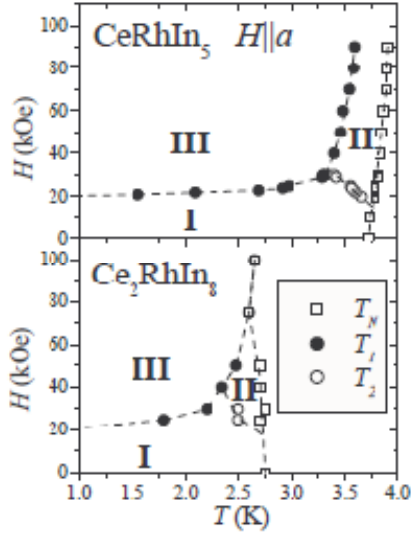
Fig. 12: Temperature vs magnetic field phase diagrams of CeRhIn$_5$ and Ce$_2$RhIn$_8$, $T_N$ corresponds to the antiferromagnetic ordering temperature; $T_1$ and $T_2$ correspond to field-induced first- and second-order transitions respectively. The dashed lines are guides to the eyes. After Cornelius *et al.* [96]
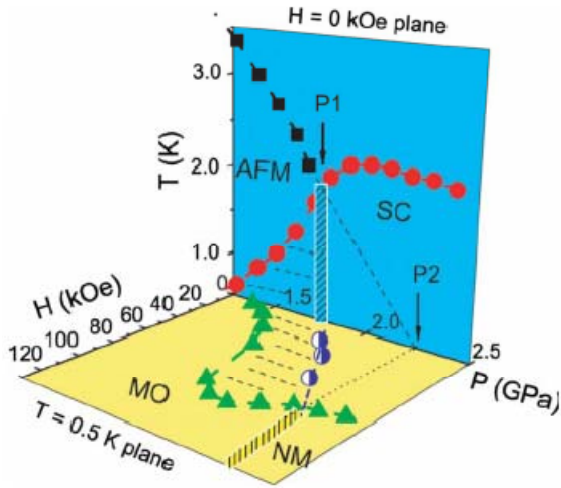


Fig. 13: The *H-T-p* phase diagram of CeRhIn$_5$. The *T-p* plane is at $H = 0$ and the *H-P* plane is for $T = 500$ mK. In the *H–P* plane, upper critical fields $H_{c2}$ where SC state is totally depressed are represented by green triangles. Quantum phase transitions between the pure SC phase and the coexistence phase of *H*-induced magnetism and SC are shown as semi-filled circles. Pressure $p_1$ marks a quantum phase transition point between SC + MO and SC phases at zero magnetic field. Pressure $p_2$ is a tetracritical point where the $H_{c2}$ line and the MO to NM (non-magnetic) lines cross. The dashed line between $p_1$ and $p_2$ is a fit to the data. After T. Park *et al.* [80].

## Ce$_2$*T*In$_8$

The properties of the 218 compounds are similar to those of 115 in many ways. Ce$_2$*T*In$_8$ seems to be less anisotropic than the single-layered Ce*T*In$_5$.

Similar to CeCoIn$_5$, also Ce$_2$CoIn$_8$ undergoes a superconducting transition, but at lower temperature, $T = 0.47$ K. The compound shows non-Fermi liquid behavior above $T_s$ pointing to the vicinity of the quantum critical point [86,102] as CeCoIn$_5$.

Ce$_2$IrIn$_8$ stays paramagnetic down to 50 mK and reveals field-induced NFL behavior [87,103].

The magnetic phase diagram of Ce$_2$RhIn$_8$ at ambient pressure is reminiscent of that of CeRhIn$_5$ [96]. The antiferromagnetic structure of Ce$_2$RhIn$_8$ can be described by the magnetic *q*-vector (½, ½, 0) and by the deviation 38° of magnetic moments from the *c*-axis [104]. A second antiferromagnetic transition is observed in the resistivity at $T_{N2} = 1.65$ K. This anomaly marks a transition from commensurate to incommensurate magnetically ordered state, which shows hysteretic behavior and, therefore, appears to be a first-ordered

24

transition [105]. Hydrostatic pressure suppresses both $T_{N1}$ and $T_{N2}$; $T_{N2}$ vanishes below 0.1 GPa and therefore is not supposed to affect the emergence of superconductivity; $T_{N1}$ extrapolates to zero around $p = 3.2$ GPa [99], suggesting a quantum critical point as in CeRhIn$_5$. In some Ce$_2$RhIn$_8$ samples showing superlattice reflections, ambient pressure superconductivity was reported recently [106]. A superstructure in Ce$_2$RhIn$_8$ is induced by the presence of the stacking faults observed by high-resolution neutron diffraction [107].

**Substitutional doping in Ce$_2T$In$_8$ and Ce$T$In$_5$ compounds**

The series CeCo$_{1-x}$Ir$_x$In$_5$ allows the study of the evolution between two unconventional superconductors. Cobalt doping of CeIrIn$_5$ induces two anomalies as shown in Fig. 14 [108] - superconducting transition at $T_s$ and a transition at $T_?$, whose origin is still not clear. In series Ce$_2$Co$_{1-x}$Ir$_x$In$_8$, increasing cobalt doping enhances anomaly at $T_?$ with similar character to the 115 equivalent [97].



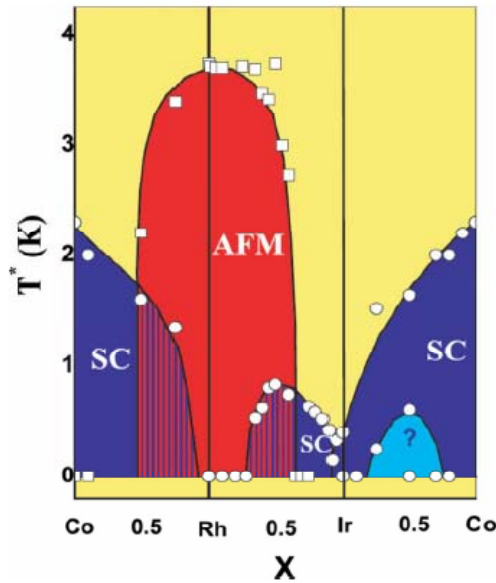Fig. 14: Evolution of the superconductivity and antiferromagnetism in the series Ce$T$In$_5$. After Pagliuso, Movshovich [108].

In the series Ce$_n$Co$_{1-x}$Rh$_x$In$_{3n+2}$ and Ce$_n$Rh$_{1-x}$Ir$_x$In$_{3n+2}$ the substitutional doping allows the study of the evolution between superconductivity and antiferromagnetism [7]. The superconductivity seems to be insensitive to the disorder associated with the doping, concerning the 115 compounds [7]. Doping of Ce$_2$RhIn$_8$ by Ir at the Rh site smoothly suppresses the magnetism into a paramagnetic heavy state with no evidence for a phase transition at ambient pressure [109] whereas doping by Ir at the Rh site of CeRhIn$_5$ gradually suppresses AF order and simultaneously induces SC state, which results in an overlapping region of SC and AF as shown in Fig. 14. Temperature $T_N$ is relatively insensitive on the Ir doping till the SC state emerges and then it decreases rapidly [110,111]. Similar effect is caused also by Co doping on Rh site of both 218 and 115 compounds [97,112].

Substitutional doping of Ce and In in CeRhIn$_5$ and Ce$_2$RhIn$_8$ has been carried out with La, Sn and Cd. La doping at the Ce-site in CeRhIn$_5$ and Ce$_2$RhIn$_8$ causes the suppression of magnetic order and emergence of the NFL behavior [108,113]. Cd doping at the In site of CeRhIn$_5$ reduces the $T_N$ first but higher concentrations of Cd lead to its further increase [113]. On the opposite, rising amount of Cd atoms on the In positions in Ce$_2$RhIn$_8$ enhances the AF state [114].

Sn doping at the In-site causes the suppression of magnetic order and no further increase of $T_N$ [115].

**Ce$_2$PdIn$_8$ and CePt$_2$In$_7$**

The family of Ce$_n$$T_m$In$_{3n+2m}$ compounds was enriched by two new discoveries in 2008. The heavy fermion compound CePt$_2$In$_7$ was presented as a new structure type with a tetragonal structure (I4/mmm) formed by two layers of PtIn$_2$ and one layer of CeIn$_3$ (as shown in Fig. 10) connecting this compound with the Ce$_n$$T$In$_{3n+2}$ family [116]. CePt$_2$In$_7$ reveals stronger 2D-character than Ce$T$In$_5$ due to the doubled $T$In$_2$ layer in the structure [117]. CePt$_2$In$_7$ is a commensurate antiferromagnet below 5.2 K [117] exhibiting pressure-induced SC; there is a region of pressures $1 \leq p \leq 3$ GPa where both phenomena coexist [14].

Ce$_2$PdIn$_8$ with Ho$_2$CoGa$_8$ type structure was first reported by Shtepa $et$ $al.$ [12]. The original studies on polycrystalline Ce$_2$PdIn$_8$ reported that the compound was paramagnetic down to the lowest temperatures ($\sim 0.4$ K) with NFL behavior below 6 K [13]. Further studies on single crystals revealed heavy fermion superconductivity below $T_s \sim 0.7$ K, however, the crystals contained CeIn$_3$ as an impurity phase [9-11].

Single crystals of Ce$_2$PdIn$_8$ have been grown by solution growth method [9-11,21]. There is a strong tendency of initial growth of CeIn$_3$ while Ce$_2$PdIn$_8$ growths on top of it, as shown in Fig. 15. Since the boundary between these two phases is well defined the separation of Ce$_2$PdIn$_8$ is possible [21]. The studies of single phase Ce$_2$PdIn$_8$ single crystals confirm the superconductivity and NFL behavior, however the critical temperature was found to be sample dependent $T_s = 0.45$ - $0.68$ K. This behavior was ascribed to structural defects such as stacking faults [21] presented for Ce$_2$RhIn$_8$ [107]. Up to now, the only single-phase samples presenting well defined SC transition at 0.69 K were polycrystals; annealing process seems to play important role for the superconductivity [20]. Recent studies [118] of polycrystalline Ce$_2$PdIn$_8$ in pressures up to 2.1 GPa show that increasing pressure gradually suppresses $T_s$ and pushes the system away from the NFL state.



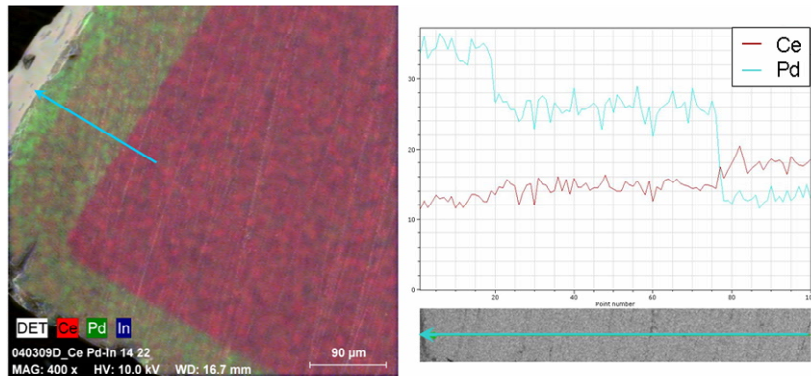Fig. 15: SEM image with elements mapping (EDX) of a CeIn$_3$-Ce$_2$PdIn$_8$ system (left); the line scan along the blue arrow shows a sharpness of the boundary between the CeIn$_3$-Ce$_2$PdIn$_8$ phases (right). After Uhlířová $et$ $al.$ [21,119].

# 4.     Experimental techniques

## 4.1.     Synthesis of intermetallic compounds

**Binary phase diagrams**

It is useful at this moment to explain several important terms considering thermodynamics of binary (for simplicity) alloys. A binary phase diagram is a temperature - composition diagram for two elements. Of course the description can be extended to more (*N*) elements; however the diagram becomes *N*-dimensional and thus more complicated. An example of a binary phase diagram is shown in Fig. 16. The boundary between solid and liquid phase is a *liquidus-solidus* line. It represents a concentration dependence of the melting and solidification temperature of a solution, respectively. At an *eutectic point* (*E*), a liquid phase transforms into two different solid phases. *Peritectic point* (*P*), on the other hand, represents a transformation of a liquid and solid phase into another solid phase.

Compounds can be distinguished depending upon they melt congruently or incongruently. While congruently melting compounds transform from homogeneous solid to homogeneous liquid at melting point, incongruently melting compounds decompose at some temperature to another solid phase and liquid whose composition differs from composition of the original compound.


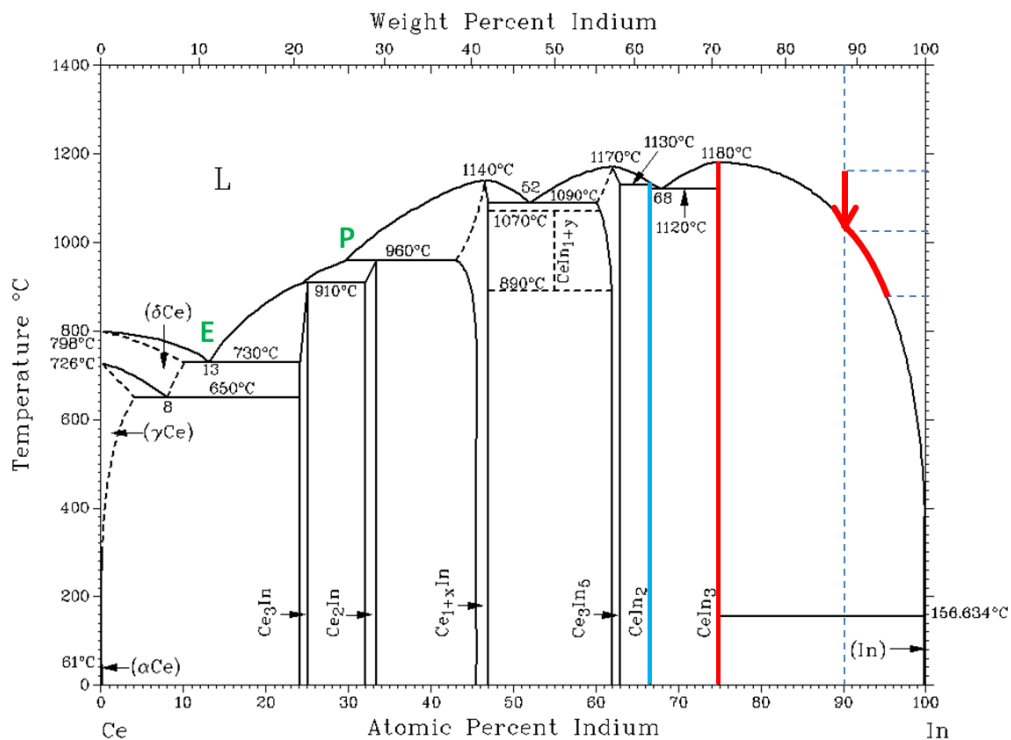
Fig. 16: Ce-In phase diagram [120]. The blue line marks the incongruent growth from a Ce-rich composition; the red line marks the congruent growth producing the phase CeIn$_3$ directly. The red arrow and following red curve show the starting temperature and In-rich concentration of the mixture. The letter *E* marks the eutectic point; letter *P* marks the peritectic point of Ce$_2$In compound.

En example of congruently melting compound is $CeIn_3$. It can be prepared either by crystallization from melt (for example by Czochralski method [121]) or from solution [82]. The red line (see Fig. 16) represents growth from stoichiometric melt, which is used by Czochralski method. As soon as the temperature drops to less than 1180 °C, the liquid transforms into solid of the same stoichiometry. The red arrow represents growth from In-rich composition which produces also single crystals of $CeIn_3$, the method is explained below.

**Purity of metals**

The purity of elements is usually expressed in percentages. Because the number of digits can be rather large, the notation as 4N = 99.99 %, 5N = 99.999 %, etc., is used. In some cases the purity of metal elements is defined on "metals basis", which defines the total amounts of other metallic impurities, but not other elements such as oxygen, nitrogen or carbon. For ultra high purity materials the amount of impurities is often expressed in ppm unit.

## 4.1.1. Polycrystalline samples

Polycrystalline materials show periodical ordering only within small grains, which are randomly oriented and therefore prevent the majority of measurements of anisotropic properties. On the other hand, their uncomplicated synthesis provides a possibility to investigate basic physical properties. Polycrystalline samples can be prepared by arc melting, solid phase reaction, annealing and other methods.

In our case, the synthesis was realized by arc melting in a monoarc furnace and by consequent annealing. The furnace was evacuated to $10^{-3}$ mbar and flushed/filled up with high purity Ar (6N). The elements are placed into the furnace on a copper crucible, which is intensively cooled; the interaction between the sample and the crucible does not take place during melting due to a big temperature gradient which causes an emergence of vapor preventing any contact between the sample and crucible. To let the reaction take place in the whole volume and to homogenize the sample enough, the melting should be repeated several times. After the arc melting the samples are usually annealed while sealed in quartz tube under vacuum ($10^{-6}$ mbar) or Ar (6N) atmosphere. Annealing at certain temperature is important especially for stabilization of incongruently melting phases, but it also helps to decrease inhomogeneities in congruently melting compounds caused by rapid cooling.

## 4.1.2. Single crystal growth techniques

The preparation of single crystals is crucial for the condensed matter physics due to the possibility to investigate anisotropic properties of materials. Generally, single crystals allow measuring of the intrinsic magnetic, transport, thermodynamic and structural properties of the materials. In addition, samples in the form of single crystals provide lower porosity and stress, higher purity and fewer grain boundaries in comparison to polycrystalline materials.

This chapter offers a short review of the most frequent crystal growth methods with special stress on the solution growth technique, which was used in this work to obtain single crystals.

The crystal growth methods are generally classified into three categories: growth from melt, growth from solution and growth from the vapor phase.

### Growth from melt

All materials which melt congruently and do not undergo a phase transformation between the melting point [*] (see Ref. [122]) and the room temperature can be prepared from melt.

The most popular method (especially in the silicon industry) is the Czochralski method [123]. The growth process is carried out under inert atmosphere. The melt is placed in a rotating crucible to achieve better compositional and thermal homogenization. A seed is held by a rod, which is rotating during the growth as well. The seed is pulled into the melt after equilibration. An ingot is slowly pulled out of the melt and the aim is to prefer just one nucleus to form a narrow neck. After that, the neck is widened slowly. Czochralski method provides the possibility to get large crystals at high speeds and high crystalline perfection. Although the growth can be carried out under moderate pressures, it is not suitable for materials whose vapor pressure is high at the melting point.

In another widely used method - zone melting - the charge is contained in a closed container slowly moving through a furnace with appropriate thermal gradient. The crystal starts to grow at one end of the container. Bridgman method is often used as a synonym for zone melting, but there a slight difference which lies in the usage of a container with a tapered end [123]. Shape and size of the crystals, as well as the vapor pressure can be easily controlled during this growth procedure. On the other hand, high densities of lattice defects can occur when the volume expansion is associated with solidification and thus leads to high pressures [123].

Floating zone, technique similar to zone melting, requires vertical configuration without container. The molten zone of a polycrystalline rod is usually formed by oxygen-hydrogen flame or by halogen and xenon lamps, respectively (the rod is then put in the focus of the mirrors with the lamp – so-called optical furnace). The missing container - a potential source of contamination - is the biggest advantage of this method, but materials with high vapor pressure are generally not suitable for it. Floating zone is ideal for obtaining crystals of dielectrics or insulators [123].

### Growth from vapor phase

The growth process involves usually either reversible or irreversible reactions. Reversible reaction is used when the solid material can be brought into vapor phase (hot-wire method [123]). The seed material is brought into contact with the reactants where the irreversible reaction takes place. Growth from vapor phase can be obtained also without involving chemical reactions such as molecular beam epitaxy or sputtering of element materials [123].

These processes are extremely slow but their result is a very high purity material because, generally, gases can be obtained at higher levels of purities than liquids. This procedure is used especially for the growth of thin layers of silicon or semiconductors (GaAs) [123,124].

### Solution growth technique

The solution (- flux) growth is a crystal growth method commonly known from school experiments as a way to grow crystals of table salt or bluestone from water solution. Solution growth applied in solid state research uses several different types of solution, e. g. aqueous, molten salt or molten metal.

---

[*] However in some cases when the crystal undergoes structural transition, a high-temperature phase can be obtained. This is an example of the growth of polymorphic materials such as $PrIr_2Si_2$ by Czochralski method, where the cooling during the growth is fast enough to avoid the transition to the low-temperature phase.

The term "flux" stands for a high temperature solvent which permits growth to proceed at temperatures well below the melting point of the solute phase. We distinguish so-called *self-flux* method for compounds containing the solvent and *true-flux* method for compounds grown from an additional element; the principle of both methods is the same.

**The principle of the flux growth method**

To explain the solution growth method we describe the growth of an incongruently melting phase with a hypothetical phase diagram given in Fig. 17. The desirable phase has a composition $X_{1-m}Y_m$. In this case $X$ and $Y$ can be one or more different elements in fixed ratio. To prepare $X_{1-m}Y_m$ compound we start from Y-richer composition $X_{1-n}Y_n$, which we heat to temperature $T_1$ well above the liquidus line. While cooling through the liquid phase $l$, we reach the liquidus-solidus line (red) at $T_2$. At this point, the solution is saturated and the solution growth can take place. Generally, the saturation can be achieved not only by lowering the solution temperature, which is our case, but also by evaporating the solvent. While further cooling the crystals of $X_{1-m}Y_m$ start growing; the system is no longer homogeneous, instead contains a solid of one stoichiometry and a liquid $l$ of another. The liquid becomes Y richer following the liquidus line. The crystals should be decanted at a temperature $T_3$ before reaching the eutectic point $E$. The relative phase amounts of the crystals and remaining flux are given by lever rule [†] (see Ref. [123-125]). The amount of $Y$ in the starting composition should lie in a range marked by the pink lines in order avoid growth of $X_{1-k}Y_k$. The phase of $X_{1-k}Y_k$ is formed when the liquid is cooled from $T_1$ with composition $X_{1-m}Y_m$; but after the peritectic temperature $T_P$ is reached, $X_{1-m}Y_m$ starts to grow again.
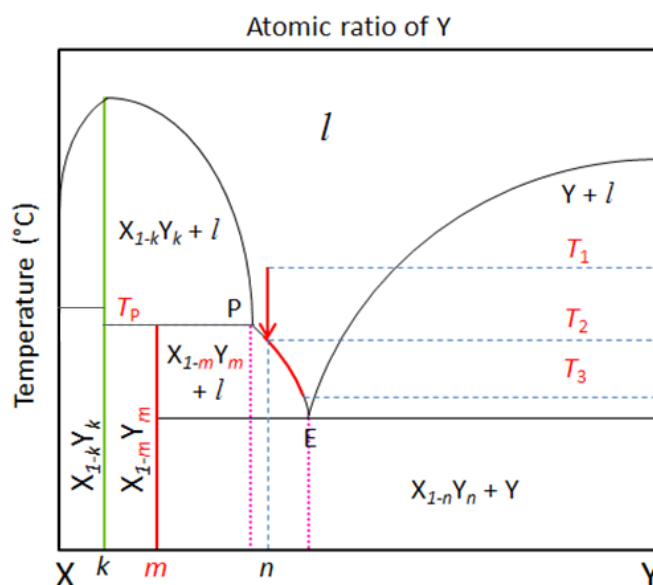


Fig. 17: Binary phase diagram. Points $E$ and $P$ mark eutectic and peritectic points, respectively; $k$, $m$, $n$ together with the green, red and dashed blue vertical lines present different starting ratios of $X$ and $Y$ elements; the blue dashed vertical lines mark the temperatures $T_1$, $T_2$ and $T_3$ which define the cooling regime, while $T_p$ marks the peritectic temperature; the pink dashed lines mark the concentration range suitable for growing $X_{1-m}Y_m$; the red arrow and line present the growth process of $X_{1-m}Y_m$.

---

[†] The lever rule is used to determine weight percentages of liquid and solid phase for given temperature of a binary phase diagram. The distances $l_a$ and $l_b$ along the horizontal tie line of the phase diagram are measured. The lever rule states that $n_a l_a = n_b l_b$, where $n_a$ is the amount of phase $a$ and $n_b$ is the amount of phase $b$.

Appropriate parameters to grow for example CeIn$_3$ compound, shown in Fig. 16, are: $X$ = Ce, $Y$ = In, $m$ = 0.75, $n \sim 0.90$, $T_1 \sim 1150$ °C, $T_2 \sim 1020$ °C. Here, we have only described the self-flux method. The compounds $RET_2Ge_2$ ($T$ = Cu, Ni) are examples of compounds grown from true-flux [126].

**Solution growth – practical aspects**

**Necessary equipment**

The solution growth requires high purity materials, protective environment and a furnace with controllable temperature. The arrangement of our laboratory is in Fig. 18.



(*a*)



(*b*)

Fig. 18: The solution growth laboratory (*a*) equipped by programmable furnaces with high accuracy temperature controller and apparatus for sealing samples under protective atmosphere or vacuum (*b*) and centrifuge.

The elements of given stoichiometry are placed in into an appropriate crucible. For most of intermetallic compounds, high density sintered Al$_2$O$_3$ (alumina) is used. The advantage of alumina is that it is stable against attack from many of the low melting elements used as solutions, however, it is not stable in contact with some elements such as *RE* or Mg. For melts containing *RE* the critical concentration suitable for alumina crucibles is ~ 10 %, otherwise

other materials of the crucibles have to be used (e.g. BN, Ta, Pt) [125]. In this work, high purity alumina crucibles (99.8 % or 99.99 %) were used.

Since metals especially at high temperatures tend to form oxides, the protective environment (atmosphere) is needed. This is mostly realized by sealing the crucibles in an amorphous quartz ampoule. In our case, a bottle gas-oxygen blow torch (see Fig. 19) was used. The ampoules were evacuated down to the pressure of $\sim 10^{-6}$ mbar. The process is shown in Fig. 19.

Rather difficult part of the growth is the right choice of the flux. As it was explain above, we can use a self-flux method for growing compounds where one of the components is suitable to act as flux, however, in many cases another element has to be used for successful growth. The essential requirement of a flux is that it should have a high solubility for the solute, without forming stable unwanted binary phases with the elements which are used. The melt should have a very low solubility or reactivity with the material of the crucible in the whole range of temperatures which are used. Elements as Al, Bi, Ga, In, Pb, Sn and Sb are commonly used as fluxes. More details about their specific properties can be found in work by P.C. Canfield and Z. Fisk [127]. In our work, In was used as a self-flux for the growth of $Ce_nT_mIn_{3n+2m}$ compounds.
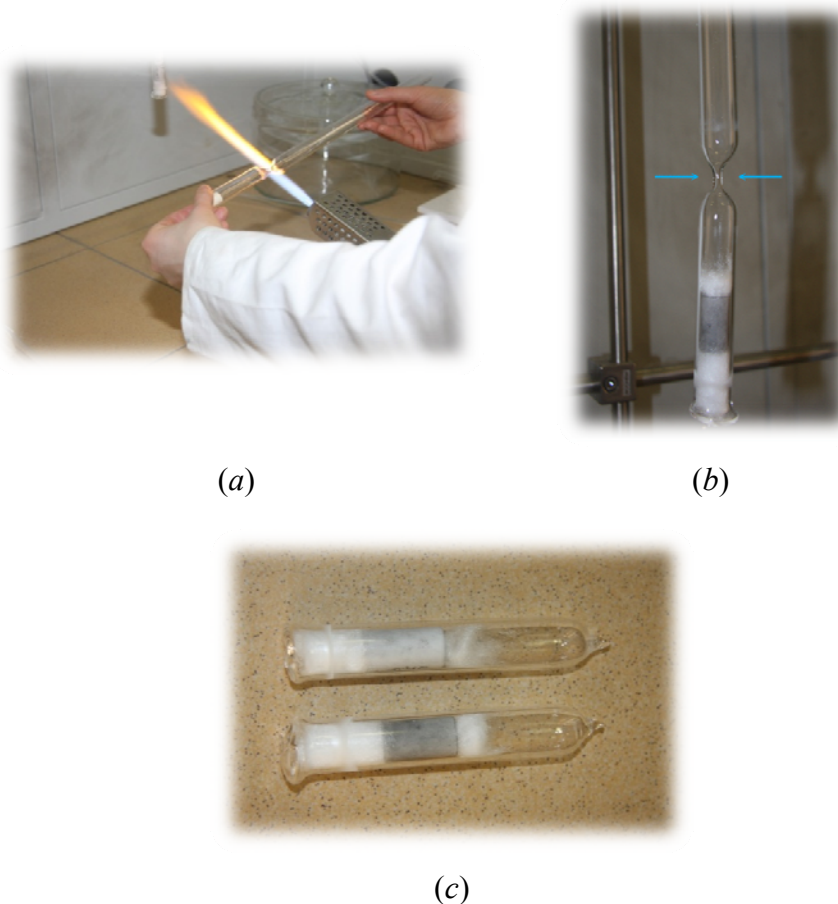
(a)

(b)

(c)

Fig. 19: Necking the quartz tube with the bottle gas-oxygen blow torch (a); the ampoule attached to the pumping system is ready to be sealed by hand torch (b); evacuated ampoules with crucibles (c).

Controllable temperature can be achieved by using furnaces with a programmable temperature controller. Accurate temperature control is essential for stable growth and controllers capable of regulation better than $\pm 0.5\,°C$ are available for this purpose. The temperature stability might be improved by surrounding the ampoule with a ceramic material to increase the thermal capacity, as it was done in our experiments.

The final step is to separate the solution from the crystals that have grown. This can be done mechanically, chemically or using a lab centrifuge with metal cups to hold the ampoule. The centrifugation is the most efficient way how to get rid of the liquid solution; melts up to $\sim 800\,°C$ can be centrifuged without a centrifuge with heating. The samples are quickly removed from the furnace and put to the centrifuge with a fast start. Chemical etching must attack the flux much more quickly than it does the crystals, a proper etchant is not always easy to find. Mechanical removing of the crystals from the solidified flux is not the preferred route, since it is time consuming and the crystals break easily [128]. In our case, most of the indium was decanted in a centrifuge with rotating speed approximately 3500 - 4000 rpm and the remaining flux was etched by concentrated HCl which does not attack the crystals.

**The crystal growth procedure**

Before running the experiment, it is necessary to determine the initial composition of the growth and a temperature profile using phase diagrams or previous experiences.

The consequent process of single crystal synthesis can be realized in many ways, which can slightly differ from each other in technical details; the procedure described in the consequent paragraph was used in our work.

The starting composition of elements is placed into the crucible; the element which acts as a solvent covers the other, higher melting elements. Another crucible, filled with quartz wool, is used to catch the remaining flux while decanting. The quartz wool acts as a filter to separate the solid crystals. The crucibles are put into the quartz tube with flattened bottom to be sealed. After evacuating, the ampoule is placed in a bigger crucible to be kept it in vertical position and finally put into the furnace. The temperature profile has commonly three phases - heating (rather fast $\sim 200\,°C/hour$), delay at constant temperature (to let the melt homogenize) and the growth phase - slow cooling (rates $\sim 1\text{-}10\,°C/hour$ or even slower). The cooling rate affects the size of crystals - usually, the faster cooling, the smaller crystals.

When the crystals are grown, the ampoule is moved quickly to centrifuge. The second crucible catches the remaining flux during centrifugation.

# 4.2. Characterization methods

## 4.2.1. X-ray diffraction

### Powder diffraction

X-ray powder diffraction is a fundamental technique for structural characterization of poly- and single-crystalline samples. It allows distinguishing different phases in a multiphase samples as well. We have prepared polycrystalline samples, pulverized them into a fine powder and uniformly spread the powder on the silicon plate. The measurement of $Ce_n(Rh,Pd)In_{2n+3m}$ was performed on a Bruker D8 Advance diffractometer [129] with classical Bragg-Brentano setup [130] and Cu $K_\alpha$ radiation ($\lambda = 1.540562$ Å). The measurement of $YPd_2Al_3$ was done using Seifert XRD 7 diffractometer with similar equipment.

The data were analyzed using FullProf/WinPlotr software [131] based on Rietvield technique [130]. Rietvield method is based on the method of least squares.

**Single-crystalline diffraction**

The structure with emphasis on the lattice parameters of single crystals of $Ce_n(Rh,Pd)In_{2n+3m}$ was analyzed. The analysis was done by recording multiple images with a large area X-ray detector [132], as the single crystal was rotated in the X-ray beam. The measurement was performed using X-ray diffractometer RIGAKU RAPID II [132].

**Laue method**

Laue method was used mainly to determine the quality and orientation of the single crystals. Continuous spectrum of Cu radiation interacts with the sample and the diffracted beam is registered on a plane film. The diameter of the film was 10 cm and distance of the sample from the film was 3 cm. The sample was mounted on a goniometrical head shown in Fig. 20. The Laue patterns were taken on Micrometa 600 apparatus with polychromatic Cu-radiation. An example of the pattern ($CeRhIn_5$ single crystal) is presented in Fig. 20.



(*a*)    (*b*)

Fig. 20: Goniometric head (*a*) and Laue pattern (*b*) of $CeRhIn_5$ single crystal with the *a*-axis oriented perpendicular to the image plane.

## 4.2.2. Scanning electron microscope

Scanning electron microscope (SEM) images the sample surface by scanning it with a high-energy beam of electrons in a raster scan pattern. The types of signals produced by an SEM include secondary electrons (SE), back-scattered electrons (BSE) and characteristic X-ray radiation. The signals of SE result from interactions of the electron beam with atoms at or near the surface of the sample, so they provide information about surface topography. BSE are beam electrons that are reflected from the sample by elastic scattering. Because the intensity of the BSE signal is strongly related to the atomic number $Z$ of the specimen, BSE images can provide information about the distribution of different elements in the sample. The measurement was performed on Tescan Mira I LMH SEM [133]. The microscope is equipped with SE detector, BSE detector and with energy dispersive x-ray analyzer (EDX) Bruker AXS. EDX allows measuring the elemental composition of the specimen by analyzing emitted X-rays characteristic of the difference in energy between the two shells. EDX was used to check the stoichiometry of the specimens on several faces and also on the cut.

# 4.3.　　Thermal analysis measurements

Generally, thermal analysis [134] investigates a change of properties of a sample, related to an imposed temperature alternation. Classical thermal analysis measures time dependence of temperature to register the released or absorbed heat during a phase transition (crystallization, glass transitions, melting, thermal decomposition, sublimation, structure and magnetic transitions...). On the other hand, differential thermal analysis represents a much more sensitive method, based on measuring of the temperature difference of the sample and reference. DTA is a technique used for the determination of phase diagrams, which may be applied to fluxed melts. It was found that DTA can lead to optimization of the growth without detailed knowledge of phase diagrams and can play a role in selecting the right crucible material [124]. Differential scanning calorimetry (DSC) measures the energy needed to compensate the temperature difference between the sample and reference. The DTA device is more adapted to qualitative measurements (determination of transition temperature) and the DSC device to quantitative measurements of heat. Thermogravimetry (TG) measures changes in sample mass with temperature using thermobalance. The thermomechanical analysis (TMA) aims at measuring variations of a sample's dimensions as a function of temperature [134].

The measurement was performed using SETSYS Evolution 24 instrument by SETARAM Instrumentation Company. The apparatus allows measuring i. a. with TG, TMA, DTA and DSC device hooked to the balance [135]. Simultaneous TG-DTA/DSC enables measuring both heat flow and weight changes in a material as a function of temperature or time in a controlled atmosphere. Simultaneous measurement of these material properties simplifies interpretation of the results. The complementary information obtained allows differentiation between endothermic and exothermic events which have no associated weight loss (e.g., melting and crystallization) and those which involve a weight loss (e.g., degradation). In our measurements, we used the TG-DTA option; however, the data from thermogravimetry are not presented because did not reveal any relevant information concerning the transition temperatures. As a crucible, we used the standard alumina crucibles with diameter 0.5 cm and height 1 cm. The corresponding baseline (measured with an empty crucible) was estimated for all experiments and subtracted from the data. The onset, offset and maximum temperatures of the peaks were estimated using the SETARAM software.

# 4.4.　　Magnetic measurements

The measurements of magnetization, DC and AC susceptibility were performed using Physical Property Measurement System (PPMS) and Magnetic Property Measurement System (MPMS – SQUID = Superconducting Quantum Interference Device) by Quantum Design Company [136,137]. Magnetization and AC/DC susceptibility were measured in the temperature range of $1.8 - 300$ K in magnetic fields up to 14 T on PPMS 14T and in the temperature range of $1.8 - 300$ K in magnetic fields up to 7 T on MPMS 7T. Magnetization was measured partially using SQUID and vibrating sample magnetometer (VSM) on PPMS 9T. VSM operates in frequency range from 1 to 400 Hz (40 Hz is used most frequently) and oscillation amplitude $1 - 3$ mm. For the AC susceptibility measurement, a home-made AC magnetometer was used to estimate the temperature of the macroscopic transition into the superconducting state. AC magnetometer is suitable for measurements in temperature range $0.35 - 400$ K using Helium-3 option devices. A comparable piece of tin was used as a standard for the measurement with the home-made AC magnetometer.

# 4.5. The effect of demagnetizing factor

As mentioned earlier, the samples prepared and measured in this work were usually flat and rectangular shaped, as the result of the growth in layers. Generally, the shape of specimen affects through the demagnetizing factor measurement in magnetic field. The magnetization $M$ within the magnetic specimen induces demagnetizing field $H_D$, which is proportional to the specimen's magnetization: $H_D = nM$. Here $n = n_x + n_y + n_z = 1$ is the demagnetizing factor, which depends on the shape of the specimen, $n_i$ mark components of the demagnetizing factor. If the specimen is located in an external magnetic field $H_{ext}$, then the internal field $H_{int}$ in the specimen is equal to [2,138]

$$H_{int} = H_{ext} - nM \,. \tag{35}$$

The demagnetizing factor appears also in description of behavior of superconducting materials. Let us define the external susceptibility $\chi_{ext} = dM/dH_{ext}$ and internal susceptibility $\chi_{int} = dM/dH_{int}$. From equation (35) we get [139]

$$\chi_{ext} = \chi_{int}/(1 + n\chi_{int})$$
$$\chi_{int} = \chi_{ext}/(1 - n\chi_{ext}). \tag{36}$$

Assuming a simple type-I superconductor is a perfectly diamagnetic material ($\chi_{int} = -1$) the previous equation for $\chi_{ext}$ would simplify to

$$\chi_{ext} = 1/(n - 1). \tag{37}$$

Considering a superconducting ellipsoid, a type-I superconductor, in a uniform magnetic field we get equation [140,141]

$$H = \frac{H_{ext} \sin \vartheta}{1 - n} \tag{38}$$

where $\vartheta$ presents an angle between the direction of the external field and the principal axis of the rotational ellipsoid. The field outside the surface will reach the critical value for destruction of superconductivity in some places when $H_{ext} = (1 - n)H_c$ where $H = H_c$ is the critical field. It may seem that this field should create a non-superconducting region around the equator, but instead of that, the ellipsoid splits up into some arrangement of normal and superconducting regions - domains. This state, which occurs only in the type-I superconductors, is called intermediate state. The specimen is superconducting and ideal diamagnetic in the Meissner state until a specific external field given by the demagnetizing factor makes it overpass to intermediate state.

Theoretical values of the demagnetizing factor for several idealized objects are shown in Tab. 3 and on the magnetization curves (see Fig. 21):
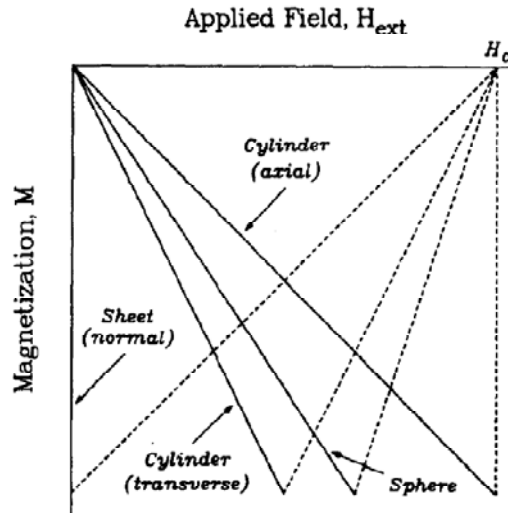


Fig. 21: Ideal reversible magnetization curves as a function of applied field $\boldsymbol{H}_{ext}$. The curves correspond to type-I superconductors. The external susceptibility $\chi_{ext}$ is given by the slopes of the solid lines; flux penetration for the intermediate state is marked by the dashed lines. After R. B. Goldfarb [139].

We have measured lead specimens of rectangular shape (1.4×2.3×0.2 mm) placed parallel and perpendicular to the external magnetic field using MPMS 7T, which correspond to the size and shape of our samples and a thin rod (length ~ 5.1 mm, diameter ~ 0.4 mm) to compare (see Fig. 22):
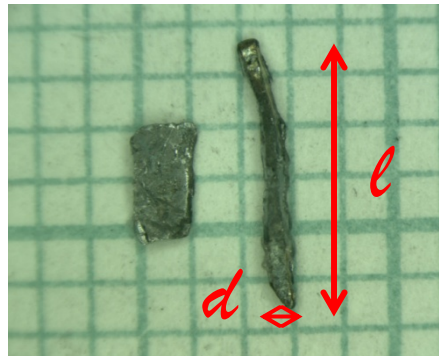


Fig. 22: Measured lead samples. The dimensions of the rod described in the figure are discussed in context of demagnetizing factor (see Tab. 3).

The critical magnetic field of lead is 80.4 mT at $T = 0$ K (according to equation (31)) and the critical temperature is 7.2 K [142]. Before the measurements the lead samples (Pb - 99.999 %) were annealed for 3 days at 200 ºC to avoid any possible stress in the samples. The magnetization was measured at 2 K ($\mu_0 H_c = 74.6$ mT [143]). The demagnetizing factors obtained from this measurement are presented in Tab. 3 and in Fig. 23. Demagnetizing factor decreases strongly when the plate is reoriented parallel to the field and the thin rod approaches the ideal case. Although the experimental values of demagnetizing factors for the rod and plate parallel to the field correspond to their theoretical equivalents well, the experimental value for plate oriented perpendicularly differs strongly from the expected one. This difference is caused probably by the real shape of the sample in this dimension, which is

far away from the idealized assumption (very thin plate). The inaccuracy of the sample orientation in the magnetic field (due to complicated fixation of the plate perpendicularly on the sample holder) could also play a role. The irregularities on the curves are caused most likely by the nonideal shape of samples. Another reason for the deviation from the theoretical character of the curves could be the remanent field of the superconducting magnet. After the magnet is set to zero field, there will be some magnetic field trapped in the magnet. This residual field is usually relatively small (0.1 to 2 mT), however, to make measurements at the lowest fields, it is important to determine the offset due to the remanent field. Residual field affects also the critical magnetic field, which did not deviate from the value $\mu_0 H_c = 74.6$ mT at 2 K in our measurements, thus we can neglect this effect.

Most of our samples had rectangular, plate-like shape, with the *c*-axis perpendicular to the plate. Therefore the measurements in magnetic fields applied parallel to the *c*-axis were significantly influenced by the effect of demagnetizing factor. However, the effect of demagnetizing field is negligible considering the relation $\boldsymbol{H_D} = n\boldsymbol{M}$ for small values of $\boldsymbol{M}$, which is the case of antiferromagnets; the demagnetizing field is much stronger in the case of superconductors.

| Shape of the samples | Theoretical value of demagnetizing factor $n$ [2] (except rod ‖ field) | Experimental value of demagnetizing factor $n$ (this work) |
|---|---|---|
| rod ‖ field ($l/d = 10$) | 0.017 ($l/d = 10$) [144] | 0.02 ($l/d \sim 13$) |
| plate ‖ field | 0 | 0.08 |
| sphere | ⅓ | - |
| rod ⊥ field | ½ | - |
| plate ⊥ field | 1 | 0.77 |

Tab. 3: The dependence of demagnetizing factor $n$ on the shape of the samples. The theoretical values are for a long rod where $l/d = 10$ and for a plate. The experimental values are for samples of finite dimensions as described above.
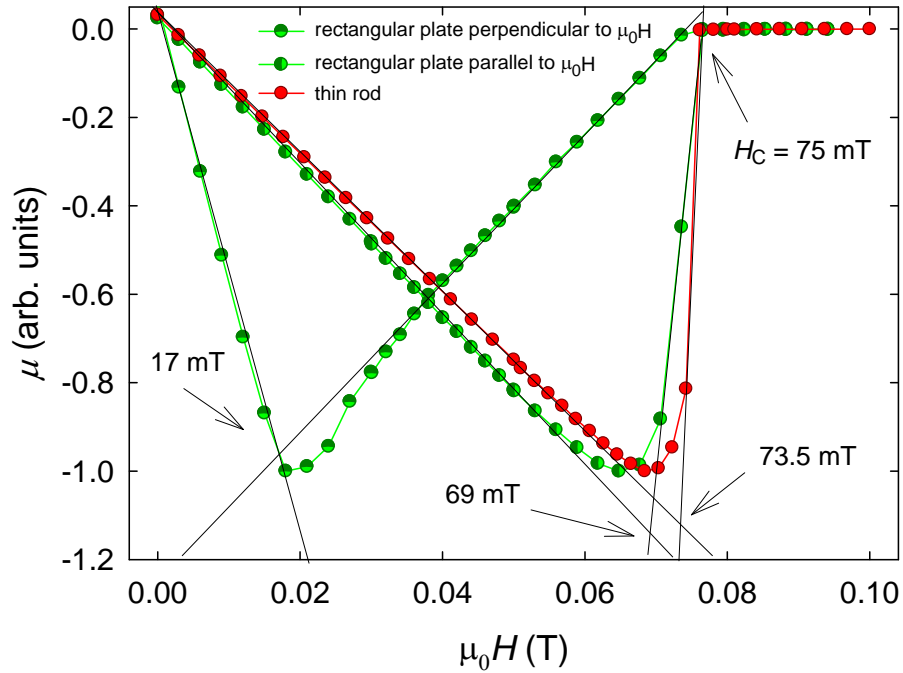
Fig. 23: Magnetization curves of lead samples of rectangular shape placed parallel and perpendicular to the external magnetic field and magnetization curves of a thin lead rod. The data are standardized on -1.

## 4.6. Specific heat measurements

The measurements of heat capacity were performed on PPMS 9T in temperature range 0.35 – 400 K using Helium-3 option devices (1.8 - 400 K without these devices). The measurements are normally performed under vacuum conditions, which imply constant pressure ($C_p$). The measurement itself proceeds under vacuum of $10^{-5}$ torr. The sample is placed on a corundum plate 3×3 mm in the sample holder - puck (see Fig. 24). To keep the sample in position and to improve the heat contact, the Apiezon – heat conductive Grease is used (Apiezon N is used for temperatures below 300 K; H is used for measurements to the highest temperatures). A thermometer and a heater are fixed to the bottom part of the plate. The sample is heated by a heat pulse and then relaxes (relaxation method). The heat capacity is determined from the time dependence of temperature during the relaxation. The specific heat of the corundum plate with Apiezon has to be measured within the calibration without the sample in order to separate later the contribution of the sample.

Fig. 24: The left upper part: modified commercial puck for vertical HC measurement with the heater and thermometer on the corundum plate, 3He puck with the sample; the right part: 3He insert with the puck for HC measurement.

Specific heat is defined as the heat $dQ$ needed to increase the temperature $T$ of a unit of mass of a substance in a unit of degree

$$C_y = \frac{\delta Q}{\delta T} \tag{39}$$

Parameter $y$ indicates the control parameters kept constant. Specific heat $C_p$ can be expressed as

$$C_p = T \left( \frac{dS}{dT} \right)_P \tag{40}$$

therefore, the experimental knowledge of $C_p(T)$ provides a direct measure of the entropy evolution of the system.

Specific heat generally consists of many contributions, which become dominant in different temperature ranges [145]:

$$C_{tot} = C_n + C_{el} + C_{ph} + C_{mag} + C_{Sch} \tag{41}$$

40

The contribution $C_n$ [145] represents nuclear contribution, which becomes important for $T < 0.5$ K. This contribution is usually recognized by $C \propto T^{-2}$ dependence and it will not be further discussed in this work.

Conduction electrons can be described as free electrons and their contribution, electronic specific heat $C_{el}$ dominates approximately in the temperature range $0.5 < T < 5$ K; more precisely, the region is defined by Debye temperature $\theta_D$ (described further) [146]. Contribution $C_{el}$ can be described using Sommerfeld model for temperatures much lower than $T_F$ where Fermi temperature $T_F$ is $10^4$ - $10^5$ K:

$$C_{el} = \frac{2nk_B^2 T}{E_F} = \gamma T \tag{42}$$

The quantity $E_F$ is energy of Fermi level, $n$ is the number of free electrons in a unit volume and $\gamma$ is Sommerfeld coefficient constant within the experimental range of temperature. Experimental values of $\gamma$ are extracted from a $C_p/T$ versus $T^2$ representation. The Sommerfeld coefficient $\gamma$ is strongly enhanced by electron-electron interactions and magnetic correlations and becomes even larger for HF materials (see Subsection 2.2.1).

The contribution $C_{ph}^2$ approves itself more significantly for high temperature region (for about $T > \theta_D/30$ where $\theta_D$ is Debye temperature) and it is caused by the lattice vibrations represented by quasiparticles - phonons. Phonons can be divided into optical ($3n$-3 branches) and acoustical (3 branches) for a unit cell with $n$ atoms (the detailed derivation can be found in Kittel [2]. The contribution $C_{ph}$ is extracted from the slope of a $C \propto T^2$ because of the formula

$$\frac{C_P}{T} = \gamma + \beta T^2 \tag{43}$$

where $\beta$ is relied to phonon contribution. The high temperature region can be described using Dulong-Petit law $C_{ph} \rightarrow 3Nk_B$ where $3N$ are 3 degrees of freedom of $N$ atoms. This leads to almost constant value of phonon specific heat, which is independent on any material. The law becomes invalid for lower temperatures where $C_{ph}$ decreases to zero. As a reaction on the limitations of Dulong-Petit law, two models taking quantum physics into account - Einstein and Debye model - were developed to explain the low-temperature behavior of specific heat.

Einstein model expect that the lattice vibrations can be described as independent vibrations of $N$ harmonic oscillators with equal frequency. Then, the heat capacity can be given by

$$C_{phE} = 3Nk_B \left(\frac{\theta_E}{T}\right)^2 \frac{e^{\frac{\theta_E}{T}}}{\left(1 - e^{\frac{\theta_E}{T}}\right)^2} \tag{44}$$

where $\theta_E$ is Einstein temperature characterizing one branch of frequency $v_E$.

The frequency $v_E$ is defined as

$$\theta_E = \frac{h v_E}{k_B} \tag{45}$$

41

This model describes the high-temperature region and optical phonons very well but it fails when applied for temperatures lower than ~ 0.2 $\theta_E$.

To describe the low-temperature region and the acoustic braches properly, the Debye model is presumed. It deals with the material as a continuous elastic body, which vibrates elastically in analogy with sound vibrations. The frequencies are proportional to *ck* where *c* is the speed of propagation of vibration waves and *k* is the size of wave vector. The specific heat is given by

$$C_{phD} = 9Nk_B \left(\frac{T}{\theta_D}\right)^3 \int_0^{\frac{\theta_D}{T}} \frac{x^4 e^x}{(e^x-1)^2} dx \ . \tag{46}$$

The quantity $\theta_D$ is Debye temperature characterizing one branch, defined as

$$\theta_D \sim \frac{h\nu_D}{k_B} \tag{47}$$

where $\nu_D$ is the highest possible frequency. Using both models, one can describe both low- and high – temperature region satisfactory. To describe the specific heat more precisely, it is necessary to leave the harmonic approximation and to consider thermal expansion. Anharmonicity is given by the correction factor

$$\frac{1}{1 - \alpha T} \tag{48}$$

where $\alpha$ is a correction coefficient, which represents a very small perturbation compared to perturbation due to thermal expansion. This effect leads to the corrected form of specific heat contribution

$$C_{ph} = R \left( \frac{1}{1 - \alpha_D T} C_D + \sum_{i=1}^{3N-3} \frac{1}{1 - \alpha_E T} C_E \right) \tag{49}$$

Specific heat contributions $C_D$ and $C_E$ are in harmonic approximation along the Debye and Einstein theory, respectively. According to the last equation, there are $3n$- 3 + $3n$ - 3 + 2 = $6n$ - 4 free variables in total. This approximation would lead to very unstable system of many parameters making any fitting impossible. The degeneration of branches, which is given by the crystal symmetry, reduces the number of variables.

The description of the magnetic contribution $C_{mag}$ is much easier for temperatures above the specific ordering temperature and it is connected with the crystal field effect [3]. The splitting caused by CF (see Section 2.1) corresponds to the contribution of the specific heat, which is called Schottky anomaly. The specific heat $C_{mag}$ of a material in paramagnetic state is given by the Schottky contribution $C_{Sch}$ [147]:

$$C_{Sch} = \frac{R}{T^2} \left( \frac{\sum_{i=0}^{n} \Delta_i^2 exp\left[-\frac{\Delta_i}{T}\right]}{\sum_{i=0}^{n} exp\left[-\frac{\Delta_i}{T}\right]} - \left( \frac{\sum_{i=0}^{n} \Delta_i exp\left[-\frac{\Delta_i}{T}\right]}{\sum_{i=0}^{n} exp\left[-\frac{\Delta_i}{T}\right]} \right)^2 \right) \tag{50}$$

where $\Delta_i$ is the energy of the $i$-th energy level. The contribution to magnetic entropy can be described in high-temperature limit as

$$S_{mag} = Rln(2J + 1) \tag{51}$$

The crystal field ground state of most cerium compounds is a doublet, which leads to the maximum theoretical value of entropy connected with magnetic phase transition equal to (see Subsection 2.2.2)

$$\Delta S = Rln2 \tag{52}$$

Schottky anomalies are well observed when their respective characteristic energies or associated gaps, $\Delta$, are about $k_B\Delta < 20$ K [145], but it is also possible to observe levels with higher energies, especially those with high Debye temperatures [146].

Specific heat data can be used to estimate the evolution of Kondo temperature $T_K$. There are several methods of estimating $T_K$; in this work, the evaluation of $T_K$ based on a simple two-level model was used [148], according to Čermák et al. [149,150]. In this model, the magnetic entropy $S$ is reduced from the value of $R$ ln2 (for more details see Section 4.6) by an energy splitting of $k_B T_K$ at Curie temperature $T_C$:

$$\frac{\Delta S}{R} = \ln\left[1 + \exp\left(-\frac{T_K}{T_C}\right)\right] + \frac{T_K}{T_C}\left[\frac{\exp(-T_K/T_C)}{1 + \exp(-T_K/T_C)}\right] \tag{53}$$

Various methods of estimating $T_K$ (based on measurements of dilute impurities in an appropriate non-magnetic host material – quasi-elastic neutron scattering, estimating from the magnetic susceptibility, resistivity measurements) give different results compared to each other, but similar general trends in the evolution of $T_K$ across the series are observed. This may be due to different time scales of the experimental techniques [151]. Considering this fact, we do not propose any precise estimating of $T_K$, but we present its clear evolution for the prepared substitutions.

## 4.7. Resistivity measurements

The electrical resistivity was measured as a function of temperature and magnetic field using a standard four-probe AC method on PPMS 9T. The measured temperature range was extended from 0.35 to 300 K using 3He insert.

The sample holders enable to measure two oblong samples simultaneously by using two independent channels. Couples of current and voltage contacts were prepared from cooper

wires fixed to the sample by a conductive silver paste. The measurement in the low-temperature region requires properly prepared contacts with electrical resistivity between contacts lower than approx. 5 Ω. The appropriate excitation current, frequency and time have to be set up accordingly to the measured temperature range to get a sufficient signal. To prevent the overheating of the sample in the low-temperature region, the excitation current was ~ 0.2 mA; for higher temperatures, the excitation current from 0.5 to 5 mA was used.

## 4.8. Pressure measurements

Static pressures $p$ up to 2.4 GPa were generated using a hybrid two-layered Cu-Be/NiCrAl clamped pressure cell [152] with highest nominal pressure of 3 GPa, which is designed to fit into PPMS 9T. However, considering the ageing caused by frequency of previous experiments, we avoided exceeding 2.5 GPa. The interior diameter of the cell is 4 mm; the resulting specimen diameter restricted by a Teflon cap is 2.7 mm. The Daphne oil 7373, which belongs to olefin oligomers, was used as the pressure-transmitting medium. The manganin wire (manganin is an alloy of typically 86 % Cu, 12 % Mn, and 2 % Ni) was used to determine the pressure inside the cell according to its strong pressure dependent resistivity:

$$R(T,p) = R(T,0)(1 + \alpha(T)p) \tag{54}$$

where $\alpha(T)$ is the pressure coefficient of resistance of the manganin. Its value at room temperature (at which the changes of pressure were realized) is $\alpha(293 \text{ K}) = 2.465 \cdot 10^{-3}$. Arrangement of two 4-wire resistivity outputs (sample and manganin) were covered by the Daphne oil and placed into the Teflon capsule. CuBe-anti-extrusion rings seal the Teflon container. The electrical contacts between the sample and manganin inside pressurized space and the measurement electronics were mediated by insulated Cu-wires leading out of the cell through the plug [47].

In the case of the tested pressure-transmitting media, the values of $\beta_m/\kappa_m$ are close to value $10^{-3}$ GPa/K, see Fig. 25. The difference $\Delta p$ between the room- and the lowest measured temperature of the Daphne 7373 oil inside the used pressure cell is $\Delta p \sim 0.3$ GPa and remains similar all over the used range of pressures.
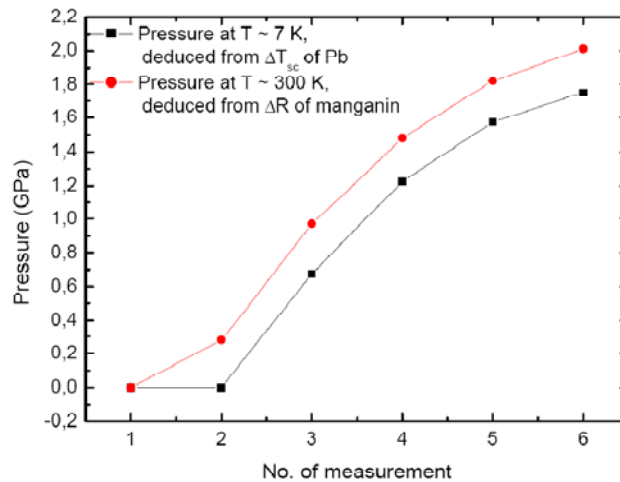


Fig. 25: The calibration of the pressure difference between the room temperature and the temperature ~ 7 K (temperature of superconducting transition of lead), according to Ref. [153]. The test was performed directly in the same pressure cell as our experiment.

44

The real values of pressure in the low temperature region inside our cell were determined using the linear pressure dependence of the electrical resistivity of manganin at room temperature (according to equation (54)) and the above-mentioned difference $\Delta p$ between low- and room temperature. The maximum deviation from linearity of the pressure dependence does not exceed 1 % of the whole pressure changes of the resistance. The resistance of manganin reveals relatively large temperature dependence at low temperatures. However, it is almost temperature independent within the temperature range ~ 10 K near the room temperature, which allows neglecting the temperature changes of the manganin resistance while applying the pressure in the cell at room temperature.

# 4.9.    Computational methods

In this section, the basic computational methods are explained in order to enable their usage in forthcoming chapters. First-principles methods use quantum-mechanical descriptions of atoms to calculate materials properties. They provide very detailed information about electronic structure of system studied [25]. The method used in this work is density functional theory (DFT) within local spin density approximation (LSDA) and the generalized gradient approximation (GGA). For this purpose, the full potential augmented plane wave plus local orbitals method (APW+lo) was used (for more details of the codes and parameters see Pospíšil *et al.* [154]) to solve the single particle Kohn-Sham equations.

DFT [25] represents a quantum mechanical method which describes the ground state of a many-body system, but instead of working with a system of $N$ electrons it uses the functionals of spatially dependent electron density with 3 coordinates. Standard DFT is based on solution of Kohn-Sham equations [23] which describe electrons in an effective single particle potential. Kohn-Sham potential includes also the exchange-correlation term. However, exact functionals and corresponding exchange-correlation potential are not known, except for the electron gas, which presents the crucial problem of DFT. The most widely used approximation of DFT is the local-density approximation (LDA) [25]; the functional depends only on the density at the coordinate where the functional is evaluated. LSDA [25,155] is based on the similar principle as LDA and in addition, it includes electron spin. In comparison with LSDA, GGA [156,157] represents a numerical approximation which takes into account also the gradient of the density at the same coordinate and improves, for example, the total energies and lattice parameters of $3d$ [157] and $4d$ metals [156]. The APW method represents a numerical method to solve Kohn-Sham equations not only close to nucleus but also in the interstitial region. The space of unit cell is divided into spheres centered in each atom site, and into the interstitial region. The local orbitals (lo) improve the APW basis.

# 5. Results and discussion

## 5.1. YPd$_2$Al$_3$

### 5.1.1. Synthesis and characterization

The polycrystalline sample of YPd$_2$Al$_3$ was prepared by melting of the stoichiometric amounts of pure elements (purity of Y - 99.9 %, Pd - 99.95 %, Al - 99.9999 %) in an arc-furnace under high-purity (99.9999 %) argon atmosphere. The sample was re-melted several times to achieve good homogeneity. The stoichiometry of the sample was kept stable due to a negligible evaporation during melting. After that, a part of the sample was wrapped in tantalum foil, sealed in a quartz ampoule under high vacuum of $10^{-6}$ mbar and annealed at 700 ºC for 14 days, then slowly cooled down to room temperature to avoid any possible stresses in the material.

The final composition was checked by microprobe analysis. Except the major phase of YPd$_2$Al$_3$, phases of Y$_2$O$_3$ and a nonstoichiometric compound similar to YPd$_6$Al$_3$ were detected (see Fig. 26). BSE detector enabled to emphasize the contrast among different phases. The impurity phases accumulated especially by the grain boundaries and their distribution in the sample was homogenous, thus we have not observed any concentration gradient.
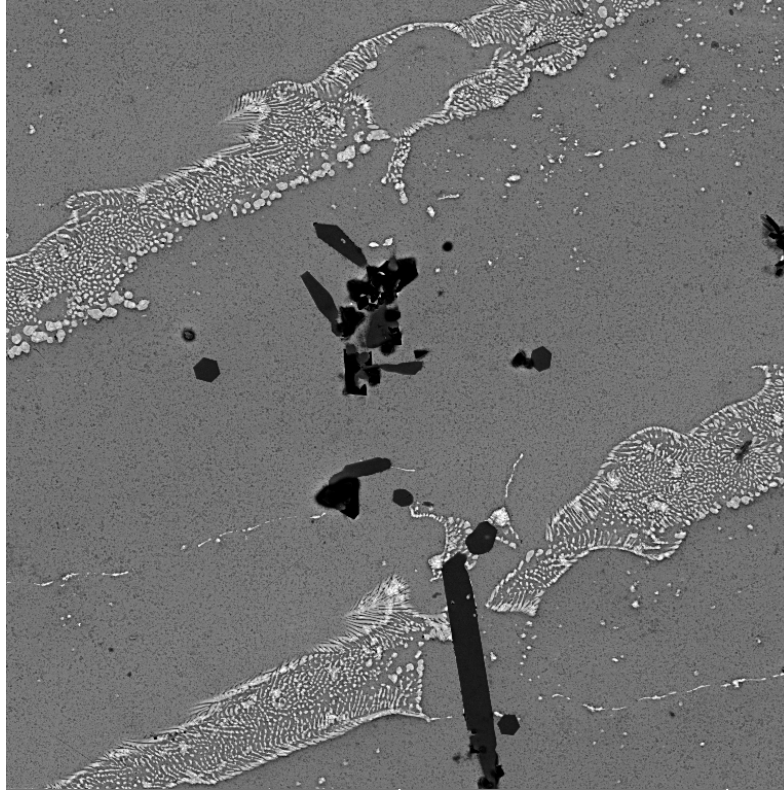
Fig. 26: BSE image of polished surface of the annealed sample from SEM - the white grains formed to stripes are the phase of $YPd_6Al_3$; the square black grains are $Y_2O_3$.

X-ray powder diffraction patterns of both, as-cast and annealed samples were recorded by crushing the sample into powder. The sample was found to have the hexagonal P6/mmm structure and adopts the $PrNi_2Al_3$-type structure, which is an ordered variant of the $CaCu_5$ type. We observed several diffraction lines which did not belong to the major phase and pointed to the presence of small amounts of impurity phases. These reflections were slightly suppressed by the annealed sample. Multiphase composition was checked later by EDX analysis. The difference between lattice parameters of as-cast and annealed samples determined at room temperature are negligible: $a = 5.3720 \pm 0.001$ Å, $c = 4.193 \pm 0.002$ Å (as-cast sample) $a = 5.3704 \pm 0.0006$ Å, $c = 4.1932 \pm 0.0007$ Å (annealed sample) are close to values for $GdPd_2Al_3$ and $UPd_2Al_3$ as can be seen in Tab. 1.

## 5.1.2. Physical properties and computational results

The resistivity was measured on as-cast and annealed sample, respectively and revealed a superconducting transition, as shown in Fig. 27. The transition temperature $T_s = 2.2$ K of the annealed sample is strongly enhanced compared to the $T_s = 0.6$ K of the as-cast sample. The significant difference can be caused by the imperfect occupancy of the atoms in the crystal lattice and material stress after melting. The transition temperature was determined from the maximum of the temperature derivative of resistivity curve.
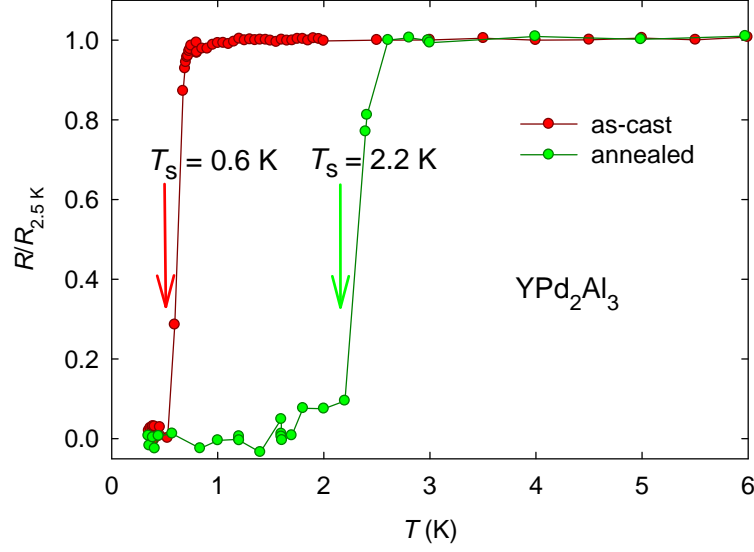
Fig. 27: Resistivity measurement of the as-cast and annealed sample of $YPd_2Al_3$.

The magnetoresistance measurement shown in Fig. 28 revealed shift of $T_s$ with increasing temperature, typical for superconducting transition.
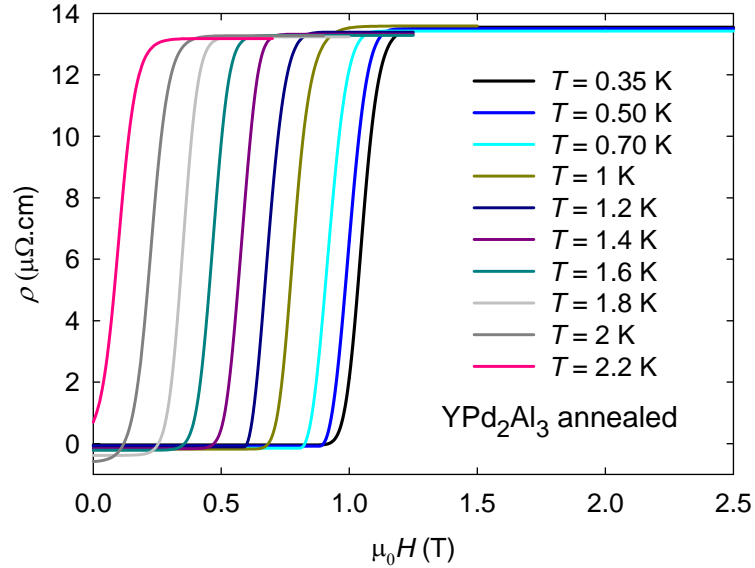


Fig. 28: Magnetoresistance curves of $YPd_2Al_3$ in various temperatures.

The critical fields at various temperatures were determined as the maxima from the field derivative of magnetoresistance curves. We have calculated the value of critical field $\mu_0H_{C2}(0)$ from the square law using equation (31) and we have found the value $\mu_0H_{C2}(0) = 1.25$ T. The Nevertheless we have found that the square law is not suitable model for our resistivity data. The value of critical field $\mu_0H_{C2}(0) = 0.96$ T, determined from WHH formula (32) [55], is closer to the value from square law applied on AC susceptibility data, as it is shown below. We have estimated the superconducting coherence length $\xi(0) = 192$ Å based on Ginzberg-Landau formula (33) for an isotropic three-dimensional superconductor.
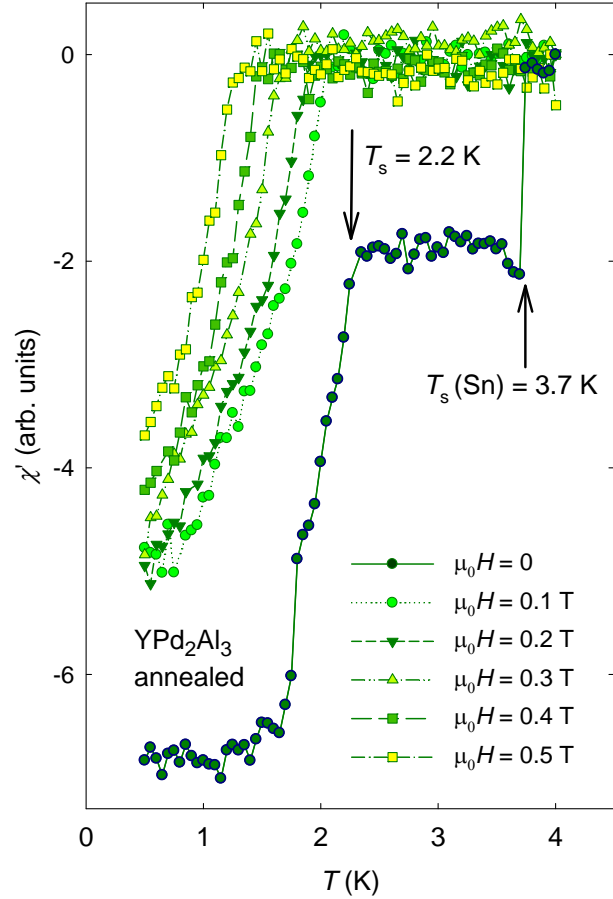
Fig. 29: The temperature evolution of the real part of AC susceptibility $\chi'$ in various magnetic fields; the arrow on the left marks the steps on curves where the YPd$_2$Al$_3$ sample becomes superconducting, the arrow on the right marks the sharp transition of tin to the superconducting state.

The deviation of $\mu_0 H_{C2}(T)$ given by the resistivity data from the square law was an impulse to investigate superconductivity using AC susceptibility. The measurement of AC susceptibility presented in Fig. 29 was performed on the same annealed sample as the previous resistivity measurement. The home-made AC magnetometer was used to estimate the temperature of the macroscopic transition into the superconducting state. The comparable piece of tin used as a standard can be identified in the data by a transition at 3.7 K, which is suppressed completely in higher magnetic fields. The transition of tin is sharp when compared to the broaden transition of YPd$_2$Al$_3$ compound in the temperature range 1.7 - 2.2 K. This difference can be induced by mechanical stress inside the sample and small composition inhomogeneities. Considering fact, that we are only able to compare the relative value change of the AC susceptibility between the standard (tin) and the sample in case of our home-made magnetometer, we have no possibility to measure the susceptibility properly to obtain value of the Meissner fraction [‡] as discussed in Nagano *et al.* [158]. We suppose that majority part of the sample was in the SC state. We have also determined the value of the critical field

---

[‡] The Meissner fraction expresses the ratio of field cooled to zero field cooled magnetization. The Meissner fraction tends to underestimate the real superconducting volume fraction of the specimen when measured in magnetic fields ~ 0.1 T.

$\mu_0 H_{C2}(0) = 0.825$ T from AC data, which is lower than the corresponding result from resistivity data.

The temperature of superconducting transition was confirmed by the AC susceptibility measurement using SQUID magnetometer, as well, as can be seen in Fig. 30:
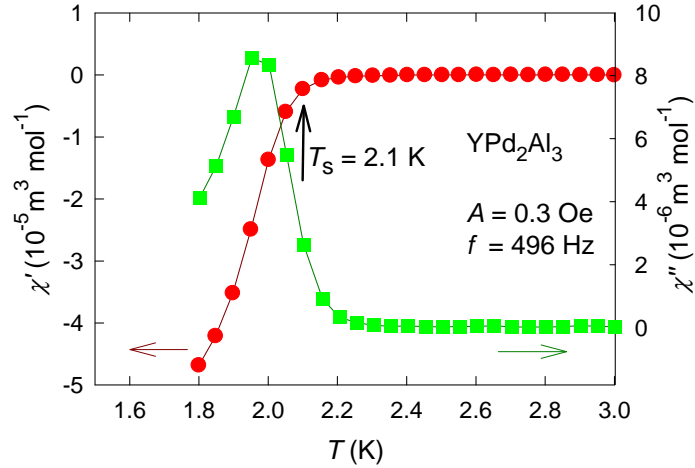


Fig. 30: Temperature dependence of real and imaginary part of AC susceptibility. The black arrow marks the onset of superconductivity in the curve of real part of AC susceptibility. The other arrows tie the curves together with the right axes.

The onset of superconductivity in the real part of AC susceptibility at 2.1 K corresponds to the result from the home-made AC magnetometer. The maximum of the imaginary part can be seen slightly below 2 K.

The values of critical field obtained from different experiments are summarized in Fig. 31. The circles represent results of AC susceptibility measurements, the squares represent results of resistivity and the dotted curve marks the square law fit for AC susceptibility data. The significant deviation of the resistivity data from the square law is clearly observable as was discussed earlier whereas the AC measurement provides significantly better results and the square law presents a very good approximation.
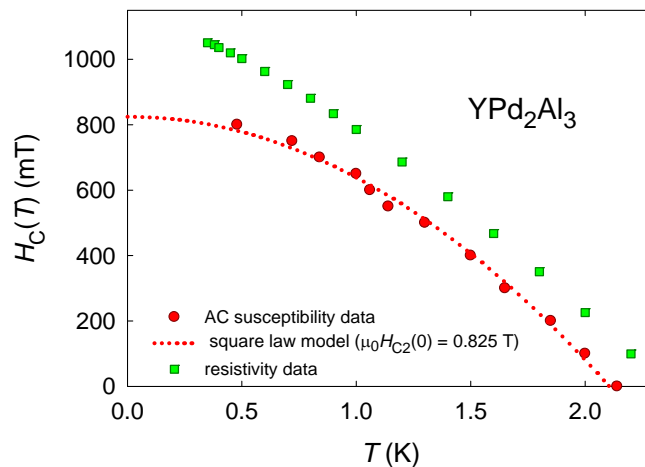


Fig. 31: Temperature dependence of critical magnetic field obtained from magnetoresistivity curves and AC susceptibility.

50

The specific heat measurement presented in Fig. 32 confirmed the superconducting transition observed in resistivity measurements, although the anomaly is almost negligible (see inset in Fig. 32). The fit of specific heat data was performed using Debye and Einstein model (see equation (49)) with respect to the anharmonicity. The parameters characterizing the phonon spectrum (the degeneracies of Debye and Einstein branches, the Debye and Einstein temperatures and corresponding anharmonicity), summarized in Tab. 4, resemble those of lanthanide analogs [73]. The Sommerfeld coefficient $\gamma = 7.2$ mJ mol$^{-1}$ K$^{-2}$ was obtained from the linear fit of $C/T$ vs $T^2$ data using equation (43). Its value points to relatively low density of states at Fermi level. We used $\Delta C_p$, shown in the inset of Fig. 32, to estimate the ratio $(\Delta C_p)_{T_S}/\gamma T_s$, which is equal to 1.43 considering the BCS weak-coupling theory (see Section 2.3). However, a significantly lower value ~ 0.2 was determined by our measurement. We assume that the transition to superconducting state does not happen at any particular temperature, but it is broadened into some certain temperature range due to mechanical stress within the sample. This broadening was observed also in the AC susceptibility data.
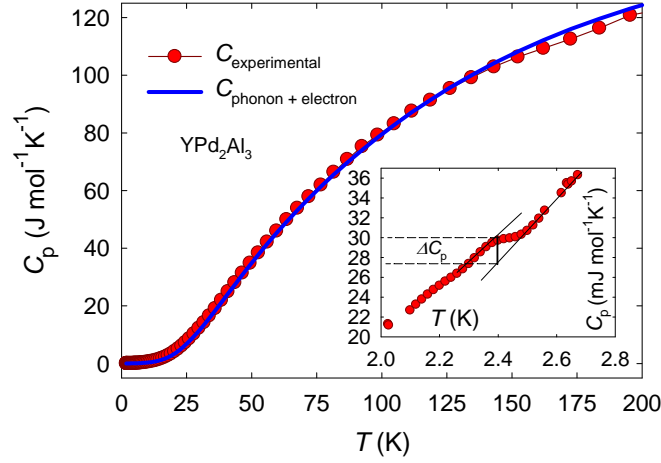


Fig. 32: The temperature dependence of specific heat. The blue line represents the fit based on Debye and Einstein model. The inset shows the low temperature region with the superconducting transition.

| Branches | Degeneracy | $\theta$ (K) | $\alpha$ ($10^{-4}$ K$^{-1}$) |
|---|---|---|---|
| $\theta_D$ | - | 200 | 1 |
| $\theta_E$ | 3 | 380 | 2 |
| $\theta_E$ | 5 | 211 | 1 |
| $\theta_E$ | 2 | 130 | 2 |
| $\theta_E$ | 5 | 550 | 2 |

Tab. 4: The phonon spectrum of YPd$_2$Al$_3$ based on Debye and Einstein model.

The experimental magnetic susceptibility in the normal state is temperature independent and reaches the value $\chi_{exp} \sim 2 \times 10^{-8}$ m$^3$ mol$^{-1}$. The somewhat higher theoretical value $\chi_{theor} \sim 7.7 \times 10^{-8}$ m$^3$ mol$^{-1}$, calculated by using equation for Pauli susceptibility (20), provides only right order with the experimental value. The overestimation of theoretical value can be

related to the approximate exchange correlation functional used in our first principles DFT calculations.

In Fig. 33 (*a*) the total density of electronic states of $YPd_2Al_3$ based on GGA calculations at experimental equilibrium is presented [154], while in Fig. 33 (*b*) - (*d*) the DOS of individual elements is shown. The width of the occupied part of DOS is 9.5 eV. It can be divided into two parts – the first part from -9.5 to -4.8 eV originates mostly from free-electron-like states and from the Y 5*s*, Pd 5*s*, Al 3*s* and Al 3*p* states from the atomic spheres [154]; the second part from -4.8 eV to the Fermi level represents mainly the Pd 4*d* states hybridizing with the Y 4*d* and Al 3*p* states. The unoccupied states above the Fermi level are affected mainly by Y 4*d* electrons with an admixture of the Pd 4*d* and Al 3*p* states and the large contribution from the free-electron-like interstitial region (see Fig. 33 (*d*)).

The total DOS at Fermi level reaches 2.56 states/eV and the orbital analysis revealed that mainly the Pd 4*d*, Y 4*d* and Al 3*p* states contribute to it. The value of total DOS at Fermi level is too low to induce a spontaneous magnetic polarization of Pd 4*d* states and it corresponds to Sommerfeld coefficient $\gamma_{band} = 6.0$ mJ mol$^{-1}$ K$^{-2}$. This value is somewhat lower than the value $\gamma_{exp} = 7.2$ mJ mol$^{-1}$ K$^{-2}$ obtained from specific heat measurement, which leads to a relatively low value of mass-enhancement coefficient $\lambda = 0.19$ from

$$\gamma_{exp} = (1 + \lambda)\gamma_{band} \tag{55}$$

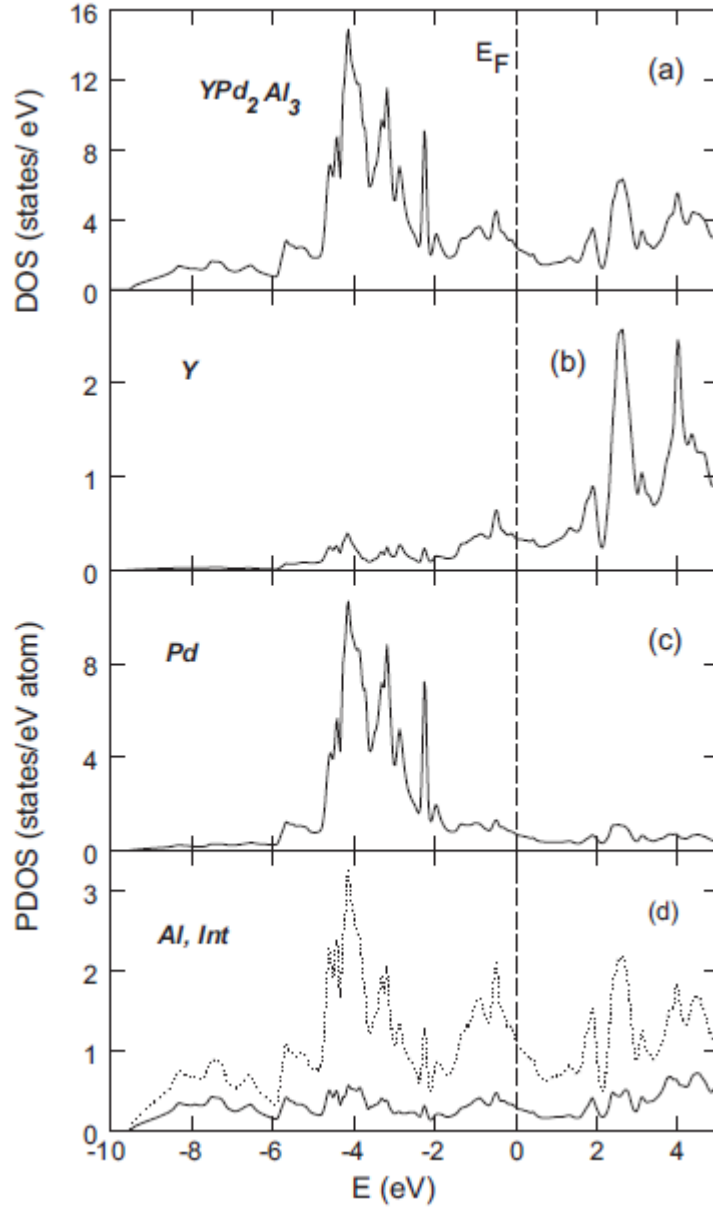pointing to a weak electron-phonon interaction in the $YPd_2Al_3$ compound.

Fig. 33: The DOS (*a*) and atom-projected DOS (*b*) - (*d*) of YPd$_2$Al$_3$ compound. The interstitial region marked by a dotted line together with Al DOS marked by solid line is shown in (*d*) part. Fermi level is marked by a dashed line at zero energy.

In order to compare the experimentally obtained value of $T_s$ with a value calculated theoretically we used the McMillan formula [159], the first presented superconducting temperature relation based on Eliashberg equations. The formula is based on the minimum set of three parameters – Debye temperature $\theta_D$, mass-enhancement coefficient $\lambda$ and Coulomb pseudopotential $\mu^*$:

$$T_S = \frac{\theta_D}{1.45} exp\left(-\frac{1.04(1+\lambda)}{\lambda - \mu^*(1+0.62)}\right) \tag{56}$$

Using values $\theta_D = 200$ K (specific heat measurement), $\lambda = 0.19$ and $\mu^* = 0.13$ we obtained the value of $T_s$ lower than 1 mK. The value of Coulomb pseudopotential was suggested by McMillan for all transition metals and their compounds [159]. The

mass-enhancement coefficient was obtained combining experimental data from specific heat and calculations based on DFT and already this parameter influenced the result strongly (for instance the change of the value $\lambda = 0.6$ gives $T_s \sim 1$ K). The reason for such a significant difference between experimental $T_s$ and the value calculated using McMillan formula might lie in a complex nature of the phonon spectra of YPd$_2$Al$_3$. The coupling of electrons to special phonon modes can cause the unexpectedly high value of $T_s$, but this is a task for further full first-principle calculations [154].

In the calculations, two approximations were applied - GGA and LSDA, with respect to the equilibrium volume of YPd$_2$Al$_3$. Generally, GGA compared to LSDA gives both theoretical values of equilibrium volume and *c/a* ratio closer to the experimental values than LSDA method [154].

### 5.1.3. Summary

The polycrystal of YPd$_2$Al$_3$ was successfully synthetized, although two other phases Y$_2$O$_3$ and YPd$_6$Al$_3$ were detected, but their presence did not affect the further measurements due to their minor occurrence and subsequent annealing. The lattice parameters $a = 5.3704 \pm 0.0006$ Å, $c = 4.1932 \pm 0.0007$ Å of the annealed sample are close to values for GdPd$_2$Al$_3$ and UPd$_2$Al$_3$ and the unit cell is in very good agreement with the theoretical DFT value obtained using GGA [156]. Various types of measurements - magnetoresistivity, specific heat and AC susceptibility - revealed a transition to superconducting state, which was strongly enhanced after annealing to $T_s \sim 2.2$ K. The theoretical value of $T_s$ obtained from the straightforward use of McMillan formula ($T_s \ll 1$ mK) differs strongly from the well defined experimental value. This fact leads us to presumption that the observed superconductivity might result from the coupling of electrons to special phonon modes in the YPd$_2$Al$_3$ complex phonon spectra. The low value of the coefficient $\gamma = 7.2$ mJ mol$^{-1}$ K$^{-2}$ points to the low density of state at Fermi level, which was confirmed by theoretical calculations where the 4*d* states of Y ion are found 2 - 4 eV above the Fermi level. This indicates a weak electron-phonon interaction, expressed by the low mass enhancement ($\lambda = 0.19$). The parameters of YPd$_2$Al$_3$ describing mostly the superconducting properties obtained both theoretically and experimentally are presented in Tab. 5.

| Parameter | Value |
|---|---|
| $T_s$ specific heat | 2.45 K |
| $T_s$ resistivity | 2.3 K |
| $T_s$ AC susceptibility | 2.2 K |
| $T_s$ theoretical | < 0.001 K |
| $\mu_0 H_{C2}(0)$ WHH | 960 mT |
| $\mu_0 H_{C2}(0)$ square law | 825 mT |
| $\gamma$ experimental | 7.2 mJ mol$^{-1}$ K$^{-2}$ |
| $\gamma$ theoretical | 6.0 mJ mol$^{-1}$ K$^{-2}$ |
| $\xi(0)_{GL}$ | 192 Å |
| $\Delta C/\gamma T_s$ | 0.2 |
| $\theta_D$ | 200 K |
| $\lambda$ | 0.19 |

Tab. 5: The summary of parameters characterizing the superconducting and other properties of YPd$_2$Al$_3$.

# 5.2.     Ce$_n$Rh$_m$In$_{3n+2m}$

## 5.2.1. Synthesis of Ce$_n$(Rh$_{1-x}$Pd$_x$)$_m$In$_{3n+2m}$

Single crystal samples of Ce$_2$Rh$_{1-y}$Pd$_y$In$_8$ and CeRh$_{1-y}$Pd$_y$In$_5$ were grown out of indium flux using high purity elements (Ce 99.9 % + solid state electrotransport (SSE) purification [160], Rh 99.95 %, Pd 99.98+ % and In 99.9999 %). Because the amount of Ce in the melt was always below ~ 5 % the alumina crucibles could be used without a risk of attack. To optimize the quality and size of the crystals, we have performed many (~ 30) experiments using different starting compositions and growth temperature ranges. In general, the system was heated up to the maximum temperature (between 1000 °C - 950 °C) and the temperature was kept stable for several hours (~ 2 - 4) to homogenize the melt. After that, it was slowly cooled down to the temperature at which the remaining flux was centrifuged. The growth conditions for selected single crystals are summarized in Tab. 6. Temperature ranges together with typical plate-like shape and size of samples are shown in Fig. 34. Slower cooling rate in temperature range 950 - 600 °C (the green thermal process) was found to be the better for the sample homogeneity.
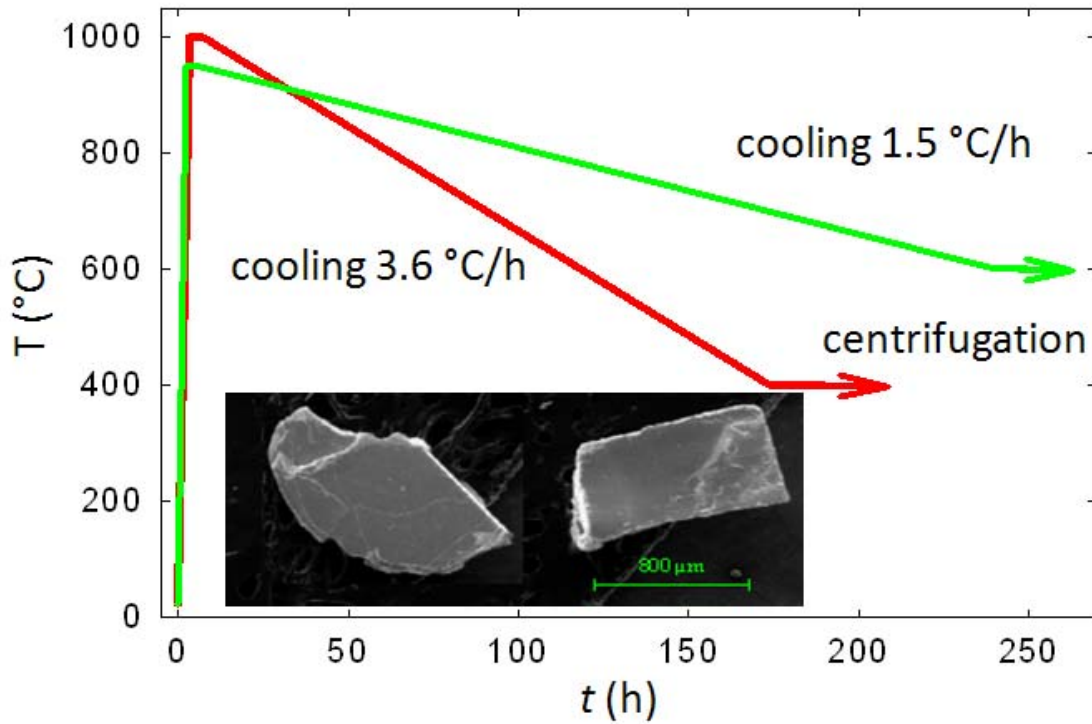
Fig. 34: Temperature vs time profile used for the $Ce_nRh_{1-y}Pd_yIn_{3n+2}$ crystal growth and the final products.

Although the growth of pure phases $CeRhIn_5$ and $Ce_2RhIn_8$ from In flux is relatively easy, the preparation of $Ce_2PdIn_8$ is much more complicated due to strong tendency of initial formation of $CeIn_3$. To avoid the growth of $CeIn_3$, several off-stoichiometric starting compositions have been suggested [21].

Another complication was the inhomogeneity of the samples, which increased with higher Pd concentration. The crystals always formed sandwich like systems consisting of many thin ($< 1$ μm) layers perpendicular to the $c$-axis with different Pd concentration. The higher was the concentration of palladium, the higher was the concentration gradient and the more frequent was the intergrowth of other phases ($CeIn_3$, $Pd_3In_7$ and $Ce_4Pd_{10}In_{21}$). Example of multiphase samples are shown in Fig. 35 (*a, b*). A multiphase sample containing $CeIn_3$ and $Ce_2Rh_{0.2}Pd_{0.8}In_8$ grown from the Pd-rich starting composition $y$ ($y \sim 99$ % Pd) illustrating the intergrowth of $CeIn_3$ is shown in Fig. 35 (*a*). In Fig. 35 (*b*), a sample grown from starting composition 1:0.7:0.3:30 is shown to illustrate the intergrowth of $CeRh_{1-x}Pd_xIn_5$ with high Pd-content into $Ce_2Rh_{1-x}Pd_xIn_8$ phase. It is obvious from the Tab. 6, that the growth of the phase 115 is not preferred for higher Pd content; instead of it, the doped phase 218 tends to grow. This is not surprising, considering the fact that the existence of the $CePdIn_5$ has not been reported yet. Starting compositions Ce:*T*:In ($T$ = Rh + Pd) 1:1:X led to growth of both 115 and 218 phases, while the ratio 2:1:X always produced 218 substitutions. Starting compositions and appropriate thermal processes of all measured samples are presented in Tab. 6.

In order to achieve higher concentration homogeneity, we have annealed the single crystals of substituted compounds at 700 °C for two weeks, however, without significant effect. According to Ref. [20], annealing of (polycrystalline) $Ce_2PdIn_8$ at 700 °C should lead to

better sample homogeneity and well defined superconductivity. We have annealed $Ce_2PdIn_8$; however the temperature of 700 °C was already too high and led to sample decomposition. Details about this treatment are presented below.

$Ce_2Rh_{1-x}Pd_xIn_8$:

| $x$ | starting composition of Ce:Rh:Pd:In | temperature range (°C) | cooling rate (°C/h) |
|---|---|---|---|
| 0 | 2:1:0:27 | 1000 - 350 | 8 |
| 0.10 | 2:0.9:0.1:30 | 1000 - 400 | 3.6 |
| 0.15 | 1:0.7:0.3:30 | 950 - 600 | 1 |
| 0.30 | 2:0.5:0.5:30 | 1000 - 400 | 3.6 |
| 0.45 | 1:0.05:0.95:40 | 950 - 600 | 1 |
| 0.85 | 1:0.01:2.99:55 | 950 - 500 | 2 |
| 1 | 1:0:3:40 | 900 - 350 | 1.7 |

$CeRh_{1-x}Pd_xIn_5$:

| $x$ | starting composition of Ce:Rh:Pd:In | temperature range (°C) | cooling rate (°C/h) |
|---|---|---|---|
| 0 | 1:1:0:25 | 950 - 700 | 1.5 |
| 0.10 | 1:0.8:0.2:30 | 1000 - 400 | 3.6 |
| 0.25 | 1:0.8:0.2:30 | 1000 - 400 | 3.6 |

Tab. 6: The growth conditions of $Ce_n(Rh_{1-x}Pd_x)In_{3n+2}$ single crystals which were selected for all the measurements presented below.



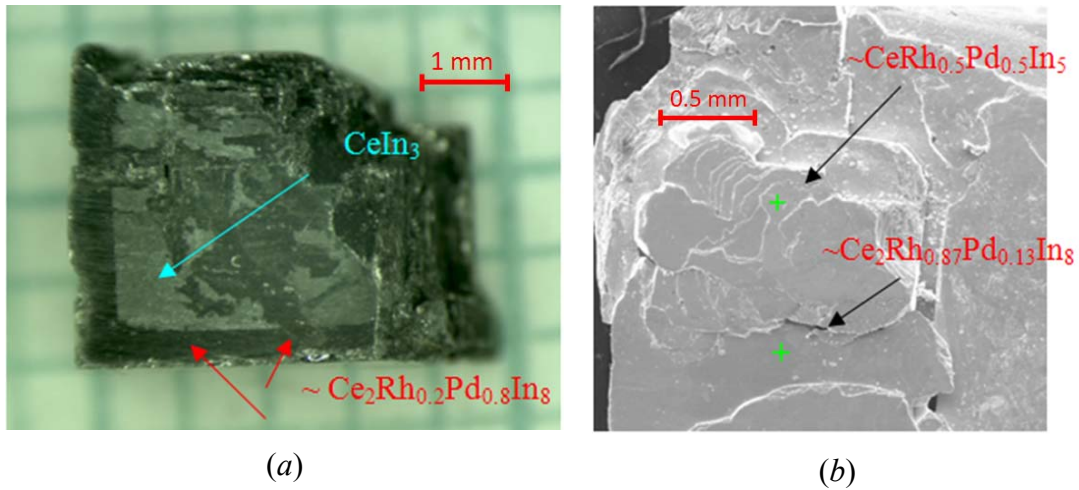Fig. 35: (*a*) An optical microscope image of a multi-phase $Ce_2Rh_{1-x}Pd_xIn_8$-$CeIn_3$ system. The contrast between the phases is given by oxidized surface of $CeIn_3$; (*b*) SEM image of a multi-phase $Ce_2Rh_{1-x}Pd_xIn_8$-$CeRh_{1-x}Pd_xIn_5$.system.

Finally, several single crystals of $Ce_2Rh_{1-y}Pd_yIn_8$ ($y$ = 0, 0.1, 0.3, 0.5, 0.6, 0.7, 0.8, 0.85, 0.9 and 0.95) were prepared. Considering the difficulties with the growth we have chosen several representative samples with best homogeneity where final composition $x \sim 0$, 0.10, 0.15, 0.30, 0.45 and 0.85. Traces of phase with the stoichiometry $CeRh_{0.5}Pd_{0.5}In_5$ and $CePdIn_5$ were detected by EDX in $Ce_2RhIn_8$ substitution, but we could not isolate these phases to either determine the structure or measure the physical properties. Due to gradual suppression

of the growth of 115 phase at the expense of 218 with increasing concentration of Pd, only samples of $CeRh_{1-x}Pd_xIn_5$ with $x \sim 0.1$ and $0.25$ were chosen for further measurements.

$Ce_4Pd_{10}In_{21}$ was found to be a by-product of $Ce_2Rh_{1-x}Pd_xIn_8$ prepared from the 1:3:55 starting stoichiometry. Since $Ce_4Pd_{10}In_{21}$, together with $CeIn_3$, also emerged as a product of decomposition of $Ce_2PdIn_8$ after annealing at 700 ˚C, we have focused on characterization of this compound more closely to disclose possible presence of this phase as an impurity in our samples. Thin needle like single crystals of $Ce_4Pd_{10}In_{21}$ are shown in Fig. 36.
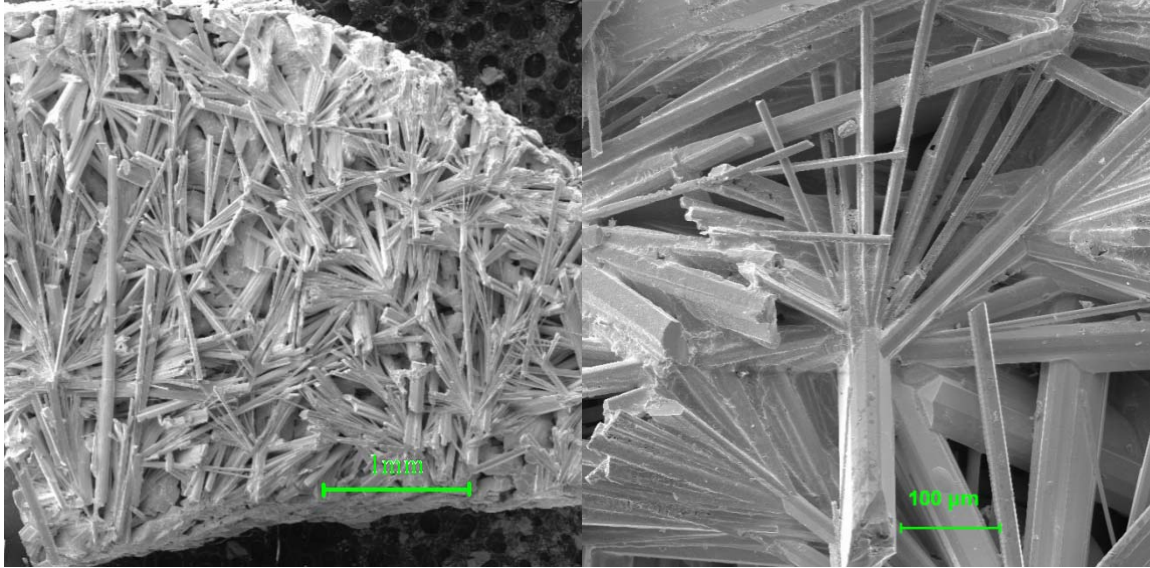


Fig. 36: SEM images of $Ce_4Pd_{10}In_{21}$ single crystals.

## 5.2.2. Characterization and physical properties of $Ce_n(Rh_{1-x}Pd_x)_mIn_{3n+2m}$

### $CeRh_{1-x}Pd_xIn_5$

The X-ray analysis of $CeRh_{1-x}Pd_xIn_5$ for $x = 0.1$ and $0.25$ confirmed the tetragonal $HoCoGa_5$ structure. The lattice parameters change only very slightly with increasing Pd content (see Tab. 7) without any particular trend.

| $x$ | $a$ (Å) | $c$ (Å) |
|------|---------|---------|
| 0 | 4.652 | 7.542 |
| 0.1 | 4.653 | 7.544 |
| 0.25 | 4.663 | 7.553 |

Tab. 7: Lattice parameters of $CeRh_{1-x}Pd_xIn_5$.

Before we start to discuss the experimental results, it is necessary to explain how we determine the Néel temperature $T_N$, SC temperature $T_s$ and magnetic field-induced transition temperature. The transition temperatures from specific heat data were determined as a point of intersection of the measured curve with the model of ideal curve of the second-order transition peak in the specific heat.

The evolution of specific heat data of $CeRh_{1-x}Pd_xIn_5$ for various concentrations $x = 0$, $0.1$ and $0.25$ in zero magnetic field is presented in Fig. 37 ($a$). The Néel temperature $T_N$ slightly

decreases with increasing Pd content from 3.78 K to 3.74 K for $x = 0$ and 0.25, respectively. On the contrary, Fig. 37 ($b$) presents evolution of magnetic phase transition of $CeRh_{0.75}Pd_{0.25}In_5$ in various magnetic fields applied along the $a$-axis. Except the AF transition in zero field, other two transitions at temperature $T_1$ and $T_2$ were observed. Using the same notation as in work of Raymond *et al.* [94], we have constructed magnetic field-temperature phase diagram for $CeRhIn_5$ and $CeRh_{0.75}Pd_{0.25}In_5$ as shown in Fig. 39. The ground state of $CeRhIn_5$ is an incommensurate helical AF with magnetic moments aligned in the basal ($a$) plane [94]. When magnetic field is applied along the $a$-axis, two magnetic-field-induced transitions are observed at temperatures $T_1$ and $T_2$ dividing the $H$-$T$ diagram to three regions (see Fig. 39). For $CeRhIn_5$ the regions I and II present incommensurate helical AF structures where region II has a larger magnetic moment on Ce atoms, while region III corresponds to commensurate magnetic structure [94].

Looking at the high magnetic-field region of the phase diagram more closely, the temperature dependencies of specific heat in magnetic fields applied along both $a$- and $c$-axes for $x = 0$, 0.1 and 0.25 are presented in Fig. 38. In case of magnetic field applied along the $c$-axis (upper figures), the Néel temperature slightly decreases while no other transition was observed. On the other hand, when magnetic field is applied along the $a$-axes (lower figures) the Néel temperatures increases, and first order-like anomalies presenting the transitions between region II and III appear. The doped samples present very similar behavior to $CeRhIn_5$ with only slight changes of the transition temperatures with increasing $x$, which shows that the magnetism of $CeRhIn_5$ is much less sensitive to Pd doping, than to the Co or Ir doping [97,98].



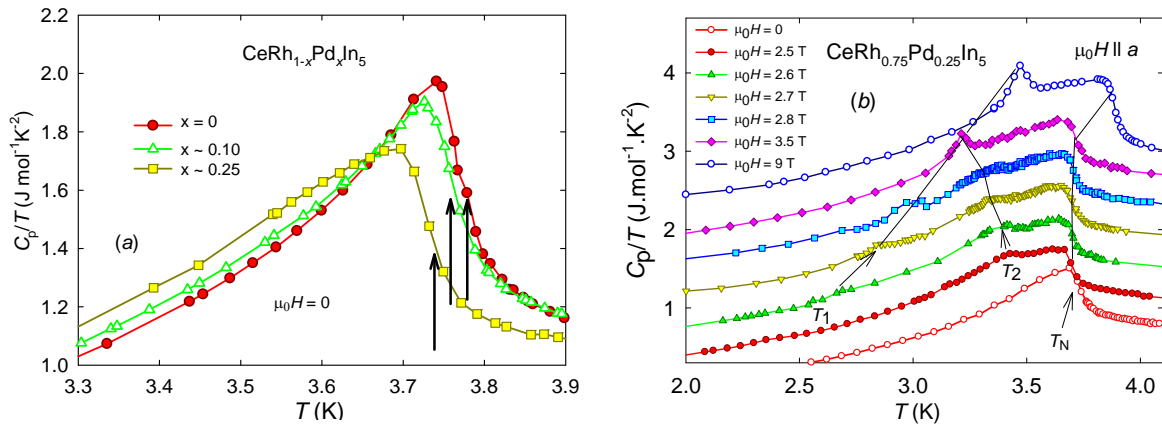Fig. 37: ($a$) - The low-temperature region of specific heat of $CeRh_{1-x}Pd_xIn_5$ ($x = 0$, 0.1 and 0.25) in zero magnetic field shows the shift of $T_N$ with increasing Pd content ($T_N$ is marked by black arrows); ($b$) - Specific heat of $CeRh_{0.75}Pd_{0.25}In_5$ measured in various magnetic fields oriented along the $a$-axis. The arrows and lines indicate the evolution of Néel temperature $T_N$ and other two transitions $T_1$ and $T_2$. The curves measured in different magnetic fields in ($b$) are shifted equidistantly for better clarity.
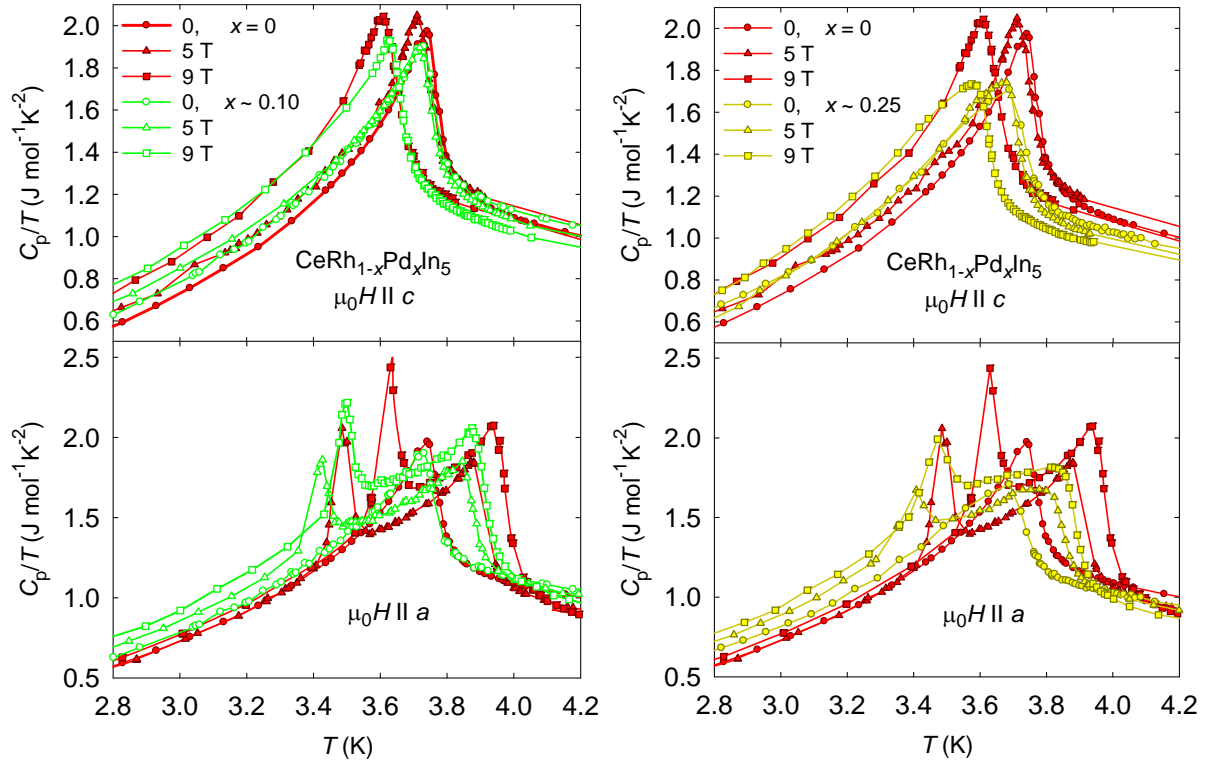
Fig. 38: The low-temperature region of heat capacity data of CeRh$_{1-x}$Pd$_x$In$_5$ in various fields applied along both crystallographic directions.



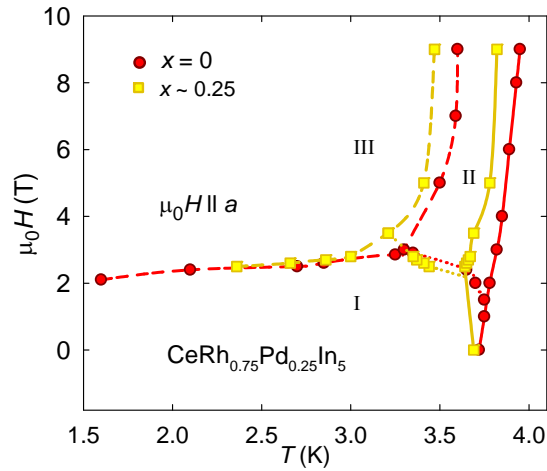Fig. 39: The *T-H* diagram of CeRhIn$_5$ and CeRh$_{0.75}$Pd$_{0.25}$In$_5$. The lines are guides to the eyes; the evolution of $T_N$, $T_1$ and $T_2$ is represented by solid, medium-medium and dashed lines, respectively. For CeRhIn$_5$, the regions marked I, II refer to incommensurate AF structure while in the region III, the AF structure is commensurate with the lattice. Same notation as in Raymond *et al.* [94] is used.

We have performed measurement of the reciprocal susceptibility ($1/\chi$) of CeRh$_{0.75}$Pd$_{0.25}$In$_5$ in magnetic field oriented along the *a*- and *c*-axis, as shown in Fig. 40.
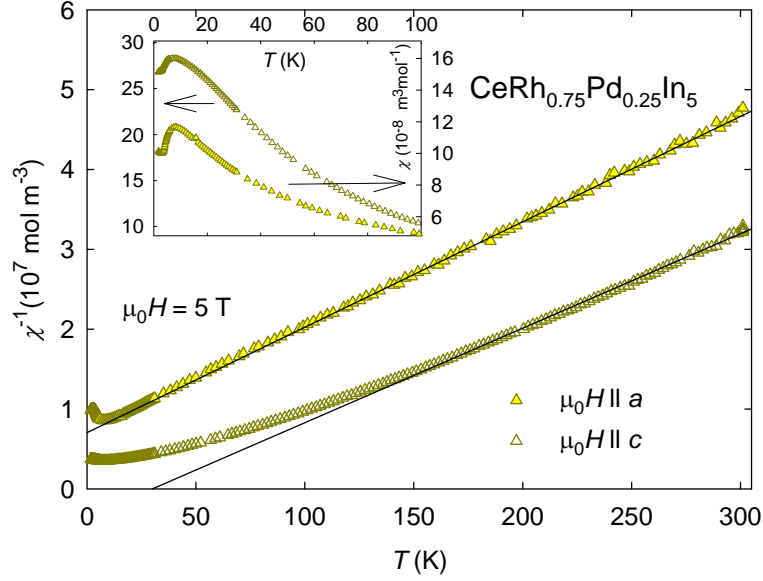
Fig. 40: Temperature dependence of reciprocal magnetic susceptibility of $CeRh_{0.75}Pd_{0.25}In_5$ measured in magnetic field 5 T oriented along both crystallographic directions (black lines are the fits of C-W law). The inset shows the low temperature region of magnetic susceptibility.

The C-W law was used to fit magnetic susceptibilities measured in magnetic field applied along the $a$- and $c$-axis. The Pd doping leads to the increase of C-W temperature for both crystallographic directions and to the decrease of the effective magnetic moment (see Tab. 8), compared to data presented by Hegger et al. [79] (the effective moment of $CeRhIn_5$ is a polycrystalline average).

| $x$ | temperature range of CW fit (K) | | $\theta_P$ (K) | | $\mu_{eff}$ ($\mu_B/Ce^{3+}$) | |
|---|---|---|---|---|---|---|
| | ll $a$ | ll $c$ | ll $a$ | ll $c$ | ll $a$ | ll $c$ |
| 0 | 100 - 300 | 100 - 300 | -79 | 16 | 2.38 | 2.38 |
| 0.25 | 15 - 300 | 150 - 300 | -55 | 30 | 2.2 | 2.3 |

Tab. 8: The concentration dependence of the paramagnetic Curie temperature $\theta_P$ and the effective magnetic moment $\mu_{eff}$ of $CeRh_{1-x}Pd_xIn_5$ together with the temperature ranges used for C-W fitting. The results for $x = 0$ are from Ref. [79].

The large difference in $\theta_P$ for both directions shows on strong crystal field splitting, however, it is slightly larger for $CeRhIn_5$. The effective magnetic moment is somewhat reduced from the value expected for a free $Ce^{3+}$ ion (2.54 $\mu_B/Ce^{3+}$) given by crystal-field splitting of the $J = 5/2$ multiplet. The reduction of $\mu_{eff}$ cannot be explained only by the weak signal or inaccuracy of the sample's mass, which could change the value of $\mu_{eff}$ in the range of less than $\sim 7\%$. As in the case of undoped phase [79], the susceptibility exhibits a low-temperature maximum at $\sim 8$ K for both directions, similar to the undoped phase [79], which is commonly ascribed to the presence of rare earth impurities [162].

The magnetization measured along the $a$-axis in contrast to magnetization along the $c$-axis (see Fig. 41) shows a significant abrupt decrease of magnetization for $\mu_0H = 3$ T at $\sim 3.4$ K which is in agreement with the heat capacity data where a magnetic field-induced transition is observed at similar conditions. This leads us to conclusion that this effect which disappears in magnetic fields higher than 3 T corresponds most likely to the second order

61

field-induced transition at $T_2$. The transition at $T_1$ was not observed in the magnetization measurement and the AF transition at $T_N$ is hardly observable. The values of transition temperatures $T_N$ and $T_2$ are determined from Fig. 41 (marked by black arrows).
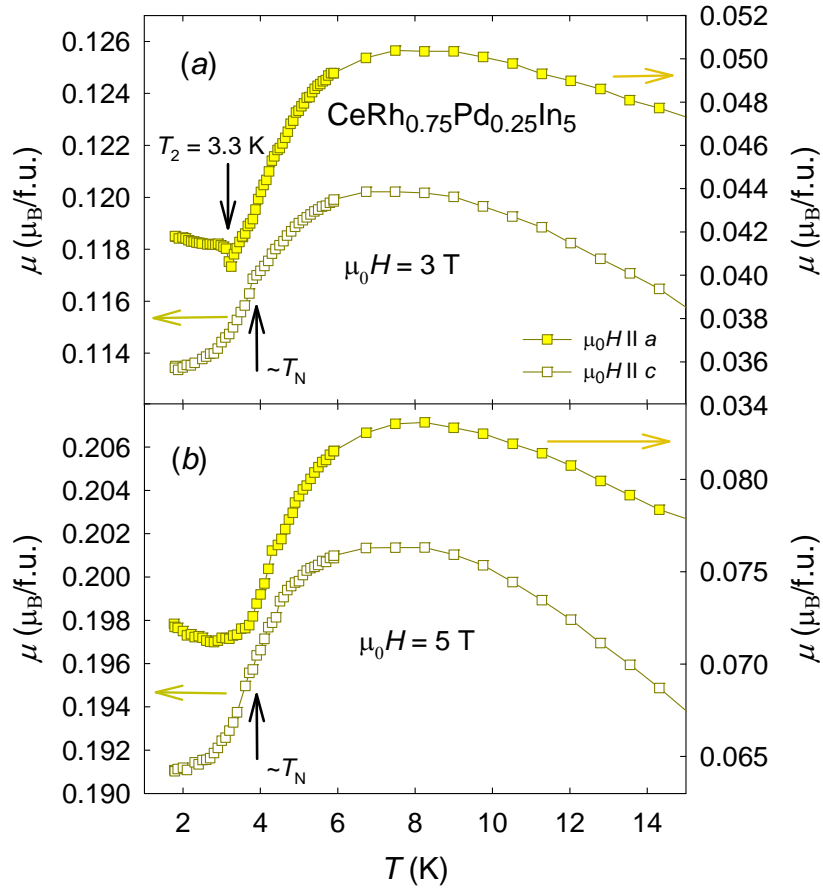


Fig. 41: Temperature dependence of magnetization of $CeRh_{0.75}Pd_{0.25}In_5$ measured in magnetic fields of 3 T (*a*) and 5 T (*b*), respectively, applied along both crystallographic directions. The black arrows point to transitions $T_2$ and $T_N$, respectively. The other arrows tie the curves together with the right axes.

The comparison of heat capacity and magnetization measurement is presented in Fig. 42. The temperature $T_2$ where the anomaly on magnetization curve is observed is consistent with the temperature of the second-order magnetic field-induced transition in the heat capacity data, both measured for $\mu_0 H = 3$ T.
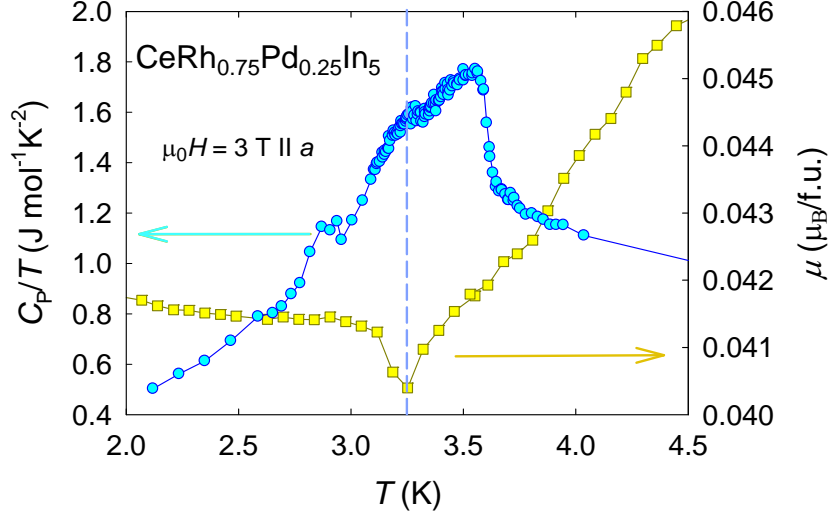
Fig. 42: Temperature dependence of magnetization and heat capacity of $CeRh_{0.75}Pd_{0.25}In_5$ in magnetic field of 3 T applied along *a*-direction. The blue dashed line marks the corresponding position of transition $T_2$ observed in both experiments. The arrows tie the curves together with the right axes.

We have also investigated the effect of hydrostatic pressure (0, 0.24, 1.14, 1.32, 1.56, 1.72, 1.89 and 2.15 GPa) on temperature dependence of resistivity of $CeRh_{0.75}Pd_{0.25}In_5$, as shown in Fig. 43 (*a*). The values of pressure were determined from difference of the manganin resistivity at room temperature and $\Delta p \sim 0.3$ GPa given by the physical properties of Daphne oil at various temperatures as discussed in Section 4.8. Previous works [163-165], which were studying the effect of pressure on $CeRhIn_5$, determined either precise values of pressure at low temperatures by inductively measuring the shift of Sn's superconducting transition temperature [165] or they have not mentioned any experimental details [79] at all. The application of different pressure determination methods do not prevent from comparing the absolute values of pressure considering negligible deviation of the $\Delta p$ from 0.3 GPa (see Fig. 25).

Similar to $CeRhIn_5$, the resistivity curves of the Pd-doped compound reveal maxima enhanced with increasing pressure. The peak temperature $T_{max}$ initially decreases, then it passes through a minimum at $\sim 1.32$ GPa and increases with further increasing pressure (see inset in Fig. 43 (*a*)). The pressure minimum of $T_{max}$ is somewhat lower than the minimum $\sim 1.7$ GPa presented in Ref. [100]. The maxima in resistivity curves are associated with coherence effects among Ce 4*f* spins hybridized with itinerant electrons [100].
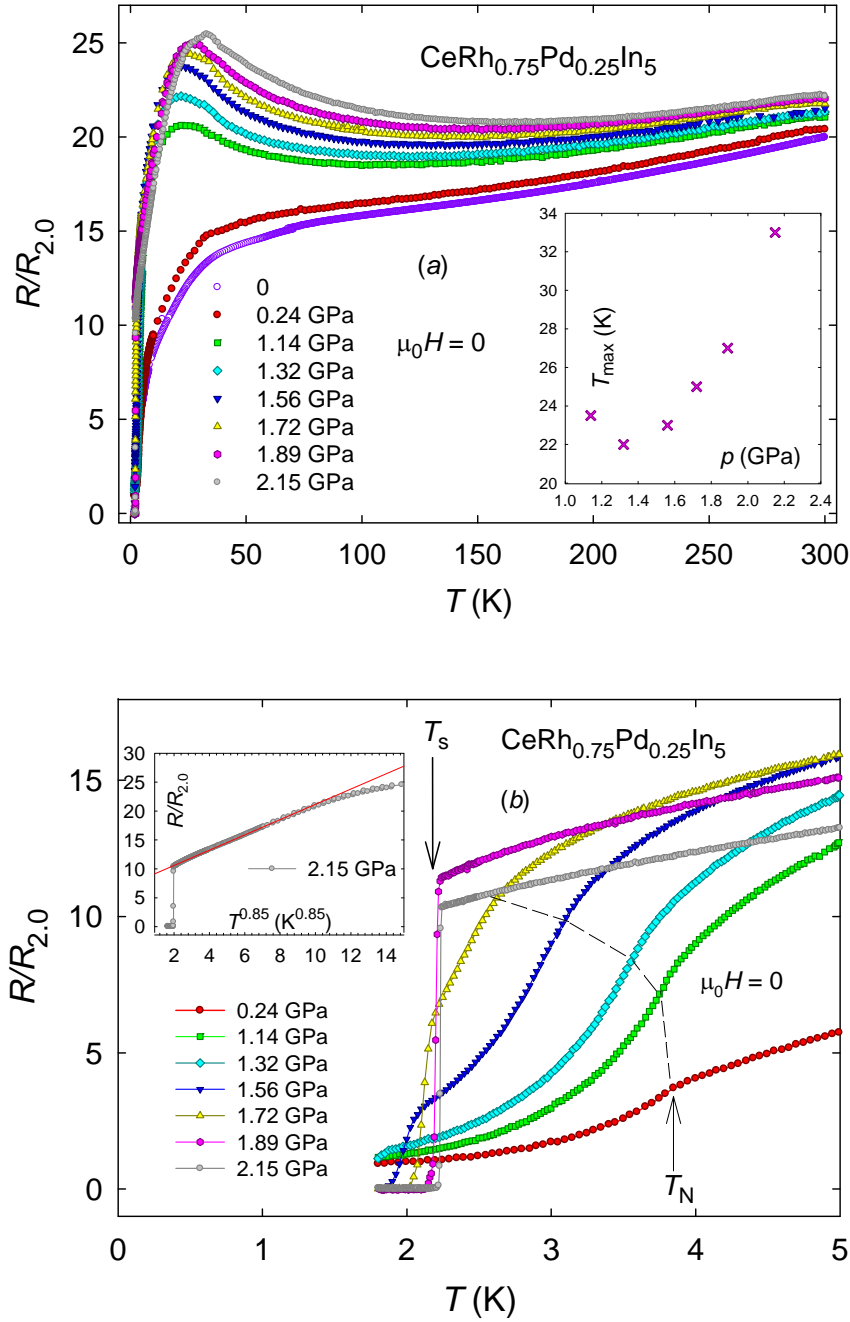
Fig. 43: (*a*) - Temperature dependence of the electrical resistivity of $CeRh_{0.75}Pd_{0.25}In_5$ under pressure at zero magnetic field. The inset shows the evolution of $T_{max}$ with pressure; (*b*) - The low-temperature region of the *a*-axis resistivity of $CeRh_{0.75}Pd_{0.25}In_5$ measured in various hydrostatic pressures. The arrows mark the transition temperatures $T_s$ at $p = 1.89$ GPa, and $T_N$, the dashed line marks the evolution of the Néel temperature $T_N$. The transition temperatures $T_N$, and $T_s$ were determined from the temperature dependence of the derivative $d(R/R_{2.0})/dT$. The red line shown in the inset represents a linear fit to resistivity curve measured in 2.15 GPa.

While the transition temperature to AF order does not change significantly at first with increasing pressure, the resistivity curve measured in 1.32 GPa indicates the onset of the superconductivity in the lowest measured temperatures (see Fig. 43 (*b*)). At this point, the

Néel temperature starts to decrease with pressure, pointing to a correlation between both phenomena [100]. The SC transition emerges clearly at $T_s = 1.97 \pm 0.10$ K at pressure $p \sim 1.56$ GPa and the SC and AF transition temperatures are equal when the pressure reaches critical value of $p_{c1} \sim 1.9$ GPa (see Fig. 44), which is close to the value presented in Ref. [166]. Higher pressures (above 1.9 GPa) lead to suppression of AF order and to further slight increase of superconducting temperature to $T_s = 2.23 \pm 0.02$ K at $p = 2.15$ GPa. This value corresponds to $T_s = 2.22 \pm 0.02$ K at $p = 2.35$ GPa for CeRhIn$_5$ presented in Ref. [165]. The extrapolation of the pressure dependence of $T_N$ reaches $T = 0$ at $p_{c2} \sim 2.5$ GPa where only SC phase survives; similarly to Ref. [166]. Very narrow SC transitions in resistivity curves indicate a good hydrostatic environment.

Analysis of the temperature exponent $n$ over a temperature range of $\sim 2 - 11$ K (above $T_s$) shows that electrical resistivity exhibits linear $T$-dependence at $p = 2.15$ GPa with $n$ equal to 0.85; thus the NFL behavior region develops at similar pressure as in CeRhIn$_5$ from Ref. [163] (see inset of Fig. 43 (*b*)).

The $T$-$p$ phase diagram of CeRh$_{0.75}$Pd$_{0.25}$In$_5$ is very similar to the one of CeRhIn$_5$ (see Fig. 44). While AF transition temperature changes due to substitution negligibly, the SC temperature is enhanced by Pd content in the pressure range $\sim 1.5 - 2$ GPa compared to previous results from specific heat data for CeRhIn$_5$ [166]. Different methods (specific heat, resistivity, nuclear quadrupole resonance) may lead to slightly different values of $T_s$, however the difference between CeRh$_{0.75}$Pd$_{0.25}$In$_5$ and CeRhIn$_5$ at ~1.5 GPa is significant. The fact, that CeCoIn$_5$ and CeIrIn$_5$ reveal higher values of SC transition temperatures than their 218 equivalents, suggests that this slight enhancement of $T_s$ can be expected, considering the superconductivity of Ce$_2$PdIn$_8$ below $T_s \sim 0.7$ K.
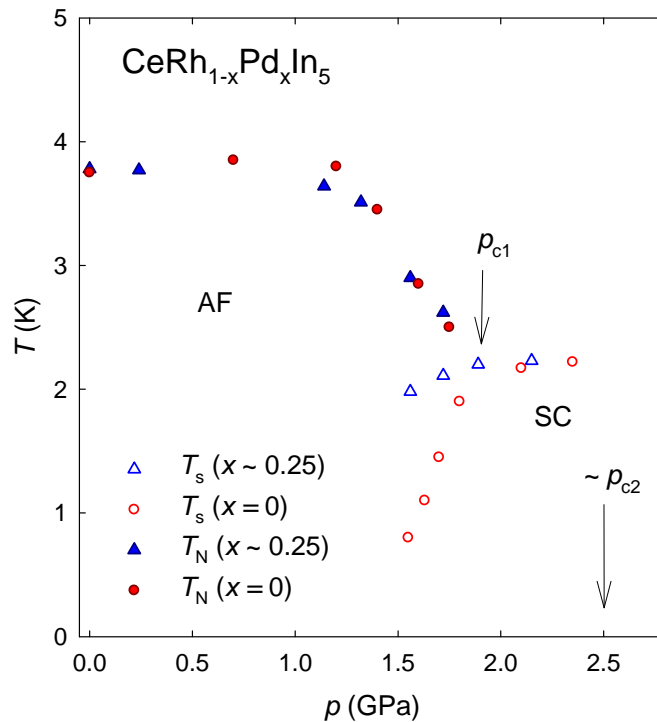


Fig. 44: $T$-$p$ phase diagram for CeRh$_{0.75}$Pd$_{0.25}$In$_5$ and CeRhIn$_5$. The values of $T_N$ and $T_s$ for CeRhIn$_5$ were taken from Ref. [166] and Ref. [165], respectively; The values for CeRh$_{0.75}$Pd$_{0.25}$In$_5$ were determined based on resistivity measurements shown in Fig. 43.

## Ce$_2$Rh$_{1-x}$Pd$_x$In$_8$

Single-crystal X-ray diffraction confirmed the Ho$_2$CoGa$_8$ structure of Ce$_2$Rh$_{1-x}$Pd$_x$In$_8$ for all $x = 0, 0.10, 0.15, 0.30, 0.45$ and $0.85$ with room temperature lattice parameters presented in Fig. 45; the lattice parameter $a$ expands and lattice parameter $c$ shrinks with increasing $x$ following the tendency between Ce$_2$RhIn$_8$ and Ce$_2$PdIn$_8$ structure. As the result, the unit cell volume increases with rising Pd content.



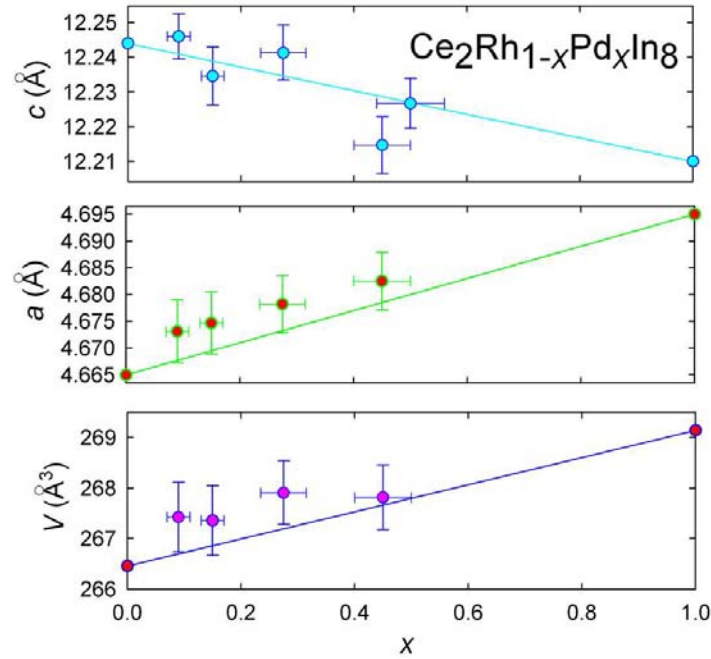Fig. 45: Lattice parameters of Ce$_2$Rh$_{1-x}$Pd$_x$In$_8$. The horizontal error bars are based on the scatter of stoichiometry checked by EDX analysis, the vertical error bars are based on deviations given by the Crystal Clear software.

In Fig. 46, the temperature dependence of specific heat of Ce$_2$Rh$_{1-x}$Pd$_x$In$_8$ in zero magnetic field is presented. The Néel temperature monotonically decreases with increasing $x$ and for $x \sim 0.45$ the antiferromagnetism is suppressed. In Ce$_2$RhIn$_8$ additional anomaly at 1.4 K is observed. It was previously reported as magnetic phase transition [96], however the magnetic structure has not been explained. This anomaly is suppressed already in samples with $x = 0.1$.
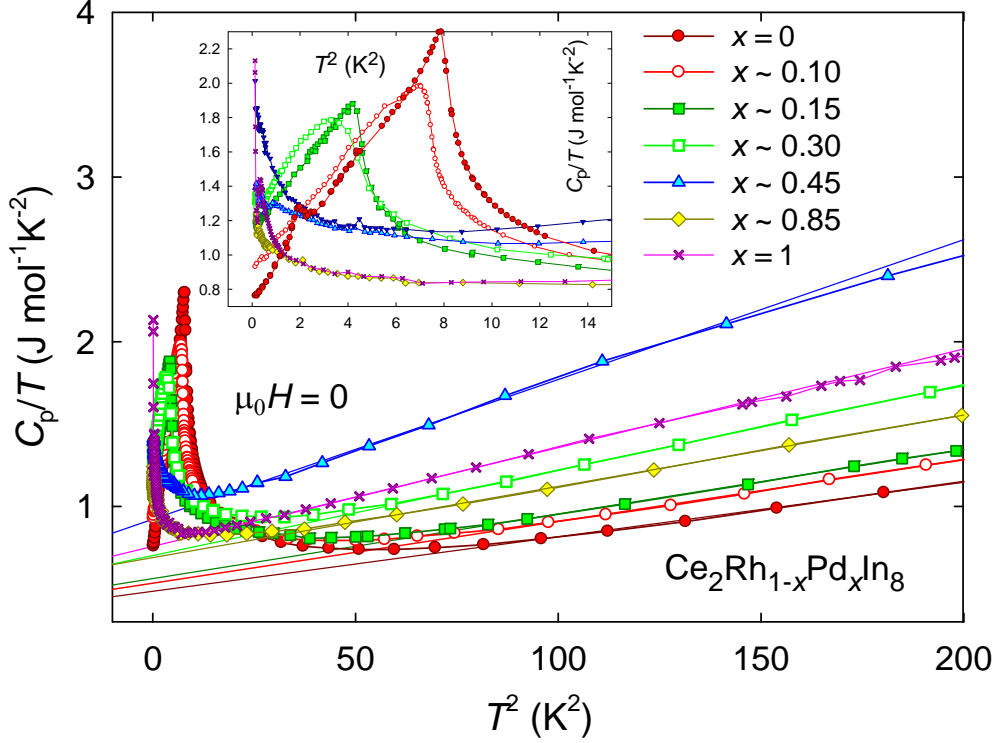
Fig. 46: The temperature dependence of heat capacity (plotted as $C_p/T$ vs $T^2$) data of Ce$_2$Rh$_{1-x}$Pd$_x$In$_8$ measured for various Pd concentrations $x$ in zero magnetic field. The lines represent the electronic part of specific heat contribution. The inset shows the low temperature region.

We have studied the influence of Pd doping on Kondo temperature of Ce$_2$Rh$_{1-x}$Pd$_x$In$_8$. There are several methods of estimating the value of $T_K$; in this work, the evaluation of $T_K$ based on a simple two-level model considering the reduction of magnetic entropy at $T_N$ was used [148]. Various methods of estimating $T_K$ [148,167] give different results compared to each other, but similar general trends in the evolution of $T_K$ across the series are observed [148]. Considering this fact, we do not propose any precise estimating of $T_K$, but we present its clear evolution for the prepared substitutions. We evaluated $T_K \sim 6$ K for the pure phase and $T_K \sim 12$ K for the sample with $x \sim 0.30$; therefore, the further increase of Kondo temperature for higher $x$ connected with the reduction of magnetic entropy with respect to the value of $R \ln 2$ was observed. The magnetic entropy was calculated from the magnetic contribution of the heat capacity (see Fig. 47).

The value of $T_K$ of Ce$_2$RhIn$_8$ is the same order of magnitude as the value of $T_K \approx 10$ K presented by Malinowski [167].
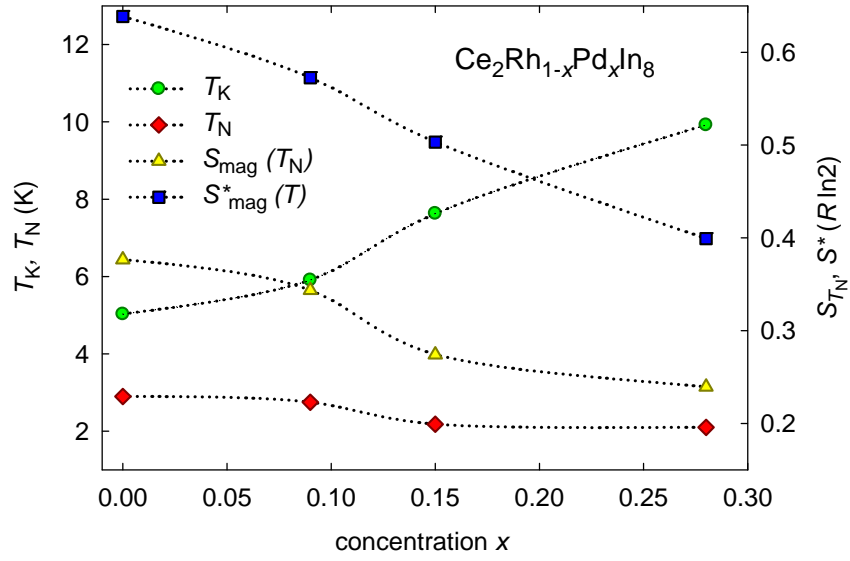
Fig. 47: Dependence of Kondo and Néel temperatures $T_K$ and $T_N$, respectively and dependence of magnetic entropy $S_{T_N}$ at $T_N$, and magnetic entropy $S^*$ of the magnetic transition, respectively, on concentration $x$ of $Ce_2Rh_{1-x}Pd_xIn_8$. Dotted lines are only guides to the eyes.
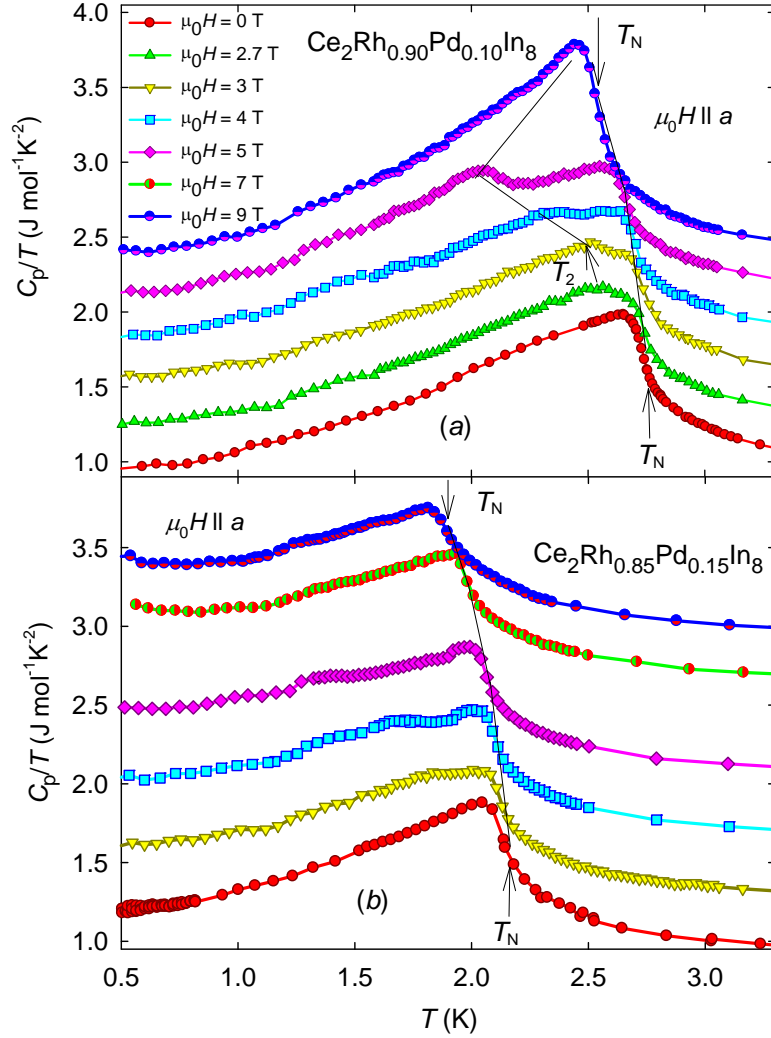
Fig. 48: The low-temperature region of heat capacity data of $Ce_2Rh_{1-x}Pd_xIn_8$ measured for various magnetic fields applied along *a*-axis for concentrations $x \sim 0.10$ (*a*) and 0.15 (*b*). The arrows and lines show the evolution of the transition temperatures $T_N$ and $T_2$. The curves measured in different magnetic fields are shifted equidistantly for better clarity.

The specific heat of $Ce_2Rh_{1-x}Pd_xIn_8$ for $x = 0.1$ and 0.15 is shown in Fig. 48 (*a*) and (*b*), respectively. Similar to $Ce_2RhIn_8$[96], in magnetic field applied along *a*-axis, a magnetic field transition at $T_2$ was observed. The evolutions of Néel temperature $T_N$ and the field-induced transition at $T_2$ are presented via arrows and lines. The transition at $T_2$ can be compared with the second-order magnetic field-induced transition in $Ce_2RhIn_8$[96] as it has similar evolution with magnetic field. Both transitions $T_N$ and $T_2$ can be detected in specific heat data till $x = 0.15$. The field-induced anomaly decays quickly; for sample with $x > 0.15$ the magnetic field transition is completely suppressed and only antiferromagnetic transition is observed. The transition temperatures shift to lower temperatures with increasing concentration of Pd similarly to $CeRh_{1-x}Pd_xIn_5$ substitutions, but the sensitivity to Pd content is stronger for anomalies in Pd-doped $Ce_2RhIn_8$, which may also correspond to the fact that the lattice parameters of $Ce_2Rh_{1-x}Pd_xIn_8$ change more significantly.

The *T-x* phase diagram of $Ce_2Rh_{1-x}Pd_xIn_8$ is presented in Fig. 49. The temperatures $T_N$, $T_{N2}$ and $T_s$ are estimated using a combination of the position of the peaks from Fig. 46 and

from extrapolation of $T_N$ to zero temperature. The Sommerfeld coefficient $\gamma$ increases monotonically till the AF order (indicated by red diagonal stripes) is completely suppressed by rising Pd content and then decreases abruptly; the decrease of $\gamma$ is followed by another increase in the higher Pd concentration range (see the fits of $\gamma$ in Fig. 46). The $\gamma \sim 240$ mJ mol$^{-1}$ Ce K$^{-2}$ for the pure phase of Ce$_2$RhIn$_8$ is roughly a half of value presented by Nicklas $et$ $al.$ [99]. Also the value of $\gamma$ for Ce$_2$PdIn$_8$ is significantly lower than the value determined in Ref. [13]. The superconducting transition temperature $T_s$ is observed only in the case of pure Ce$_2$PdIn$_8$.
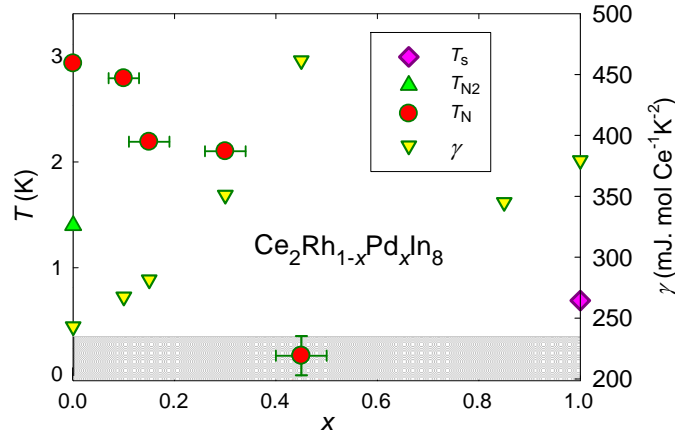


Fig. 49: The phase diagram of Ce$_2$Rh$_{1-x}$Pd$_x$In$_8$ constructed from specific heat data only; the Néel temperature $T_N$ shows gradual decrease, around $x = 0.45$, the antiferromagnetism is suppressed. Temperature $T_{N2}$, indicated by a filled triangle, represents the order to order magnetic transition [96] observed only in Ce$_2$RhIn$_8$. The critical temperature $T_s$ is taken from Ref. [20,21]. The evolution of concentration dependence of the Sommerfeld coefficient $\gamma$ is a result of specific heat analysis. The gray region represents temperatures below 0.35 K we have not reached by any of our experiments. The horizontal error bars were determined from EDX analysis. The vertical error bar for $x \sim 0.45$ is given by the gray region.

The inverse susceptibility ($1/\chi$) of Ce$_2$Rh$_{1-x}$Pd$_x$In$_8$ measured for several concentrations of Pd in magnetic field of 5 T oriented along both crystallographic directions, is shown in Fig. 50. The parameters determined from C-W law are presented in Tab. 9. The inverse susceptibility measured in magnetic field oriented in the basal plane deviates from its linear character as the crystal field effects become important; the deviation proceeds at markedly lower temperatures than in the perpendicular orientation, similarly to CeRh$_{1-x}$Pd$_x$In$_5$ compounds.

The values for Ce$_2$RhIn$_8$ differ strongly from those presented in Ref. [168] (see Tab. 9)- the magnetic moment $\mu_{eff}$ is significantly higher and the paramagnetic temperature $\theta_P$ is much lower in both crystallographic directions. The doped samples reveal lower $\mu_{eff}$ and higher $\theta_P$ than both boundary phases, forming a minimum and maximum, respectively, in the concentration dependence of these two parameters. Considering the values for Ce$_2$RhIn$_8$ presented in Ref. [168], there would be probably no such an extreme in the curve indicating the monotonic (within the uncertainty given by mass deviation) evolution of $\theta_P$ and $\mu_{eff}$ with increasing Pd concentration. It is necessary to consider that the deviation of the $\theta_P$ and $\mu_{eff}$ can reach up to 10 % due to experimental error (small sample mass $\sim 2 - 3$ mg). The values of $\mu_{eff}$ were rounded for these reasons (except the values published in Ref. [168]). The difference of $\theta_P$ and $\mu_{eff}$ in case of Ce$_2$RhIn$_8$ cannot be explained using only the mass deviation. The concentration dependence of $\mu_{eff}$ and $\theta_P$ resembles that of CeRh$_{1-x}$Pd$_x$In$_5$ substitutions, but due

to the absence of the pure CePdIn$_5$ phase we cannot decide about the presence of minimum and maximum, respectively. However, the different character of the curves of the Pd-rich ($x \sim 0.85$, 1) and Rh-rich ($x = 0$, 0.15) substitutions in the low-temperature region ($T < \sim 60$ K) can be clearly observed. There is a decrease of $1/\chi$ in both $a$- and $c$-direction below 8 K for Pd-rich compounds, while $1/\chi$ of Rh-rich substitutions becomes constant gradually. This fact also indicates that compounds with "impurity" concentration $x \sim 0.15$ still retain their physical properties, which corresponds to results from specific heat.
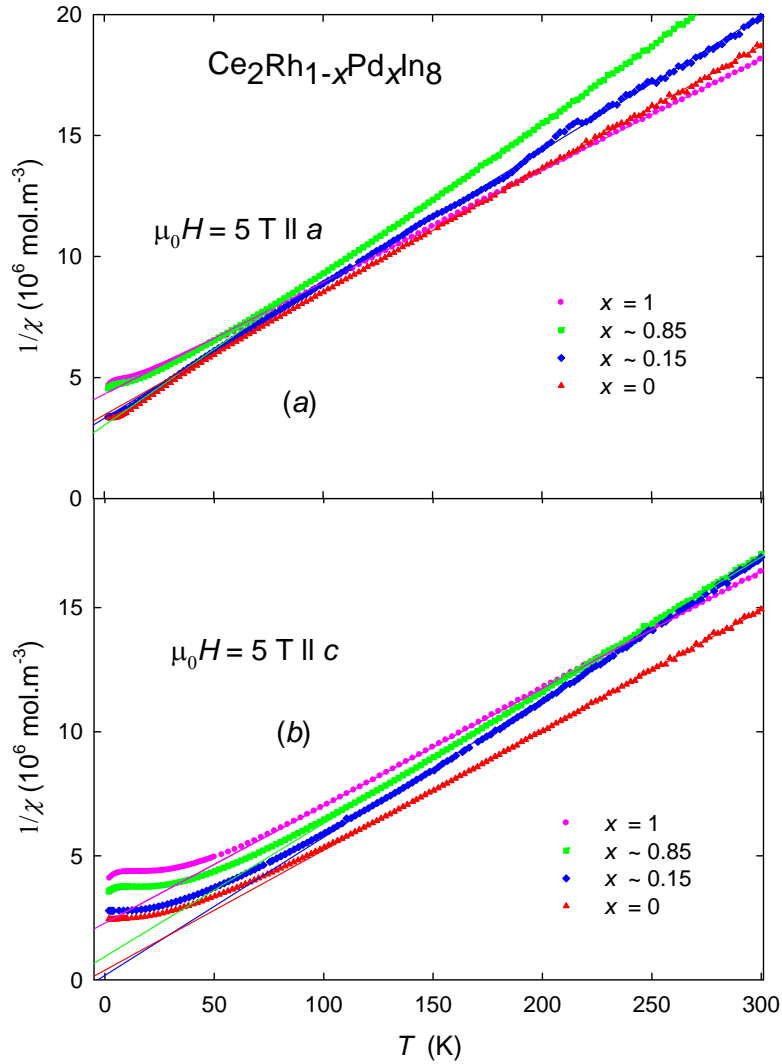


Fig. 50: The temperature dependence of inverse susceptibility of Ce$_2$Rh$_{1-x}$Pd$_x$In$_8$ for several concentrations of Pd measured in magnetic field of 5 T oriented along the $a$-axis ($a$) and $c$-axis ($b$), respectively. The lines represent the fits of C-W law in the appropriate temperature ranges. Data for $x = 1$ are taken from Ref. [21].

| $x$ | temperature range of CW fit (K) | | $\theta_P$ (K) | | $\mu_{eff}$ ($\mu_B$/Ce$^{3+}$) | |
|---|---|---|---|---|---|---|
| | ll $a$ | ll $c$ | ll $a$ | ll $c$ | ll $a$ | ll $c$ |
| 0 | 60-300 | 100-300 | -68 | -8 | 2.5 | 2.6 |
| 0 [168] | - | - | -40 | 12 | 2.32 | 2.38 |
| 0.15 | 20-300 | 90-300 | -60 | -3 | 2.4 | 2.4 |
| 0.85 | 60-300 | 100-300 | -48 | -17 | 2.3 | 2.4 |
| 1 | 22-300 | 70-300 | -90 | -50 | 2.6 | 2.6 |

Tab. 9: The concentration dependence of the paramagnetic Curie temperature $\theta_P$ and the effective magnetic moment $\mu_{eff}$ of Ce$_2$Rh$_{1-x}$Pd$_x$In$_8$ together with the temperature ranges used for C-W fitting. The results for $x = 0$ are compared with those presented in Ref. [168].

## Ce$_2$PdIn$_8$ - annealing

With respect to recent results reporting superconductivity in polycrystalline Ce$_2$PdIn$_8$ after annealing at 700 ˚C [20], we have prepared new series of Ce$_2$PdIn$_8$ single crystals to study the effect of annealing. The heat capacity measurement presented in Fig. 51 revealed a SC transition at $T_s = 0.52$ K. The superconductivity was suppressed after annealing at 650 °C.
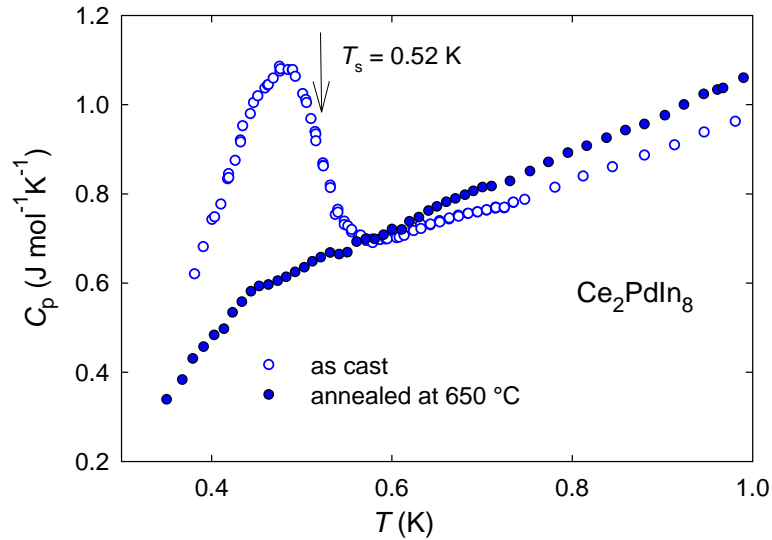


Fig. 51: Low-temperature region of heat capacity of Ce$_2$PdIn$_8$.

In Fig. 51 the measurement of sample with superconducting transition at $T_s = 0.52$ K is presented. After annealing at 650 ˚C (12 days) the SC was suppressed. Further annealing of the same sample at 700 ˚C for (1 week) led to decomposition of the single crystal to CeIn$_3$ and Ce$_4$Pd$_{10}$In$_{21}$. This is unlikely the presenter results on polycrystals; the sample, we have studied, was rather small (~ 2 mg) and local composition non-homogeneity could initiate the transformation. The other possibility is that in general the temperature of 700 ˚C is very close to composition sensitive peritectic transformation of Ce$_2$PdIn$_8$.

## Ce$_4$Pd$_{10}$In$_{21}$

Single-crystal X-ray diffraction confirmed the Ho$_4$Ni$_{10}$Ga$_{21}$ monoclinic structure, the lattice parameters were determined as $a = 23.1522$ Å, $b = 4.5514$ Å, $c = 17.2433$ Å and $\beta = 124.59°$.

72

We have studied heat capacity down to 0.35 K, to get basic ideas about possible influence on extrinsic properties of $Ce_2PdIn_8$. The heat capacity measurement on several single crystals (total mass ~ 0.5 mg) in zero magnetic field and field of 2 and 5 T applied perpendicular oriented is presented in Fig. 52. The peak below 1 K suggests magnetic ordering at $T = 0.8$ K. Assuming $Ce^{3+}$ ions to be responsible for the magnetism of $Ce_4Pd_{10}In_{21}$, and considering two nonequivalent positions of $Ce^{3+}$ positions in the crystal structure, we cannot conclude on type of magnetic ordering of $Ce_4Pd_{10}In_{21}$ from the heat capacity data.
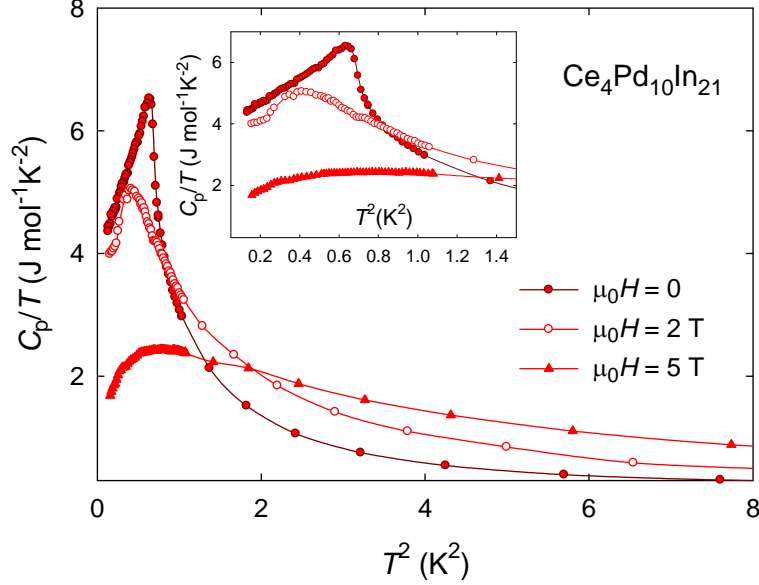


Fig. 52: Heat capacity data of $Ce_4Pd_{10}In_{21}$. The inset shows the low-temperature region.

## 5.2.3. Summary

We have prepared single crystals of $Ce_nRhIn_{3n+2}$ ($n = 1$, 2) doped by Pd and $Ce_2PdIn_8$ from In flux. Despite of several difficulties concerning the synthesis of the doped samples (sharing the problems with the growth of $Ce_2PdIn_8$) we were able to select samples appropriate for further measurements.

The highest Pd concentration in 115 substitutions suitable for measurements reached only 0.25 because the growth of 218 equivalents was preferred for higher Pd content. The specific heat measurement of $CeRh_{1-x}Pd_xIn_5$ ($x = 0.1$ and 0.25) has shown a slight decrease of the Néel temperature with increasing Pd content; the suppression of AF order was not achieved and is expected for much higher Pd content which we could not reach. We have also observed two magnetic field-induced transitions $T_1$ and $T_2$ in all prepared samples. These transitions are shifted to lower temperatures with increasing Pd concentration, however their evolution in various magnetic fields is in good agreement with data published in Ref. [96] for $CeRhIn_5$ and our own measurement on $CeRhIn_5$. Therefore we assume the magnetic structure in the doped systems to be similar to $CeRhIn_5$. The behavior of $CeRh_{0.75}Pd_{0.25}In_5$ compound was investigated also by means of preliminary pressure measurements up to hydrostatic pressure ~ 2.2 GPa in temperatures down to 1.8 K. The $T$-$p$ phase diagram resembles strongly the one presented in Ref. [100] for $CeRhIn_5$. The Pd content did not affect the pressure evolution of AF transition temperature significantly, however, the superconducting temperature is shifted to somewhat higher values by the concentration $x = 0.25$. This fact could indicate that the $CeRh_{1-x}Pd_xIn_5$ system would incline to reveal superconductivity with higher Pd content,

however further measurements using higher pressures and also lower temperatures need to be done. For better comparison of the Pd doped samples with CeRhIn$_5$, our own pressure measurements on CeRhIn$_5$ will be useful.

We have prepared several single crystals of Ce$_2$Rh$_{1-x}$Pd$_x$In$_8$ with Pd concentrations $x = 0$, 0.10, 0.15, 0.30, 0.45 and 0.85. Unfortunately the middle region of concentrations in this system was difficult to reach. The specific heat measurement of Ce$_2$Rh$_{1-x}$Pd$_x$In$_8$ revealed gradual suppression of Néel temperature upon doping with Pd; no antiferromagnetic order is observed for $x \sim 0.45$ down to 0.35 K. The 218 substitutions are more sensitive to the Pd content than their 115 equivalents. Similar to CeRh$_{1-x}$Pd$_x$In$_5$, magnetic field-induced transitions $T_1$ and $T_2$ were observed and their evolution in various magnetic fields resembles data published in Ref. [96] for Ce$_2$RhIn$_8$. The study of Kondo interactions in Ce$_2$Rh$_{1-x}$Pd$_x$In$_8$ revealed an increase of $T_K$ with increasing Pd doping.

Magnetic measurements and consequent analysis of C-W behavior indicate that the Pd content decreases effective magnetic moment and increases the paramagnetic temperature of both 218 and 115 substitutions.

Contrary to the previous work [21], annealing of Ce$_2$PdIn$_8$ single crystal with initial (as cast) $T_s = 0.52$ K led gradually to suppression of superconductivity and decomposition (at 700°C) to CeIn$_3$ and Ce$_{10}$Pd$_4$In$_{21}$ phases. However, the annealed single crystal was very small compared to polycrystalline samples which might significantly influence the annealing process. Considering persisting complications with the growth of high quality single crystals of Ce$_2$PdIn$_8$ (no single phased single crystals of Ce$_2$PdIn$_8$ have been presented up to now) we performed series of experiments based on DTA analysis. First results shown in Appendix A indicate that it is necessary to lower the maximum growth temperature, which is reached during the thermal process, to $T < 800°C$, to avoid the growth of CeIn$_3$ and to improve the quality of single crystals.

# 6.      General conclusions

We have studied two series of compounds performing a broad spectrum of physical properties. While $YPd_2Al_3$ is a representative of the group of conventional superconductors, the member of $Ce_nT_mIn_{3n+2m}$ system often exhibit rather complicated magnetic structures and their coexistence with superconductivity, which has an unconventional character [7].

Based on our previous work on $SmPd_2Al_3$ [17,18] we have studied $YPd_2Al_3$, a new member of $REPd_2Al_3$ compounds. The measurements on polycrystalline samples revealed that $YPd_2Al_3$ exhibits superconductivity below 0.6 K. The critical temperature $T_s$ was significantly enhanced by annealing (at 700 °C for 14 days) to $T_s \sim 2.2$ K, which was determined by resistivity, heat capacity and AC susceptibility measurements. The theoretical calculations revealed significant lower values of $T_s$ compared to experimentally determined ones, pointing to complex nature of the phonon spectra of $YPd_2Al_3$ which is question of further computations.

The studies of $Ce_2Rh_{1-x}Pd_xIn_8$ and $CeRh_{1-x}Pd_xIn_5$ were connected with complicated sample synthesis. Although the solution growth method is commonly used for the synthesis of $Ce_nT_mIn_{3n+2m}$ compounds and all their substitutions with Co, Rh and Ir [108-112], the stability of the phases containing Pd is lower leading to many difficulties. $CePdIn_5$ has not been synthesized yet. Despite of this, we have succeeded in synthesis of several samples and came to interesting results.

The Pd doping in $CeRhIn_5$ showed only small impact on the physical properties; the characteristic AF transition temperatures remained almost unchanged and superconducting transition temperatures were shifted to somewhat higher values in case of pressure experiments on $CeRh_{0.75}Pd_{0.25}In_5$. This might not seem to be important since we only succeeded to prepare samples with $x = 0.25$; however the doping within Co, Rh and Ir affects the antiferromagnetism and/or superconductivity much faster [108-112].

Despite of the existence of $Ce_2PdIn_8$ phase, the studies of $Ce_2Rh_{1-x}Pd_xIn_8$ system was in some sense more difficult. We have prepared single crystals mostly in the Rh and Pd rich region. In the Rh rich region a clear decrease of Néel temperature with increasing Pd content was observed, however samples with the crucial concentrations around $x = 0.45$ where the antiferromagnetism is expected to vanish were not synthesized. Due to high sensitivity of superconducting phase transition in $Ce_2PdIn_8$ it was also difficult to study the impact of Pd doping in the Pd rich region.

We tried to improve the quality of $Ce_2PdIn_8$ by changing the growth conditions. Almost 30 growth experiments were done and characterization of the samples was based on careful X-ray and microprobe analysis; about 7 samples were selected for specific heat and resistivity measurements down to 0.35 K. None of them presented one single-phase superconducting transition around 0.7 K, as presented for annealed polycrystals [20]. Based on this publication, annealing was also tried on a selected single crystal with well defined superconducting transition at 0.52 K; however without success.

Recently installed instrument by SETARAM Instrumentation Company, providing the differential thermal analysis, represents useful support to improve the growth conditions. As presented in Appendix A, we have performed several experiments using DTA analysis in order to find the proper conditions for the growth of $Ce_2PdIn_8$. Preliminary results show that the lower growth temperatures suppress the formation of unwanted impurity phase $CeIn_3$; however detail characterization of the prepared samples has not been done yet. Further experiments are still in progress.

# References

1.  V. Nekvasil a M. Diviš: Localized 4f and 5f Moments: Magnetism in Encyclopedia of Materials: Science and Technology, edited by K. H. J. Buschow et al. (Elsevier, Oxford, 2001), p.4613.

2.  Ch. Kittel: Úvod do fyziky pevných látek (Academia, Praha 1985).

3.  S. Blundell: Magnetism in Condensed Matter (Oxford University Press, Oxford, 2004).

4.  B. Coqblin: Electron Systems: Strong Correlation in Encyclopedia of Materials: Science and Technology, edited by K. H. J. Buschow et al. (Elsevier, Oxford, 2001), p. 2591.

5.  A. S. Edelstein, Journal of Magnetism and Magnetic Materials **256,** 430 (2003).

6.  F. Steglich, J. Aarts, C. D. Bredl, W. Lieke, D. Meschede, W. Franz, and H. fer, Phys. Rev. Lett. **43,** 1892 (1979).

7.  C. Pfleiderer, Rev. Mod. Phys. **81,** 1551 (2009).

8.  N. T. Huy, et al., Phys. Rev. Lett. **99,** 067006 (2007).

9.  D. Kaczorowski, A. P. Pikul, D. Gnida, and V. H. Tran, Phys. Rev. Lett. **103,** (2009).

10. K. Uhlířová, J. Prokleška, and V. Sechovský, Phys. Rev. Lett. **104,** (2010).

11. D. Kaczorowski, A. P. Pikul, D. Gnida, and V. H. Tran, Phys. Rev. Lett. **104,** 059702 (2010).

12. D. Shtepa, S. Nesterenko, A. Tursina, E. Murashova, and Y. Seropegin, Moscow University Chemistry Bulletin **63,** 162 (2008).

13. D. Kaczorowski, A. Pikul, B. Belan, L. Sojka, and Y. Kalychak, Physica B-Condensed Matter **404,** 2975 (2009).

14. E. D. Bauer, et al., Phys. Rev. B **81,** 180507 (2010).

15. K. Ghosh, S. Ramakrishnan, A. D. Chinchure, V. R. Marathe, and G. Chandra, Physica B: Condensed Matter **223-224,** 354 (1996).

16. K. Ghosh, S. Ramakrishnan, S. K. Malik, and G. Chandra, Phys. Rev. B **48,** 6249 (1993).

17. M. Kratochvílová: Magnetické a termodynamické vlastnosti $REPd_2Al_3$ sloučenin (bakalářská práce, Praha, 2009).

18. J. Pospíšil, M. Kratochvílová, J. Prokleška, M. Diviš, and V. Sechovský, Phys. Rev. B **81,** 024413 (2010).

19. S. A. M. Mentink, N. M. Bos, G. J. Nieuwenhuys, A. A. Menovsky, and J. A. Mydosh, Physica B: Condensed Matter **186-188,** 497 (1993).

20. D. Kaczorowski, D. Gnida, A. P. Pikul, and V. H. Tran, Solid State Communications **150,** 411 (2010).

21. K. Uhlířová, J. Prokleška, V. Sechovský, and S. Daniš, Intermetallics **18,** 2025 (2010).

22. N. W. Ashcroft and N. W. Mermin: Solid State Physics (Thomson Learning, 1976).

23. J. Klíma a B. Velický: Kvantová teorie II (MFF UK, Praha, 1990).

24. V. Sechovský: General Introduction: in Encyclopedia of Materials: Science and Technology, edited by K. H. J. Buschow et al. (Elsevier, Oxford, 2001), p. 5018.

25. M. Diviš: lecture notes.

26. www.cmp.liv.ac.uk/frink/thesis/thesis/node71.html.

27. G. Rancour: Magnetism of Earth Planetary, and Environmental Nanomaterials (Department of Physics, University of Ottawa, Ottawa, Ontario, Canada K1N 6N5, 2001).

28. S. Ishiwata, Y. Taguchi, H. Murakawa, Y. Onose, and Y. Tokura, Science **319,** 1643 (2008).

29. P. Javorský: lecture notes.

30. H. V. Lõhneysen: Non-Fermi Liquid Behaviour in Encyclopedia of Materials: Science and Technology, edited by K. H. J. Buschow et al. (Elsevier, Oxford, 2001), p. 6185.

31. F. Steglich and S. Sullow: Heavy-fermion Systems in Encyclopedia of Materials: Science and Technology, edited by K. H. J. Buschow et al. (Elsevier, Oxford, 2001), p. 3746.

32. Ch. Kittel: Introduction to Solid State Physics - 7th Edition (John Wiley and sons, New York, 1996).

33. B. Coqblin: The Electronic Structure of Rare-Earth Metals and Alloys: The Magnetic Heavy Rare-Earths (Academic Press, London, 1977).

34. E. Bauer: Intermediate Valence Systems in Encyclopedia of Materials: Science and Technology, edited by K. H. J. Buschow et al. (Elsevier, Oxford, 2001), p. 4148.

35. B. T. Matthias, M. Peter, H. J. Williams, A. M. Clogston, E. Corenzwit, and R. C. Sherwood, Phys. Rev. Lett. **5,** 542 (1960).

36. P. W. Anderson, Phys. Rev. **124,** 41 (1961).

37. P. W. Anderson, Rev. Mod. Phys. **50,** 191 (1978).

38. L. Havela: lecture notes.

39. J. Kondo, Progress of Theoretical Physics **32,** 37-& (1964).

40. G. J. van den Berg: Proceedings of the 7th International Conference on Low Temperature Physics (University of Toronto Press, 1961).

41. K. G. Wilson, Rev. Mod. Phys. **47,** 773 (1975).

42. E. Bauer: Kondo Systems and Heavy Fermions: Transport Phenomena in Encyclopedia of Materials: Science and Technology, edited by K. H. J. Buschow et al. (Elsevier, Oxford, 2001), p. 4372.

43. S. Ohara, Y. Shomi, and I. Sakamoto, Physica B: Condensed Matter **329-333,** 612 (2003).

44. D. L. Cox and N. Grewe, Zeitschrift f+-r Physik B Condensed Matter **71,** 321 (1988).

45. S. Doniach, Physica B & C **91,** 231 (1977).

46. J. R. Iglesias, C. Lacroix, and B. Coqblin, Phys. Rev. B **56,** 11820 (1997).

47. Z. Arnold: High pressure in basic and material science, lecture notes.

48. T. Moriya and T. Takimoto, Journal of the Physical Society of Japan **64,** 960 (1995).

49. H. Kamerlingh Onnes, Comm. Phys. Lab. Univ. Leiden **122,** (1911).

50. J. Englich et al: Fyzika nízkých teplot (Matfyzpress, Praha, 1998).

51. J. Bardeen, L. N. Cooper, and J. R. Schrieffer, Phys. Rev. **108,** 1175 (1957).

52. http: and arq.lanl.gov/source/orgs/nmt/nmtdo/AQarchive /2ndQuarter05/page9.shtml.

53. F. Marsiglio et al: Electron-Phonon Superconductivity in Superconductivity: Novel superconductors (Springer Japan KK, 2008).

54. J. C. Swihart, D. J. Scalapino, and Y. Wada, Phys. Rev. Lett. **14,** 106 (1965).

55. N. R. Werthamer, E. Helfand, and P. C. Hohenberg, Phys. Rev. **147,** 295 (1966).

56. P. Monthoux, D. Pines, and G. G. Lonzarich, Nature **450,** 1177 (2007).

57. J. G. Bednorz and K. A. Muller, Zeitschrift fur Physik B-Condensed Matter **64,** 189 (1986).

58. S. S. Saxena, et al., Nature **406,** 587 (2000).

59. D. Fay and J. Appel, Phys. Rev. B **22,** 3173 (1980).

60. N. F. Berk and J. R. Schrieff, Phys. Rev. Lett. **17,** 433-& (1966).

61. C. Geibel, et al., Zeitschrift fur Physik B-Condensed Matter **84,** 1 (1991).

62. C. Geibel, et al., Physica C **185,** 2651 (1991).

63. C. Geibel, et al., Physica B **188,** 188 (1993).

64. A. Dönni, A. Furrer, H. Kitazawa, and M. Zolliker, Journal of Physics-Condensed Matter **9,** 5921 (1997).

65. A. Dönni, A. Furrer, E. Bauer, H. Kitazawa, and M. Zolliker, Zeitschrift fur Physik B-Condensed Matter **104,** 403 (1997).

66. M. Kyogaku, Y. Kitaoka, K. Asayama, C. Geibel, C. Schank, and F. Steglich, Journal of the Physical Society of Japan **62,** 4016 (1993).

67. E. J. Freeman, M. C. de Andrade, R. P. Dickey, N. R. Dilley, and M. B. Maple, Phys. Rev. B **58,** 16027 (1998).

68. V. S. Zapf, R. P. Dickey, E. J. Freeman, C. Sirvent, and M. B. Maple, Phys. Rev. B **65,** 024437 (2001).

69. S. Suga, M. Takeda, Y. Mori, N. Shino, S. Imada, and H. Kitazawa, Physica B: Condensed Matter **186-188,** 63 (1993).

70. A. Dönni, H. Kitazawa, P. Fischer, T. Vogt, A. Matsushita, Y. Iimura, and M. Zolliker, Journal of Solid State Chemistry **127,** 169 (1996).

71. H. Kitazawa, C. Schank, S. Thies, B. Seidel, C. Geibel, and F. Steglich, Journal of the Physical Society of Japan **61,** 1461 (1992).

72. K. Fujiwara, H. Okubo, and K. Kumagai, Physica B **230,** 240 (1997).

73. G. Motoyama, T. Nishioka, and N. K. Sato, Journal of the Physical Society of Japan **71,** 1609 (2002).

74. Z. Liu, Physica B: Condensed Matter **262,** 348 (1999).

75. T. Inami, N. Terada, H. Kitazawa, and O. Sakai, Journal of the Physical Society of Japan **78,** (2009).

76. H. Kitazawa, K. Hashi, H. Abe, N. Tsujii, and G. Kido, Physica B: Condensed Matter **294-295,** 221 (2001).

77. R. Movshovich, M. Jaime, J. D. Thompson, C. Petrovic, Z. Fisk, P. G. Pagliuso, and J. L. Sarrao, Phys. Rev. Lett. **86,** 5152 (2001).

78. M. Kenzelmann, et al., Science **321,** 1652 (2008).

79. H. Hegger, C. Petrovic, E. G. Moshopoulou, M. F. Hundley, J. L. Sarrao, Z. Fisk, and J. D. Thompson, Phys. Rev. Lett. **84,** 4986 (2000).

80. T. Park, F. Ronning, H. Q. Yuan, M. B. Salamon, R. Movshovich, J. L. Sarrao, and J. D. Thompson, Nature **440,** 65 (2006).

81. E. G. Moshopoulou, Z. Fisk, J. L. Sarrao, and J. D. Thompson, Journal of Solid State Chemistry **158,** 25 (2001).

82. A. M. Vandiepe, R. S. Craig, and W. E. Wallace, Journal of Physics and Chemistry of Solids **32,** 1867-& (1971).

83. I. R. Walker, F. M. Grosche, D. M. Freye, and G. G. Lonzarich, Physica C **282,** 303 (1997).

84. A. J. Millis, Phys. Rev. B **48,** 7183 (1993).

85. G. Knebel, D. Braithwaite, P. C. Canfield, G. Lapertot, and J. Flouquet, Phys. Rev. B **65,** 024425 (2001).

86. G. F. Chen, S. Ohara, M. Hedo, Y. Uwatoko, K. Saito, M. Sorai, and I. Sakamoto, Journal of the Physical Society of Japan **71,** 2836 (2002).

87. J. D. Thompson, et al., Journal of Magnetism and Magnetic Materials **226-230,** 5 (2001).

88. M. Yashima, S. Taniguchi, H. Miyazaki, H. Mukuda, Y. Kitaoka, H. Shishido, R. Settai, and Y. Onuki, Phys. Rev. B **80,** (2009).

89. H. Aoki, T. Sakakibara, H. Shishido, R. Settai, Y. Onuki, P. Miranovic, and K. Machida, Journal of Physics-Condensed Matter **16,** L13-L19 (2004).

90. K. Izawa, H. Yamaguchi, Y. Matsuda, H. Shishido, R. Settai, and Y. Onuki, Phys. Rev. Lett. **87,** (2001).

91. C. Petrovic, P. G. Pagliuso, M. F. Hundley, R. Movshovich, J. L. Sarrao, J. D. Thompson, Z. Fisk, and P. Monthoux, Journal of Physics-Condensed Matter **13,** L337-L342 (2001).

92. A. Bianchi, R. Movshovich, I. Vekhter, P. G. Pagliuso, and J. L. Sarrao, Phys. Rev. Lett. **91,** (2003).

93. R. Borth, E. Lengyel, P. G. Pagliuso, J. L. Sarrao, G. Sparn, F. Steglich, and J. D. Thompson, Physica B-Condensed Matter **312,** 136 (2002).

94. S. Raymond, E. Ressouche, G. Knebel, D. Aoki, and J. Flouquet, Journal of Physics-Condensed Matter **19,** (2007).

95. W. Bao, P. G. Pagliuso, J. L. Sarrao, J. D. Thompson, Z. Fisk, J. W. Lynn, and R. W. Erwin, Phys. Rev. B **62,** R14621 (2000).

96. A. L. Cornelius, P. G. Pagliuso, M. F. Hundley, and J. L. Sarrao, Phys. Rev. B **64,** (2001).

97. N. O. Moreno, M. F. Hundley, P. G. Pagliuso, R. Movshovich, M. Nicklas, J. D. Thompson, J. L. Sarrao, and Z. Fisk, Physica B: Condensed Matter **312-313,** 274 (2002).

98. M. Nicklas, V. A. Sidorov, H. A. Borges, P. G. Pagliuso, J. L. Sarrao, and J. D. Thompson, Phys. Rev. B **70,** (2004).

99. M. Nicklas, V. A. Sidorov, H. A. Borges, P. G. Pagliuso, C. Petrovic, Z. Fisk, J. L. Sarrao, and J. D. Thompson, Phys. Rev. B **67,** 020506 (2003).

100. T. Park, V. A. Sidorov, H. Lee, F. Ronning, E. D. Bauer, J. L. Sarrao, and J. D. Thompson, Journal of Physics: Condensed Matter **23,** 094218 (2011).

101. T. Park, E. D. Bauer, and J. D. Thompson, Phys. Rev. Lett. **101,** 177002 (2008).

102. G. F. Chen, S. Ohara, M. Hedo, Y. Uwatoko, and I. Sakamoto, Journal of Physics-Condensed Matter **15,** S2175-S2178 (2003).

103. J. S. Kim, N. O. Moreno, J. L. Sarrao, J. D. Thompson, and G. R. Stewart, Phys. Rev. B **69,** 024402 (2004).

104. W. Bao, P. G. Pagliuso, J. L. Sarrao, J. D. Thompson, Z. Fisk, and J. W. Lynn, Phys. Rev. B **64,** (2001).

105. E. Lengyel: Antiferromagnetism and Superconductivity in Ce-based Heavy-Fermion Systems (Cuvillier, 2007).

106. M. Koeda, T. Fujiwara, M. Hedo, Y. Uwatoko, H. Sagayama, Y. Wakabayashi, and H. Sawa, Journal of Magnetism and Magnetic Materials **310,** e31-e32 (2007).

107. E. G. Moshopoulou, R. M. Ibberson, J. L. Sarrao, J. D. Thompson, and Z. Fisk, Acta Crystallographica Section B **62,** 173 (2006).

108. P. G. Pagliuso, R. Movshovich, A. D. Bianchi, M. Nicklas, N. O. Moreno, J. D. Thompson, M. F. Hundley, J. L. Sarrao, and Z. Fisk, Physica B-Condensed Matter **312,** 129 (2002).

109. E. N. Hering, et al., Physica B: Condensed Matter **403,** 780 (2008).

110. P. G. Pagliuso, C. Petrovic, R. Movshovich, D. Hall, M. F. Hundley, J. L. Sarrao, J. D. Thompson, and Z. Fisk, Phys. Rev. B **64,** 100503 (2001).

111. A. Llobet, et al., Phys. Rev. Lett. **95,** 217002 (2005).

112. J. R. Jeffries, N. A. Frederick, E. D. Bauer, H. Kimura, V. S. Zapf, K. D. Hof, T. A. Sayles, and M. B. Maple, Phys. Rev. B **72,** 024551 (2005).

113. L. D. Pham, T. Park, S. Maquilon, J. D. Thompson, and Z. Fisk, Phys. Rev. Lett. **97,** 056404 (2006).

114. C. Adriano, C. Giles, L. Mendonta-Ferreira, F. de Bergevin, C. Mazzoli, L. Paolasini, Z. Fisk, and P. G. Pagliuso, Physica B: Condensed Matter **404,** 3014 (2009).

115. E. D. Bauer, et al., Physica B: Condensed Matter **378-380,** 142 (2006).

116. Z. Kurenbaeva, E. V. Murashova, Y. D. Seropegin, H. Nodl, and A. I. Tursina, Intermetallics **16,** 979 (2008).

117. N. Roberts-Warren, A. P. Dioguardi, A. C. Shockley, C. H. Lin, J. Crocker, P. Klavins, and N. J. Curro, Phys. Rev. B **81,** 180403 (2010).

118. V. H. Tran, D. Kaczorowski, R. T. Khan, and E. Bauer, Phys. Rev. B **83,** 064504 (2011).

119. K. Uhlířová: Single Crystal Studies of Novel Strongly Correlated Electron Compounds (doctoral thesis, Prague, 2010).

120. R. Vogel and H. Klose, Zeitschrift fur Metallkunde **45,** 633 (1954).

121. S. Kawasaki, et al., Phys. Rev. B **65,** 020504 (2001).

122. M. Mihalik, M. Diviš, and V. Sechovský, Journal of Magnetism and Magnetic Materials **322,** 1153 (2005).

123. W. Bardsley et al.: Crystal Growth: a Tutorial Approach 2 (North-Holland, New York, 1979).

124. B. Pamplin: Crystal Growth (University of Bath, Pergamon Press, 1975).

125. P. Canfield: The Design, Discovery, Growth and Physical Properties of Novel Intermetallic Compounds, Department of Physics, Ames Laboratory, Iowa State University, 2nd European School in Material Science, Ljubljana, Slovenia, 2007.

126. P. C. Canfield and I. R. Fisher, Journal of Crystal Growth **225,** 155 (2001).

127. P. C. Canfield and Z. Fisk, Philosophical Magazine B-Physics of Condensed Matter Statistical Mechanics Electronic Optical and Magnetic Properties **65,** 1117 (1992).

128. B. Ferre: Properties and Applications of Complex Intermetallics, Book Series on Complex Metallic Alloys - Vol. 2 (World Scientific Publishing, 2009) .

129. www.bruker-axs.de.

130. V. Valvoda, M. Polcarová, P. Lukáč: Základy strukturní analýzy (Karolinum, Praha 1992).

131. http: //www.ill.eu/sites/fullprof/.

132. http ://www.rigaku.com/smc/spider.html.

133. www.tescan.com.

134. M. Brown: Introduction to Thermal Analysis (Kluwer Academic Publishers, USA, 2001).

135. SETSYS Evolution 24, Commissioning maintence, SETARAM Instrumentation.

136. PPMS - Physical Property Measurement System User´s Manual (Quantum Design, San Diego, 2004).

137. MPMS - Magnetic Property Measurement System User´s Manual (Quantum Design, San Diego, 2004).

138. J. R. Waldram: Superconductivity of Metals and Cuprates (IOP Publishing Ltd., London, 1996).

139. R. B. Goldfarb, Cryogenics **26,** 621 (1986).

140. S. Takacs et al: Supravodivost (ALFA, Bratislava, 1979).

141. D. Shoenberg: Superconductivity (University Press, Cambridge, 1952).

142. Ch. Poole: Superconductivity (Elsevier, London, 2007).

143. G. Chanin and J. P. Torre, Phys. Rev. B **5,** 4357 (1972).

144. K. H. J. Buschow: Physics of Magnetism and Magnetic Materials (Kluwer Academic, New York, 2003).

145. J. Sereni: Magnetic Systems: Specific Heat in Encyclopedia of Materials: Science and Technology, edited by K. H. J. Buschow et al. (Elsevier, Oxford, 2001), p. 4986.

146. Z. Málek: Tepelné vlastnosti pevných látek v nízkých teplotách (Škola fyziky a techniky nízkých teplot, Tatranská Lomnica, 1974).

147. P. Svoboda: Komplexní přístup k analýze nízkoteplotního měrného tepla (MFF UK, Praha, 2006).

148. J. A. Blanco, M. de Podesta, J. I. Espeso, J. C. mez Sal, C. Lester, K. A. McEwen, N. Patrikios, and F. guez, Phys. Rev. B **49,** 15126 (1994).

149. P. Čermák, H. Kitazawa, J. Prchal, and P. Javorský, Journal of Physics-Condensed Matter **22,** (2010).

150. P. Čermák, K. Uhlířová, and P. Javorský, Physica B-Condensed Matter **405,** 2294 (2010).

151. R. M. Galera, A. P. Murani, and J. Pierre, Physica B: Condensed Matter **156-157,** 801 (2001).

152. J. Kamarád, Z. Machatová, and Z. Arnold, Rev. Sci. Instrum. **75,** 5022 (2004).

153. M. Míšek: Pressure influence on the magnetic and transport properties of the *f*-electron compounds (diploma thesis, Prague, 2008).

154. J. Pospíšil, M. Kratochvílová, M. Diviš, J. Prokleška, J. P. Vejpravová, and V. Sechovský, Journal of Alloys and Compounds **509,** 1401 (2011).

155. J. P. Perdew and Y. Wang, Phys. Rev. B **45,** 13244 (1992).

156. Z. Wu and R. E. Cohen, Phys. Rev. B **73,** 235116 (2006).

157. J. P. Perdew, K. Burke, and M. Ernzerhof, Phys. Rev. Lett. **77,** 3865 (1996).

158. T. Nagano, Y. Tomioka, Y. Nakayama, K. Kishio, and K. Kitazawa, Phys. Rev. B **48,** 9689 (1993).

159. W. L. McMillan, Phys. Rev. **167,** 331 (1968).

160. D. Fort, Journal of the Less Common Metals **134,** 45 (1987).

161. C. Adriano, et al., Phys. Rev. B **81,** 245115 (2010).

162. V. T. Rajan, Phys. Rev. Lett. **51,** 308 (1983).

163. T. Park, et al., Nature **456,** 366 (2008).

164. T. Park, Y. Tokiwa, E. D. Bauer, F. Ronning, R. Movshovich, J. L. Sarrao, and J. D. Thompson, Physica B: Condensed Matter **403,** 943 (2008).

165. T. Park, Y. Tokiwa, F. Ronning, H. Lee, E. D. Bauer, R. Movshovich, and J. D. Thompson, phys. stat. sol. (b) **247,** 553 (2010).

166. G. Knebel, D. Aoki, J. P. Brison, L. Howald, G. Lapertot, J. Panarin, S. Raymond, and J. Flouquet, phys. stat. sol. (b) **247,** 557 (2010).

167. A. Malinowski, M. F. Hundley, N. O. Moreno, P. G. Pagliuso, J. L. Sarrao, and J. D. Thompson, Phys. Rev. B **68,** 184419 (2003).

168. K. H. Bennemann: Superconductivity - Volume 1 (Springer, Berlin, 2008).

169. Y. Janssen, M. Angst, K. W. Dennis, R. W. McCallum, and P. C. Canfield, Journal of Crystal Growth **285,** 670 (2005).

170. S. Delfino, A. Saccone, and R. Ferro, Zeitschrift fur Metallkunde **71,** 165 (1980).

171. T. B. Massalski et al.: Binary Alloy Phase Diagrams (ASM International, 1990).

172. H. Flandorfer, Journal of Alloys and Compounds **336,** 176 (2002).

173. T. Studnitzky and R. Schmid-Fetzer, Journal of Electronic Materials **32,** 70 (2003).

# List of constants

$e$       Elementary charge ($1.602176487(40) \times 10^{-19}$ C)

$e'^2$       $e^2/2\pi$

$\Phi_0$       Magnetic flux quantum ($2.067\,833\,636 \times 10^{-15}$ Wb)

$h$       Planck constant ($6.62606896(33) \times 10^{-34}$ J s)

$\hbar$       Reduced Planck constant ($1.054571628\,(53) \times 10^{-34}$ J s)

$k_B$       Boltzmann constant ($1.380\,6504(24) \times 10^{-23}$ J K$^{-1}$)

$m_e$       Electron mass ($9.10938215(45) \times 10^{-31}$ kg)

$\mu_0$       Vacuum permeability ($4\pi \times 10^{-7}$ H m$^{-1}$)

$\mu_B$       Bohr Magneton ($5.050\,783\,24(13) \times 10^{-27}$ J·T$^{-1}$)

$N_A$       Avogadro constant ($6.02214179(30) \times 10^{23}$ mol$^{-1}$)

$R$       Ideal gas constant ($8.314472(15)$ J mol$^{-1}$ K$^{-1}$)

# List of Abbreviations

| | |
|---|---|
| APW | Augmented plane wave |
| AF | Antiferromagnetism, antiferromagnet, antiferromagnetic |
| BCS | Bardeen, Cooper, Schrieffer |
| BSE | Back scattered electrons |
| CF | Crystal field |
| DFT | Density functional theory |
| DOS | Density of states |
| DTA | Differential thermal analysis |
| EDX | Electron dispersive X-ray (detector, analysis) |
| FI | Ferrimagnetism, ferrimagnet, ferrimagnetic |
| FL | Fermi-liquid |
| FM | Ferromagnetism, ferromagnet, ferromagnetic |
| GGA | Generalized gradient approximation |
| HF | Heavy fermion |
| LDA | Local density approximation |
| lo | Local orbitals |
| LSDA | Local spin density approximation |
| MO | Magnetically ordered (states) |
| NFL | Non-Fermi-liquid |
| NM | Non-magnetic |
| QCP | Quantum critical point |
| RE | Rare earth |
| RKKY | Ruderman, Kittel, Kasuya, Yoshida |
| SC | Superconductivity, superconductor |
| SCES | Strongly correlated electron systems |
| SE | Secondary electrons |
| SEM | Scanning electron microscope (microscopy) |
| SDW | Spin density wave |
| $T_C$ | Curie temperature |
| $T_N$ | Néel temperature |
| $T_s$ | superconducting temperature |
| WHH | Werthamer, Helfand, Hohenberg |
| XRD | X-ray diffraction |

# Appendix A

# Thermal analysis of Ce-Pd-In system

The goal of the DTA measurements was to understand better the growth of various phases of the Ce-Pd-In starting stoichiometry within the flux growth and depending upon these results to improve the growth of $Ce_2PdIn_8$ phase at the expense of other phases. We have examined the DTA curves of binary or ternary compounds and starting mixtures of two or three elements, respectively. The results from development of the binary compounds were analyzed using corresponding phase diagrams. The ternary phase diagrams for Ce-Pd-In are not known except isothermal section at 773 K (see Fig. 57). Analysis of DTA results of these compounds was made using the DTA results obtained for the binary compounds and the results provided by solution growth of $Ce_2PdIn_8$.

It is necessary to mention, that the shape of the peak depends on the shape of the sample, on its contact with the walls of the crucible and many other effects, which can cause also different characters of the DTA curves in first and following cycles [169]. Considering fact, that the first cycles of DTA curves do not proceed in equilibrium state, we focused more on the investigation of the curves of following cycles, but some of the first heating curves can also provide interesting information related to corresponding phase diagrams. To confirm the reproducibility of our measurements, we prepared two samples with starting stoichiometry Pd:In - 1:25 and measured the heat flow under similar conditions. The curves of both samples resembled satisfactory each other (not shown).

## Ce-In binary system

In the case of Ce-In binary system, we investigated both possibilities – the elements Ce and In which were freely placed in the crucible and the single crystal of $CeIn_3$ compound in the In surplus. The mixture of Ce and In with starting stoichiometry 2:25 was heated and cooled twice between ~ 50 and ~ 1000 °C at 10 °C/min. The single crystal of $CeIn_3$ prepared commonly from In flux was accompanied with In surplus, so that the total ratio Ce:In was very close to 2:25. In Fig. 53, the heating and cooling curves of the sample Ce:In - 2:25 and $CeIn_3$ are shown. Endothermic and exothermic peaks at ~ 150 °C are representing the melting and solidification of In. The melting point cannot be determined because the exact temperature measurement starts above 20 °C for this high-temperature scan.
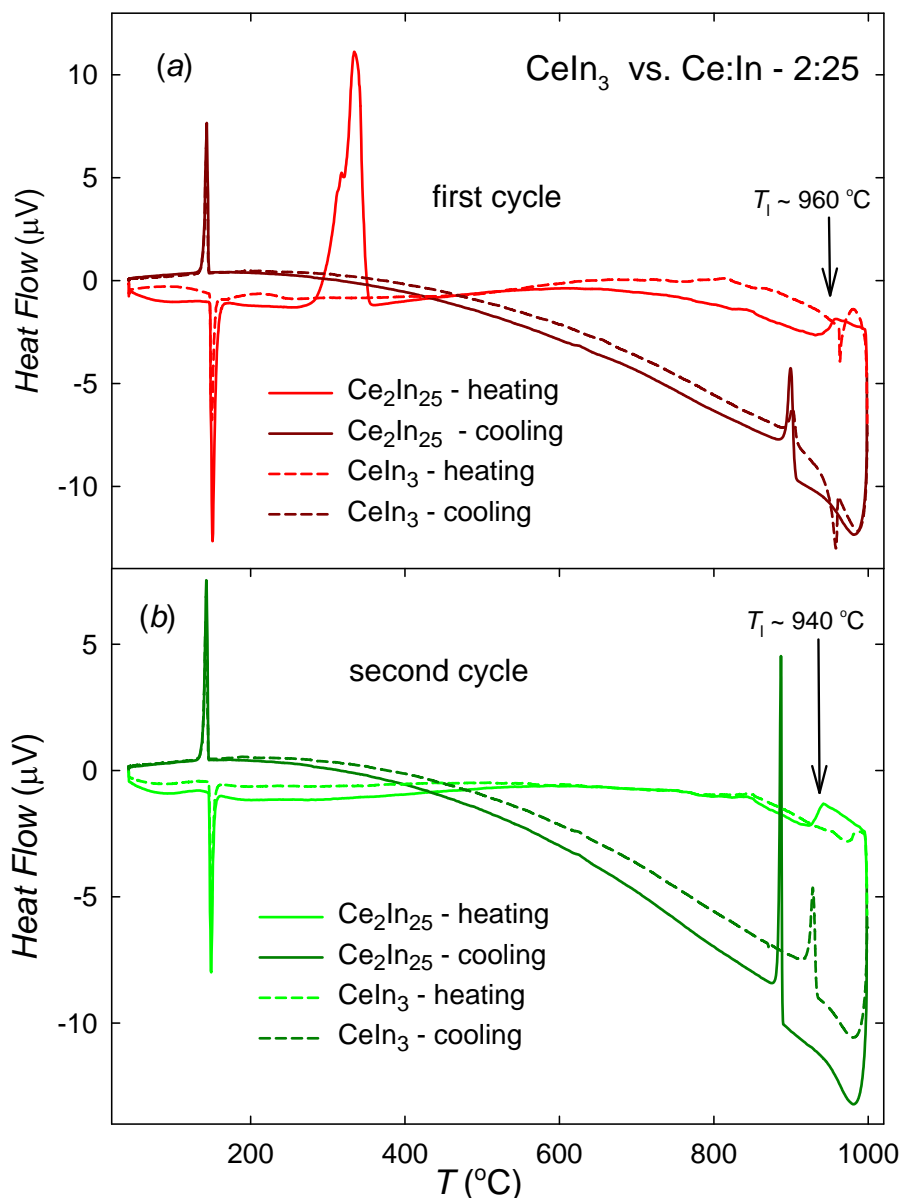
Fig. 53: The comparison of the DTA heating curves for Ce:In - 2:25 marked by solid lines and for the CeIn$_3$ compound in In surplus marked by the dashed line. The arrows mark the liquidus temperature $T_l$. The figure (a) represents the first cycle, the figure (b) represents the second cycle. The term "Ce:In - 2:25" is shortened in the legend to "Ce$_2$In$_{25}$".

In Fig. 54, the Ce-In binary phase diagram [120,170] is presented. The L/(L + CeIn$_3$) liquidus trend indicates that the L $\ll$ CeIn$_3$ + (In) eutectic composition is very close to 100 at.% In as shown in Fig. 54, suggesting very small solubility of Ce in In [170]. Accordingly, the eutectic temperature is only slightly lower than the melting point of In ($\sim 156$ °C). The sample Ce:In - 2:25 passes over the melting point of indium as the temperature increases, and the solid cerium starts to react with the liquid indium, which is indicated by the peak with onset temperature $\sim 260$ °C (see Fig. 53 (a)). The peak, marked by an arrow in Fig. 53 (a) and (b), corresponds to the liquidus temperature of CeIn$_3$ $T_l \sim 950$ °C and its position agrees with the observation in the phase diagram. The peak with onset temperature $\sim 260$ °C appears in all experiments only in the first run, independently on the starting stoichiometries of In and Pd (in case of ternary compounds). Assuming that not all the cerium has reacted during the first

run (green line in Fig. 54), we can observe a slight shift of the liquidus temperature to lower temperatures (pink line in Fig. 54), which agrees with the phase diagram.

In the case of CeIn$_3$, we do not observe any peak below 400 °C (see Fig. 53 (*a*)), which is expectable with the respect to the absence of non-reacted Ce in the sample. Similar peak as in Ce:In - 2:25 can be seen also at ~ 950 °C although the peak is much sharper in the first cycle.
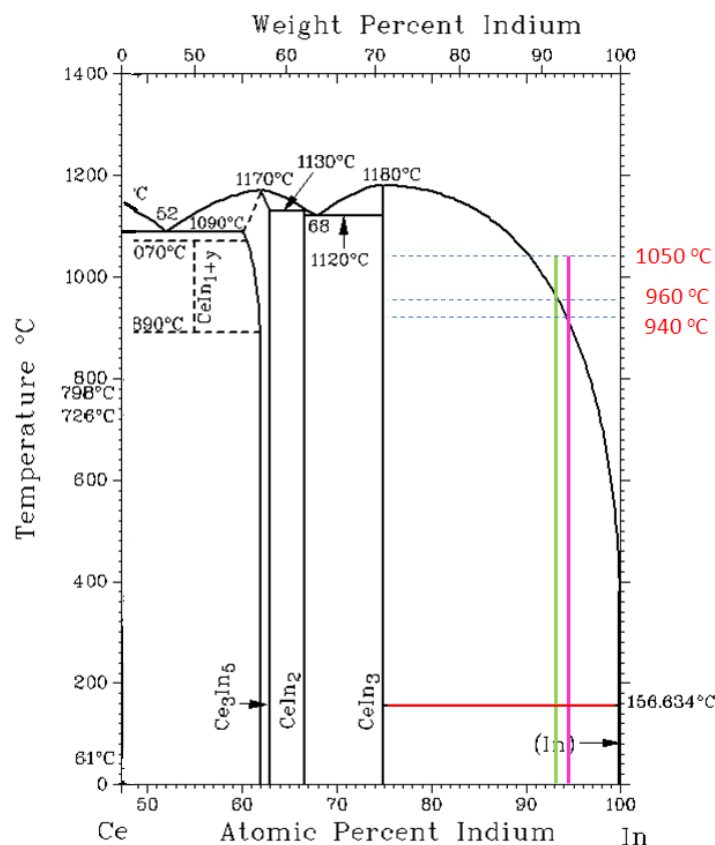


Fig. 54: The Ce-In binary phase diagram. The red line shows the melting point of In, the region between the red and blue line represents the conditions where Ce dissolutes in In; the green and pink line show the stoichiometry and liquidus temperature in the first and second run, respectively. After Vogel and Klose [120].

The cooling curve for stoichiometry 2:25 reveals a sharp exothermic peak with onset temperature ~ 900 °C, which corresponds to the temperature of liquidus transition and consecutive growth of CeIn$_3$ phase. We can observe a slight shifting of the crystallization peak in further cycle as well, which could be connected with the decreasing concentration of Ce, similar to the shifting of liquidus temperature. The shift of peak can be also caused by undercooling, which demands to keep the solution for few hours higher above the liquidus temperature, to ensure that all the nuclei will solute. This condition was not fulfilled in our measurement, which decreases the probability of this effect in our samples. The temperature dependence of heat flow for CeIn$_3$ compound during cooling reveals the peak corresponding to crystallization at similar temperature as in case of Ce:In - 2:25.

It was also reported [171], that CeIn$_3$ may show an order-disorder transformation above ~ 700 °C, but our measurements on binary compounds have not revealed any peak which could indicate this transition.

## Pd-In binary system

Similar experiment was performed with mixture of Pd and In elements freely placed in crucible with starting stoichiometry Pd:In - 1:25.
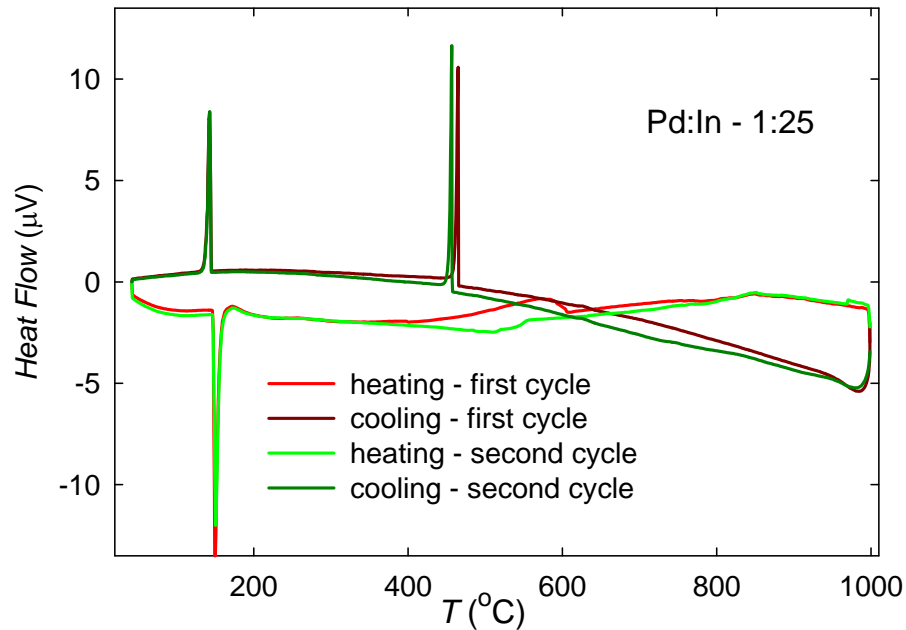


Fig. 55: The DTA curves of the binary system Pd-In with stoichiometry 1:25. The red lines represent the first cycle, the green lines represent the second cycle.

In Fig. 55, we observe the melting and solidification of indium again while heating and cooling, respectively. The eutectic reaction from liquid $L \rightarrow (In) + Pd_3In_7$ was reported [172] at 154 °C. However, because the Pd concentration of the eutectic point is negligibly small (see Fig. 56), the eutectic temperature must be very close to the melting point of In, i. e. ~ 156 °C. The eutectic reaction of Pd with In, which forms $Pd_3In_7$, is followed by the liquidus transition at ~ 630 °C according to Pd-In phase diagram [173]. The second cycle reveals that the dissolution was completed considering the missing bump. This time, we can see only the peak at ~ 550 °C pointing to the shifting of liquidus temperature, as it was mentioned in the case of Ce-In binary alloy. Cooling curve shows an exothermic transition - crystallization of $Pd_3In_7$ at onset temperature ~ 470 °C, corresponding to the In-rich stoichiometry. The shifting of the crystallization peak is probably caused by the same reasons as described by the Ce-In binary alloy.
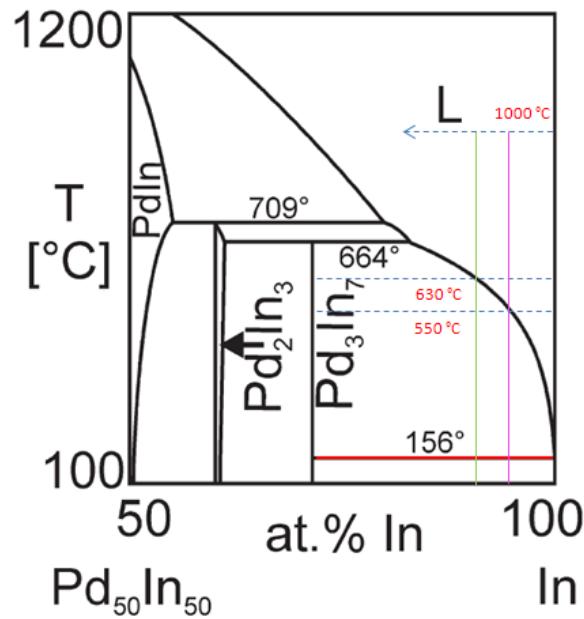
Fig. 56: The Pd-In binary phase diagram. The red line shows the melting point of In for chosen stoichiometry; the green and pink line show the stoichiometry and liquidus temperature in the first and second cycle, respectively. After Studnitzky *et al.* [173].

We also performed qualitatively different experiments with ternary compounds. The most direct way how to specify the thermal conditions suitable for the growth of $Ce_2PdIn_8$ compound, is to measure DTA curves of single crystals, but due to their small mass and thus small response of temperature dependence of the heat flow, we had no possibility to investigate the crystallization temperature directly and we have to rely on the interpretation from other data. The main task is to distinguish the peaks which correspond to binary compounds, from the other peaks, which should refer to crystallization of ternary compounds. We do not fully understand the differences between these heating and cooling curves, and especially the character of some peaks on the heating curve, but for crystal growth we only need to know the region between the liquidus temperature and the temperature where secondary phases may start to grow.

## Ce-Pd-In ternary systems

When looking at phase diagram presented in Fig. 57, we assume that it is possible to reduce all the possible compounds, which could crystallize during the cooling process, to $CeIn_3$, $Ce_2PdIn_8$, $Ce_4Pd_{10}In_{21}$ and $Pd_3In_7$, with respect to samples prepared from flux.
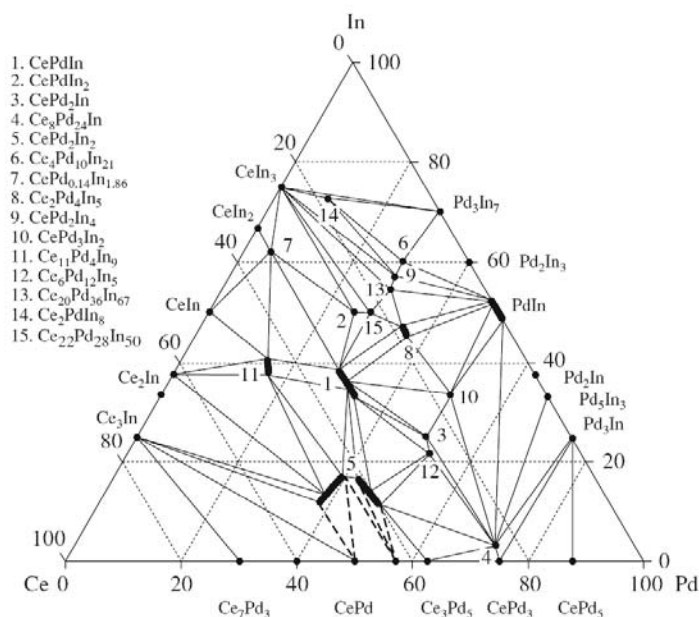
Fig. 57: Isothermal section of Ce-Pd-In phase diagram at 773 K. By Shtepa *et al.* [12].

As the first experiment, the polycrystal of starting composition 2:1:8 was prepared in monoarc, heated up to 1000 °C and cooled down several times and the composition of the final product was checked by EDX analysis and we have found that the polycrystalline material is inhomogeneous, containing grains of $Ce_2PdIn_8$, $CeIn_3$ and probably $Ce_4Pd_{10}In_{21}$ in non-stoichiometric composition. The cooling DTA curve, shown in Fig. 58, shows four peaks. We assume that these peaks can be ascribed gradually from the higher to lower temperatures to phases $CeIn_3$, $Ce_2PdIn_8$, $Ce_4Pd_{10}In_{21}$ and $Pd_3In_7$. Although $Pd_3In_7$ was not detected by EDX analysis, the other experiments show evidence for its presence in the sample in a very similar temperature region. The relative proximity of peaks corresponding to crystallization temperatures of phases $CeIn_3$ and $Ce_2PdIn_8$ indicates that the separation of these phases by lowering the maximum temperature of a thermal process could be complicated.
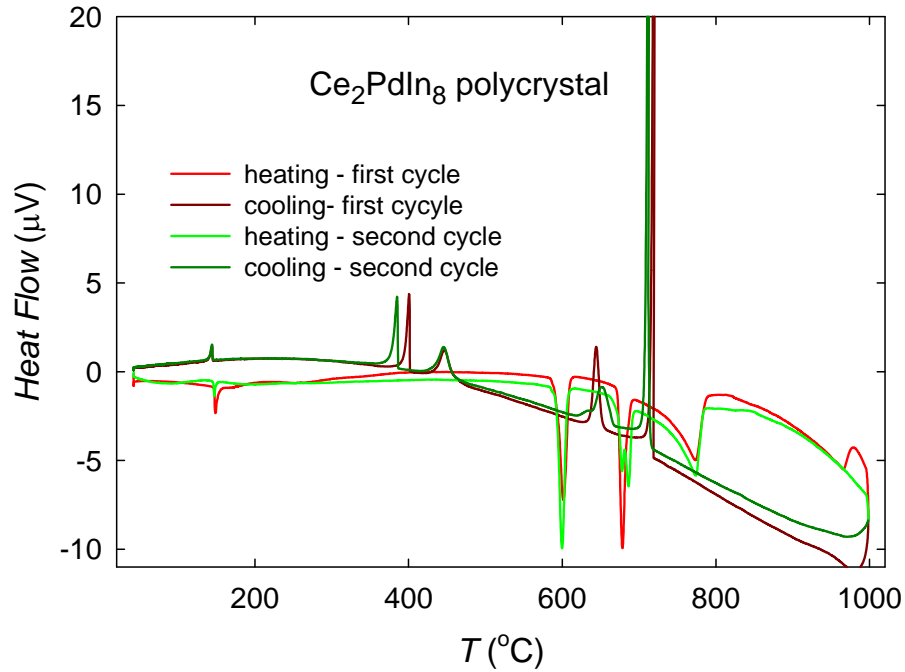
Fig. 58: The temperature dependence of heat flow for polycrystal of starting stoichiometry 2:1:8. The red lines represent the first cycle; the green lines represent the second cycle.

The other two samples were prepared in a form of a mixture from Ce, Pd and In elements with starting stoichiometry 2:1:25 and 2:1:8, respectively, freely placed in the crucible heated up to 1000 °C and cooled down several times. The ratio 2:1:25 was chosen along the stoichiometry used to synthetize single crystals of $Ce_2PdIn_8$ in solution growth method. The temperature dependence of the heat flow, shown in Fig. 59, indicates rather complex processes of crystallization of various phases during cooling.
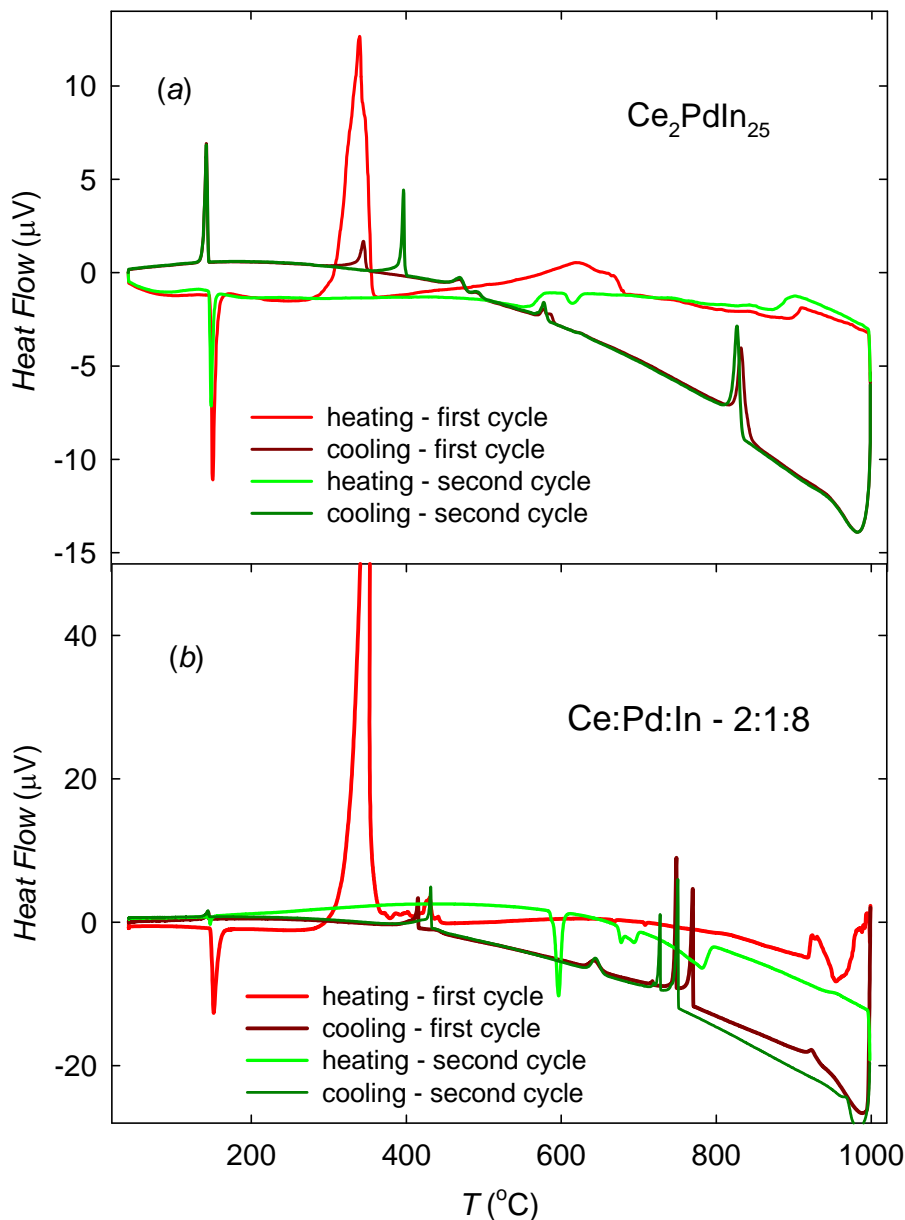
Fig. 59: The temperature dependence of heat flow for Ce-Pd-In mixtures of starting stoichiometries 2:1:25 (*a*) and 2:1:8 (*b*), respectively. The red lines represent the first cycle; the green lines represent the second cycle.

Heating curves of both stoichiometries show peaks corresponding to reaction of Ce with In (~ 340 °C) in the first cycle. In case of 2:1:25 stoichiometry in Fig. 59 (*a*), the heating curve exhibits reaction of Pd with In (~ 750 °C); the 2:1:8 stoichiometry in Fig. 59 (*b*) reveals an equivalent peak at ~ 430 °C, immediately after the reaction of Ce with In is completed. The heating curve for sample with 2:1:25 stoichiometry reveals a bump corresponding to liquidus temperature of $CeIn_3$ above 800 °C, analogically to the experiment in Fig. 53. The character of the heating curve in the other case is more complicated and probably indicates reactions of Ce and Pd with In.

Cooling curves in both experiments reveal four peaks in total, similar to DTA cooling curves of polycrystalline material. However, the onset temperatures of the peaks do not always agree with those in polycrystal. We assume, that the peaks observed in all performed

experiments in a relatively broad temperature range $350 < T < 430°C$, can be ascribed to the crystallization of $Pd_3In_7$ with respect to results in Fig. 55 and the solution growth of $Pd_3In_7$ (the compound was cooled down from 700 °C to 300 °C). When looking on the Ce-In phase diagram in Fig. 54, we can see that $CeIn_3$ has no chance to start to grow for the chosen ratio Ce:In 20:80, because the maximum temperature did not reach the necessary value of liquidus temperature $\sim 1200$ °C. On the other hand, $CeIn_3$ should reveal in the case of the sample with 2:1:25 stoichiometry. In Fig. 59 ($a$), a peak corresponding to crystallization of $CeIn_3$ at $\sim 830$ °C is observed. Its shift from temperature $\sim 900$ °C observed in Fig. 53 is caused probably because of presence of palladium. On the opposite, the DTA curves of sample with 2:1:8 stoichiometry in Fig. 59 ($b$) do not show this kind of peak, but a couple of peaks at significantly lower temperature ($\sim 750$ °C) appear. We suppose, that one of these peaks indicates solidification temperature of $Ce_2PdIn_8$, but the more probable explanation for the second one still lies in the crystallization of $CeIn_3$ compound with respect to the onset temperature. The explanation of the uncertain origin of this peak would be a subject of forthcoming studies.

| Temperature range of cooling (°C) | Obtained single crystals | |
| --- | --- | --- |
| | 2:1:25 | 2:1:40 |
| 950 - 600 | $Ce_2PdIn_8$, $CeIn_3$ | $CeIn_3$ |
| 825 – 600 | non-stoichiometric $CeIn_3$, $Ce_2PdIn_8$ | $CeIn_3$ |
| 750 - 500 | non-stoichiometric $Ce_2PdIn_8$ | non-stoichiometric $CeIn_3$ |

Tab. 10: The dependence of final products of crystal growth on the chosen thermal process.

To sum up the previous paragraphs, the results of binary compounds provided by DTA curves are in a very good agreement with binary phase diagrams. However, the results from ternary compounds cannot be interpreted for a certainty considering fact, that ternary phase diagrams are generally not known. Nevertheless, several important qualitative results were obtained. We can observe that the unwanted phase of $CeIn_3$ starts to grow at higher temperatures than $Ce_2PdIn_8$ and on the opposite, the unwanted phase of $Pd_3In_7$ starts growing at lower temperatures than $Ce_2PdIn_8$. Thus, a significant suppression of the growth of $CeIn_3$ and $Pd_3In_7$ can be realized by lowering the maximum temperature and by slight increasing the decanting temperature of thermal process. The maximum temperature, which can be used to avoid the growth of $CeIn_3$, decreases with the concentration of In. We have performed several experiments with synthesis of $Ce_2PdIn_8$ in reaction to results provided by DTA to confirm our conclusions. The $Ce_2PdIn_8$ compound was prepared from In flux and several randomly chosen samples were checked by EDX analysis and single-crystal X-ray diffractometer. Our results are summarized in Tab. 10 and they are in a good agreement with previous DTA experiments. Lower maximum temperature of the thermal process improves the quality of the $Ce_2PdIn_8$, and moreover, the amount of $Ce_2PdIn_8$ increases at the expense of $CeIn_3$. The quality of $Ce_2PdIn_8$ can be further improved probably by putting the temperature range more precisely and by lowering the cooling rates. These experiments are tasks of the forthcoming research.